



**Department of Physical, Chemical,
and Natural Systems**

University Pablo de Olavide

**TRANSPORT AND ACCESSIBILITY IN ZEOLITES
AND METAL-ORGANIC FRAMEWORKS**

Elena García Pérez

Seville, May 2010

TRANSPORT AND ACCESSIBILITY IN ZEOLITES AND METAL-ORGANIC FRAMEWORKS

DIRECTORA

Sofía Calero Díaz

Profesora Titular del Departamento de
Sistemas Físicos, Químicos y Naturales
de la Universidad Pablo de Olavide

Trabajo presentado para la obtención del título de Doctora con Mención Europea

Elena García Pérez

Licenciada en Ciencias Ambientales



Department of Physical, Chemical, and Natural
Systems

University Pablo de Olavide

Sofía Calero Díaz, profesora titular del Departamento de Sistemas Físicos, Químicos y Naturales de la Universidad Pablo de Olavide

CERTIFICA:

Que la presente memoria titulada “Transport and Accessibility in Zeolites and Metal-Organic Frameworks”, que presenta Elena García Pérez para la obtención del título de Doctora, ha sido realizada bajo mi dirección en este departamento, dentro del programa de Ciencia y Tecnología de Coloides e Interfases y que cumple los requisitos para poder optar a la Mención Europea.

Sevilla, Mayo de 2010

Sofía Calero Díaz

Directora

- Dra. S. Calero

Miembros del tribunal

- Presidente: Dr. J.B. Parra
- Secretario: Dr. P.J. Merkling
- Vocal 1: Dra. F. Siperstein
- Vocal 2: Dr. J. Gascón
- Vocal 3: Dra. E. Barea
- Suplentes: Dr. S. Lago y Dra. P. Zaderenko

Comité externo evaluador

- Dr. T.J.H. Vlugt
- Dr. D. Dubbeldam

The research reported in this thesis was carried out at the Department of Physical, Chemical, and Natural Systems, University Pablo de Olavide (Seville, Spain), with financial support from the European Research Area – Human Resources and Mobility – Marie Curie Fellowships, from the Spanish “Junta de Andalucía” – Proyecto de Excelencia, and from the Spanish “Ministerio de Educación y Ciencia” – a predoctoral fellowship and from the project CTA2007-63229/BQU.



Agradecimientos

Dicen que lo malo de finalizar una etapa es que a partir de este momento hay que buscar nuevos proyectos para alcanzar. Después de cinco años de duro trabajo, lo primero que me viene a la mente es cada una de las personas que me han ayudado a conseguir finalizar mi tesis. Por eso me gustaría agradecer a todas ellas su generoso apoyo.

En primer lugar me gustaría agradecer mi tesis a mi directora, **Sofía Calero**. Ella es un ejemplo de que la pasión por lo que las personas hacen no sólo permite disfrutar de tu trabajo sino que además facilita la excelencia. Ha sido una suerte poder contar con sus innumerables consejos y contribuciones a mi trabajo.

En segundo lugar quiero dar las gracias a **Berend Smít** y **Thijs Vlugt** por posibilitarme las estancias en el CECAM (Lyon) y en la Universidad de Delft. A **David Dubbeldam** por su constante ayuda y rápida respuesta a las dificultades que encontraba con el código. También quiero mostrar mi más sincero agradecimiento a las personas con las que he colaborado: **S. Lago, M.D. Lobato, T.L.M. Maesen, R. Krishna, J. van Baten, B. Liu, J.B. Parra, C.O. Anía, J. Gascón, V. Morales, F. Kapteijn, V. Fínsy, J. Denayer** y **P. Bárcia**. Todas ellas han hecho posible la publicación de las investigaciones llevadas a cabo.

Agradecer al grupo "RASPА": **Almudena García, Juanma Castillo, Juanjo Gutiérrez, Ana Martín, Rocío Bueno, Patrick Merklíng** y **Sáid Hamad** el día a día de estos últimos cinco años, porque trabajar codo a codo siempre es más gratificante. Gracias.

A mis compañer@s de la UPO, **Elena, Lucía, Paula, Ana, Paola, Manolo, Jose María, Manuel, Joaquín, Paco, Pedro, Tom, Pablo, Carlos, Thomas, Palma, Jesús** y **Javi** por hacer que el laboratorio no sólo sea un lugar de trabajo sino también de encuentros, por las cervezas de los jueves e infinidad de risas.

A **María, Tania** y **Sandra** por las horas de charlas, ánimos y buenos momentos. A **Pablo** porque me quiere y me hace feliz. A **mis padres** por su eterno apoyo al mundo de la investigación y por darme ánimos para continuar cuando me faltaban fuerzas. A mis hermanas **Marta** y **Clara** por escucharme, apoyarme y dejarme su ropa... y tantas cosas que ellas ya saben. A mi **familia** entera, que no saben que son las zeolitas, pero que de vez en cuando mostraban cierto interés en lo que esto significaba. También a

todos **amig@s** porque consiguieron que durante los fines de semana pudiera evadirme
y volver los lunes con fuerzas renovadas.

En definitiva, a tod@s los que han hecho posible que esté escribiendo estas palabras
como colofón a cinco años de trabajo porque sin ell@s no hubiera sido posible llegar
hasta aquí.

Contents

1 Introduction	1
1.1 Zeolites	2
1.2 Metal-Organic Frameworks (MOFs)	4
1.3 Molecular models and inter and intra molecular potentials	6
1.3.1 Modeling framework and non-frameworks ions	6
1.3.2 Modeling guest molecules	9
1.4 Simulation methods	14
1.5 Context and scope of this thesis	21
Bibliography	24
2 A Computational Study of CO₂, N₂, and CH₄ Adsorption in Zeolites	27
2.1 Introduction	27
2.2 Methodology	28
2.3 Results and discussion	31
2.4 Conclusions	38
Bibliography	39
3 Diffusion of CH₄ and CO₂ in MFI, CHA, and DDR Zeolites	41
3.1 Introduction	41
3.2 GCMC and MD simulation methodologies	42
3.3 Results and discussion	43
3.4 Conclusions	49
Bibliography	50

4 Molecular Simulation of Adsorption of *n*-alkanes in Na-MFI Zeolites.

Determination of Empirical Expressions	51
4.1 Introduction	51
4.2 Methods	52
4.3 Results and discussion	54
4.4 Conclusions	59
Bibliography	59

5 Elucidating Alkane Adsorption in Sodium Exchanged Zeolites from

Molecular Simulations to Empirical Equations	61
5.1 Introduction	61
5.2 Methodology	62
5.3 Results and discussion	64
5.4 Conclusions	69
Bibliography	70

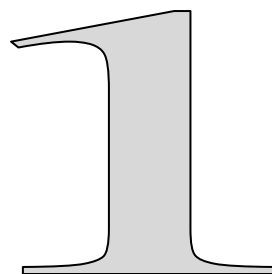
6 Influence of Cation Na/Ca Ratio on Adsorption in LTA 5A: A Systematic

Molecular Simulation Study of Alkane Chain Length	73
6.1 Introduction	73
6.2 Methods	76
6.2.1 Force field type	76
6.2.2 LTA-type zeolites	77
6.2.3 Force field model and parameters	78
6.2.4 Grand-Canonical Monte Carlo	80

6.2.5 Simulation details	80
6.3 Results	81
6.3.1 Calibration of zeolite–ion interactions	81
6.3.2 Calibration on isotherms	82
6.3.3 Predictions of isotherms	83
6.3.4 Predictions of Henry coefficients and heats of adsorption	86
6.3.5 Effect of cations	87
6.4 Conclusions	90
Bibliography	90
7 A Computational Method to Characterize Framework Aluminum in Aluminosilicates	93
Bibliography	99
8 Understanding Aluminum Location and Non-Framework Ions Effects on Alkane Adsorption in Aluminosilicates: A Molecular Simulation Study ...	101
8.1 Introduction	101
8.2 Simulation models and methods	102
8.2.1 Zeolite models	102
8.2.2 Force fields	103
8.2.3 Simulation technique	104
8.3 Results and discussion	104

Contents

8.3.1 Categorizing zeolites according to the sensitivity of adsorption properties to the aluminum distributions	104
8.3.2 Aluminum positions and alkane adsorptions in TON, FER, and MOR zeolites	105
8.4 Conclusions	113
Bibliography	114
9 Identification of Adsorption Sites in the Metal Organic Framework Cu-BTC Using Molecular Simulations	117
9.1 Introduction	117
9.2 Experimental	119
9.3 Simulation method and models	120
9.4 Results and discussion	123
9.5 Conclusions	132
Bibliography	133
10 Unraveling Argon Adsorption Processes in MFI-type Zeolite	135
Bibliography	141
11 Conclusions	143
Resumen y conclusiones (Summary and conclusions in Spanish)	145
List of publications	151



Porous materials are a subset of structured materials characterized by the presence of pores. They can render itself all sorts of useful properties that the corresponding bulk material would not have. Pores have various shapes and morphology such as cylindrical, spherical, and slit types. Porosity is not the only characteristic of these materials; they have a high surface area, very ordered, uniform structure, and fluid permeability. Furthermore, they are often non-toxic, inert, and chemically and thermally stable.

In the past few years, micro and nanomaterials have been an important target in science and technology due to their high capacity for adsorption and interaction with atoms, ions, and molecules on their internal surfaces and in the pore space. They also have high selectivity that depends on the size, shape, and distribution of the pores as well as on the nature of the adsorbate components.

A “molecular sieve” is a material with these properties. Examples of molecular sieves include zeolites (microporous materials) and Metal-Organic Frameworks, MOFs (nanoporous materials). They are regular frameworks that have void spaces (cavities or channels) that can host cations, water, and many other molecules.

Due to their structural and compositional features, zeolites and MOFs can be used for a variety of processes. Some of the main applications and market potentials are drying of refrigerants, water softening devices (detergents and soaps), removal of atmospheric pollutants, industrial air purification, separation and recovery of normal paraffin hydrocarbons, recovery of radioactive ions from polluted water, catalysis of hydrocarbon reactions, and the curing of plastic.

Synthetic porous materials have an additional property. It is possible to tailor design their structures for specific applications as an example the shape and size of the zeolite pores, as well as the type and number of cations in the structure take a relevant role in industry, especially in petrochemical industry. Here, zeolites are used as catalysts for Fluid Catalytic Cracking (FCC) process, which transforms long-chain alkanes (heavy oil) into shorter ones (petrol) and enhances the octane number of petrol by producing branched species.

Among the most important applications of porous materials, gas adsorption and separation is one of the most studied. The ability of zeolites and MOFs to selectively adsorb many gases is in part determined by the size of the channels. They adsorb preferentially molecules such as ammonia, sulphur dioxide, carbon monoxide, carbon dioxide, water, oxygen, nitrogen, Volatile Organic Compounds (VOCs), and others, according to length, size, and configurational entropy[1].

From the environmental point of view, it is necessary to develop effective separation technologies to reduce the carbon dioxide emissions that are noticeably increasing due to the use of fossil fuels. From the economic point of view, the removal of carbon dioxide from natural gas[2] and the recovery of methane from landfill gases are examples of interesting separations. Therefore, new adsorbent materials with well defined pore sizes and high surface areas are being developed and tested for potential use in energy storage and environmental separation technologies.

1.1 Zeolites

The name “zeolite” (comes from the Greek words *Zeo* – to boil and *Lithos* – stone) was originally coined in the 18th century by the Swedish scientist Axel Fredrik Cronstedt to refer to a curious mineral that was discovered. Literally it means “stones that boil”, due to zeolites expulse water when heated and after that, they can rehydrate again when cold.

Nowadays, there are around 48 natural zeolites, they occur naturally as minerals and are extensively mined in many parts of the world. They form in a number of relatively low temperature geologic environments. Gas pockets in basalt and other volcanic rocks may contain a high number of crystal groups of zeolites. Currently, there are approximately 170 different zeolite framework types that have been synthesized[3]. They are made commercially for specific uses or produced by scientists trying to understand more about their chemistry.

The most relevant characteristics of zeolites are:

- high adsorption capacity due to their intracrystalline surface area and strong interactions with adsorbates,
- high hydration capacity,
- elevated thermal stability, and
- high ion exchange capacity that depends on:
 - the nature of the ions species, the ion size, and ion charge;
 - the temperature,
 - the concentration of the ionic species in the solution,

- the anion associated with the ion in solution,
- the solvent (aqueous or organic solutions),
- the structural characteristics of the particular zeolite: topology and framework charge density.

Zeolites are uniform three-dimensional microporous crystalline materials with pores of about the same size of small molecules like water or hexane, typically between 3 and 10 Å in diameter. The structure of a zeolite consists of covalently bonded TO_4 units, in which the T-atoms are usually silicon (Si) or aluminum (Al) atoms. A representation of this structure is shown in Figure 1.1. The vast three-dimensional networks are a result of all four corners for the tetrahedral being shared, producing low density microporous materials.

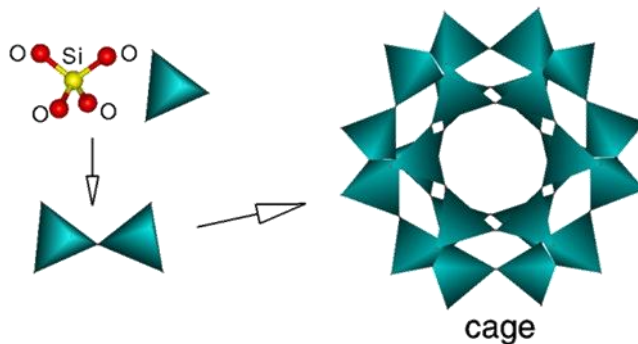


Figure 1.1 The silicon and aluminum atoms are tetrahedrally coordinated with each other through shared oxygen atoms.

The Primary Building Units (PBU's) are the TO_4 tetrahedral and they form Secondary Building Units (SBU's) that contain up to 16 T atoms. The SBU's join to form structurally and chemically important zeolite channels known as oxygen windows that pass through the zeolite and form a pore system. This microporous system can be different from a structural point of view, attending to the pore spatial distribution: cages, parallel, or interconnecting channels. The size and shape of these channels is decisive in separation processes.

The pores passing through the zeolite in one, two, or three directions vary in size. A unit cell always contains the same number of SBU's, and although rare, some materials can have different combinations of SBU's within the zeolite framework.

In the framework, aluminum and silicon are bound to each other through shared oxygen atoms. AlO_4 results in a negative net charge that is balanced by cations present during synthesis, such as Na^+ , K^+ , Ca^{2+} , Mg^{2+} , or H^+ . These ions are highly mobile and can be exchanged for other ionic species. According to the so-called Löwenstein rule, Al–O–Al linkages are energetically forbidden. As a result, all aluminate tetrahedral must be linked to four silicate tetrahedral, but a silicate tetrahedron may have different possible environments: Si (0 Al, 4 Si), Si (1 Al, 3 Si), Si (2 Al, 2 Si), Si (3 Al, 1 Si), and Si (4 Al, 0 Si).

The amount of aluminum present in zeolites is expressed by means of the Si/Al ratio, calculated from the total number of silicon and aluminum atoms per unit cell. The amount and location of the aluminum atoms have an influence on the catalytic, adsorption, and diffusion properties of zeolites.

1.2 Metal-Organic Frameworks (MOFs)

Metal-organic frameworks are a new family of hybrid porous materials that result from the reaction between organic and inorganic species. They consist of small metal-containing clusters connected three dimensionally by organic ligands[4-9]. Conceptually, there is no difference between zeolites and MOFs. Indeed, the three-dimensional skeleton can be described as in zeolites by the association of secondary building units (SBU's). However, whereas the zeolite SBU's contains only inorganic parts, in the metal-organic SBU's, the anionic species are replaced by organic linkers. The ligands act as spacers, creating an open porous structure with very high pore volume and surface area. Due to their unusual variety in terms of chemical composition, accessibility, and pore dimensions as well as to their low densities ($0.2\text{-}1\text{ g/cm}^3$) and high surface areas ($500\text{-}4500\text{ m}^2/\text{g}$) MOFs are considered promising candidates for gas storage and separation applications[6,10].

The first report on gas adsorption using MOFs was published in 1997[11], and since then MOFs have become an active field of research, resulting in numerous publications[12-15].

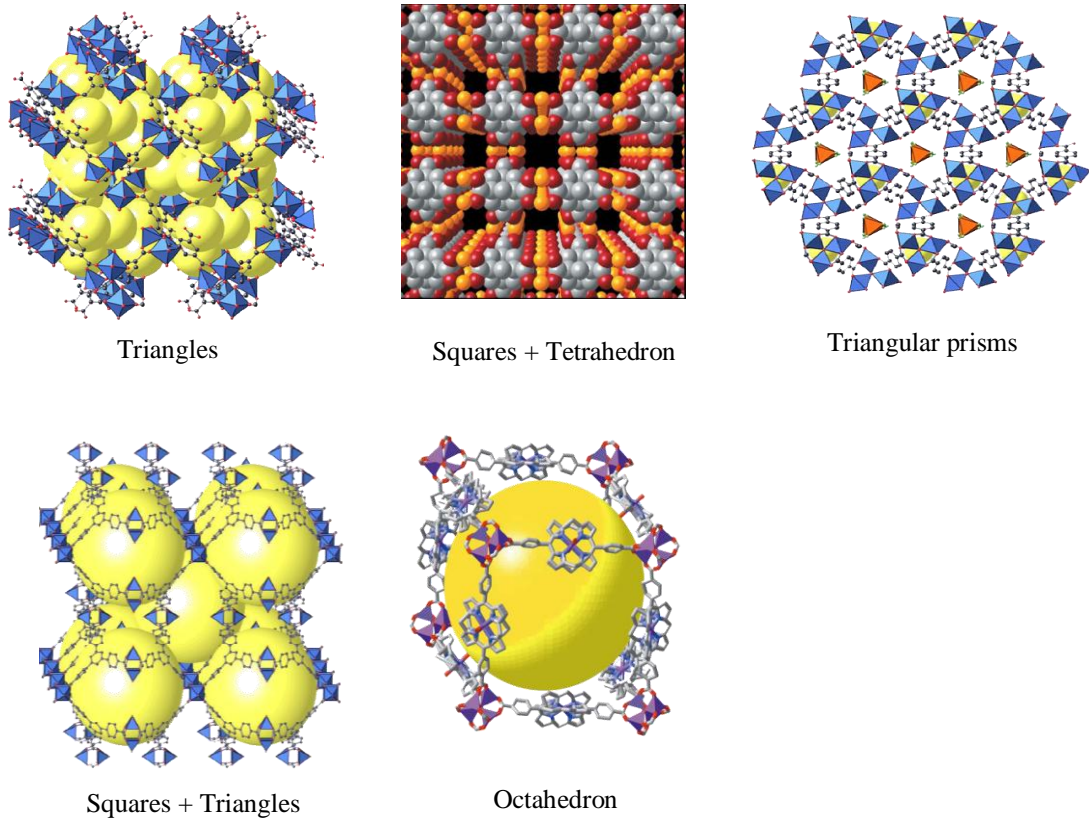


Figure 1.2 MOFs classification from the atomic association around the metal ion clusters[9].

Thousands of different MOFs have been synthesized to date with a very large range of compositions and structures[16-18]. MOFs can be classified in different groups, depending on 1) the type of the central atom, 2) how the atoms can be linked to the metal ion clusters (Figure 1.2), and 3) the nature of the organic ligands.

Whereas the potential of MOFs as catalysis, molecular sensors, luminescent, magnetic materials, and drug delivery materials has already been proven, the most promising applications probably lie in the field of adsorptive storage and separation, being hydrogen adsorption one of the most studied topics[19].

1.3 Molecular models and inter and intra molecular potentials

In this section we provide a general idea of the molecular models and simulation techniques applicable to periodic framework studies. Firstly, we describe the molecular models and interaction potentials for the adsorbents, the non-framework ions, and the guest molecules. Secondly, we summarize the simulation methods used to compute the different properties studied in this work.

This section deals with a description of the most common models and inter and intra molecular potentials for all the atoms and molecules involved in the studied systems: frameworks, non-framework ions, and guest molecules.

1.3.1 Modeling framework and non-frameworks ions. We study two types of porous materials: zeolites and metal-organic frameworks. The zeolite framework is usually built from silicon, aluminum, and oxygen with the crystallographic positions of these atoms taken from the dehydrated structures[20]. Substitution of silicon for aluminum in a zeolite generates a negative net charge in the framework that needs to be compensated by either non-framework cations or protons in order to make the zeolite charge neutral. Static atomic charges are obtained from the work of Jaramillo and Auerbach[21]. In our models, different charges are used for oxygen atoms bridging two silicon atoms, q_{OSi} , and oxygen atoms bridging one silicon and one aluminum atom q_{OAl} . The charge distribution on the oxygen framework was considered static; i.e. polarization of oxygen by nearby extra framework ions is neglected. q_{OSi} is obtained using the relation $q_{Si} + (2 \times q_{OSi}) = 0$, making the zeolite charge neutral in the absence of aluminum, while q_{OAl} is chosen to make the total system charge equal to zero[22-24]. We allow, cations and protons to move freely and adjust their position depending on their interactions with the framework atoms, other ions, and guest molecules[22]. The ion motions are sampled using displacements at random positions that bypass energy barriers.

As mentioned in previous section metal-organic frameworks consist of small metal-containing clusters connected by organic ligands. The atomic positions of the MOFs, as for the zeolites, are initially taken from their crystallographic positions[25]. We define a force field as the set of functions and parameters needed to describe the interactions between the atoms in a specific molecular system. There are many representative groups of universal force fields like the Universal Force Field (UFF)[26] or DREIDING[27]. The generic force fields include organic compounds, metals, and transition metals. They are normally expected to provide realistic predictions of molecular structures. When high specialized systems as adsorption and diffusion in porous systems are studied, these generic force fields give very poor results.

With regard to molecular simulations of MOFs, force fields have been developed and tested less profoundly as compared to zeolites. First of all, the more complex chemical nature of MOFs and the wide diversity in structure and composition complicates the modeling of the structure and the development of suitable force fields and increases the computational time. Secondly, few experimental data are available making validation of the simulation methods problematic. Thirdly, several MOFs structures exhibit significant framework flexibility, making accurate simulations even harder.

In most published works, the lattices are assumed rigid during simulations using the Kiselev-type potentials[28], where the framework atoms are held fixed at the crystallographic positions. Therefore, the structures are described in terms of their unit cell and their space group.

The use of a flexible model is highly expensive but this flexibility of frameworks may be important in some processes. Several authors have investigated the effect of flexibility using a variety of potentials for the framework atoms[29-35]. In this thesis, to understand physisorption phenomena of argon in MFI-type zeolite, two host flexible force fields were used: the Demontis model[34] and the force field developed by Nicholas et al.[35]

The Demontis model considers only interactions between nearest neighbors and, therefore, is computationally very efficient. Two simple harmonic potentials are defined to compute the whole sum of potential energy terms of the host system:

- Si-O bond stretching

$$V(r) = \frac{k_r}{2} (r_{Si-O} - r_{Si-O}^{eq})^2 \quad [1.1]$$

- Si-O/O-Si-O bond angle coupling (Urey-Bradley terms)

$$V(r) = \frac{k_{Urey-Bradley}}{2} (r_{O-O} - r_{O-O}^{eq})^2. \quad [1.2]$$

Here, k_r and $k_{Urey-Bradley}$ are the potential constants, r_{Si-O} and r_{O-O} are the actual distances, and r_{Si-O}^{eq} and r_{O-O}^{eq} are the equilibrium distances, respectively. O-O represents two adjacent oxygen atoms that are bonded to the same silicon atom[34].

Nicholas et al. developed a flexible model for silica sodalite, called General Valance Force Field (GVFF)[35]. The Nicholas model for zeolites is much more accurate than the Demontis model but also more expensive to compute. This model includes bond stretching, bond bending, bond angle coupling, a dihedral potential, Lennard-Jones interactions, and electrostatic interactions.

- Bond stretching. The Si–O bond stretch is modeled using a simple harmonic potential

$$V(r) = \frac{k_r}{2} (r - r_{eq})^2 \quad [1.3]$$

where k_r is the harmonic force constant, r is the Si–O bond length, and r_{eq} is the equilibrium Si–O bond length.

- Bond bending. To reproduce the O–Si–O bond angle bend is also modeled with a harmonic potential

$$V(\theta) = \frac{k_\theta}{2} (\theta - \theta_{eq})^2. \quad [1.4]$$

The Si–O–Si bond bending is modeled using a quartic potential because is highly harmonic and is necessary to avoid angles bigger than 180°.

$$V(\theta) = \frac{k_{\theta 1}}{2} (\theta - \theta_{eq})^2 + \frac{k_{\theta 2}}{2} (\theta - \theta_{eq})^3 + \frac{k_{\theta 3}}{2} (\theta - \theta_{eq})^4 \quad [1.5]$$

k_θ , $k_{\theta 1}$, $k_{\theta 2}$, and $k_{\theta 3}$ are the angle bending force constants, θ is the actual bond angle, and θ_{eq} is the reference bond angle.

- Si–O bond/Si–O–Si bond angle coupling. These interactions are defined using a Urey-Bradley potential, based on the Si–Si non-bonded distance for each Si–O–Si angle

$$V(r) = \frac{k_r}{2} (r_{T-T} - r_{eq})^2 \quad [1.6]$$

where r_{T-T} is the distance between Si–Si atoms in Si–O–Si bend.

- Dihedral angle. The torsional potential for the Si–O–Si–O dihedral angle is a periodic function with a 3-fold barrier

$$V(\Phi) = \frac{k_{\Phi}}{2} (1.0 + \cos(3\Phi)) \quad [1.7]$$

where k_{Φ} is the force parameter and Φ is the actual dihedral angle.

- Lennard-Jones (LJ) interactions. Non-bonded interactions were represented by LJ potentials, where r is the interatomic distance, and A and B are the values for LJ parameters for zeolite atoms interactions

$$V_{(r)} = \frac{B}{r^{12}} - \frac{A}{r^6}. \quad [1.8]$$

- Electrostatic interactions. Non-bonded electrostatic interactions were modeled by a Coulombic potential

$$V_{(r)} = \frac{1}{4\pi\epsilon_0} \frac{q_i q_j}{\epsilon_r r_{ij}} \quad [1.9]$$

where q_i and q_j are the charges of the zeolite atoms taken from Calero et al.[22], ϵ_0 is the permittivity of free space, ϵ_r is the dielectric constant, and r_{ij} is the interatomic distance.

1.3.2 Modeling guest molecules. We use classical models of atoms and molecules. In these models one atom or set of atoms (*pseudo-atoms*) are represented by a single interaction center with their own effective potentials[36].

For modeling guest molecules we can use rigid or flexible models. Small molecules such as carbon dioxide, nitrogen, and oxygen can be modeled using a rigid model with multipoles or polarization[37-39]. Complex molecules such as hydrocarbons normally require flexible models. The alkanes are described with a *united atom model*, in which each CH_x group is considered a *pseudo-atom*. A variety of flexible models have been addressed in literature[27,40-47].

Most commonly used force field consists at least of bonded and non-bonded terms:

$$U^{total} = U^{bonded} + U^{non-bonded} \quad [1.10]$$

with

$$U^{bonded} = U^{bond} + U^{bond-bending} + U^{torsion} + U^{intraVDW} \quad [1.11]$$

$$U^{non-bonded} = U^{VDW} + U^{Coulomb} . \quad [1.12]$$

When a zeolite or MOF framework is involved we have

$$U^{total} = U_g^{bonded} + U_h^{bonded} + U_{gg}^{non-bonded} + U_{gh}^{non-bonded} + U_{hh}^{non-bonded} \quad [1.13]$$

where g denotes *guest* and h denotes *host*. The thermodynamic properties of adsorbed molecules are overwhelmed by the strong adsorbent–adsorbate (host–guest) interactions. Below we list the functional forms of the bonded and non-bonded terms in the force fields used in this thesis. In Figure 1.3 the *united atom* representation of n -octane is shown with its bonded terms.

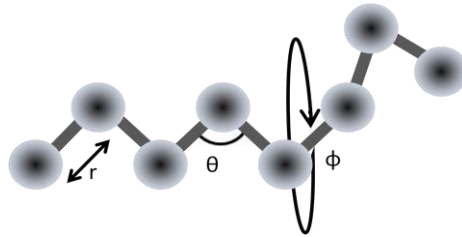


Figure 1.3 *United atom* representation of n -octane. The bond length r , the bend angle θ , and the torsion angle Φ are shown.

Bonded potentials

- Bonding potential U^{bond} . The bond potential describes the potential energy between two neighboring atoms in a molecule. They are functions of the interatomic distances only, where the distance is defined as $\mathbf{r}_{ij} = \mathbf{r}_j - \mathbf{r}_i$. There are many functional forms for the bonded terms like the harmonic bond potential, the Morse bond potential, the m - n bond potential, the quartic potential, etc. Among them, the bond potential used in this work is the harmonic bond potential, defined as

$$U_{harm}(r_{ij}) = \frac{1}{2}k(r_{ij} - r_{eq})^2 \quad [1.14]$$

where k is the stiffness of the bond, r_{ij} is the distance between two neighboring atoms, and r_{eq} is the equilibrium bond length. In our simulations of flexible molecules (from C₂ to C₁₆) r_{eq} is 1.54 Å. Molecules as CO₂, O₂, and N₂ are simulated as rigid and modeled with fixed bond lengths.

- Bond-bending potential U^{bend} . The bond-bending potential is the potential energy associated with the angle θ_{jik} between two successive bonds of three neighboring atoms in a molecule. There are many functional forms for the bond-bending potentials, e.g. the harmonic potential, the quartic potential, and the harmonic cosine potential. Among them, the bond-bending potentials used in this work are the harmonic potential and the harmonic cosine bending potential.

The harmonic potential is defined as

$$U_{harm}(\theta_{jik}) = \frac{1}{2}k(\theta_{jik} - \theta_{eq})^2 \quad [1.15]$$

The harmonic cosine potential is defined as

$$U_{harm-cos}(\theta_{jik}) = \frac{1}{2}k(\cos(\theta_{jik}) - \cos(\theta_{eq}))^2 \quad [1.16]$$

where θ_{eq} is the reference angle and k is the bond-bending constant. Both parameters can be obtained from quantum mechanical calculations or from infrared spectroscopy[48]. The energy needed to distort an angle away from equilibrium is much lower than that needed to distort a bond. Consequently bond angle bending force constants tend to be proportionally smaller than those for bond stretching. For normal alkanes, the average angle θ_{eq} is 114°. For rigid molecules the bond-bending angle is fixed.

- Torsion potential $U^{torsion}$. The torsion potential is related to the dihedral angle ϕ of four successive atoms in a molecule. There are many functional

forms for the torsion potentials like the cosine potential, the harmonic potential, the harmonic cosine potential, the triple cosine potential, the TraPPE dihedral, the Ryckaert-Bellemans potential, etc. Among them, the torsion potentials used in this work are the TraPPE dihedral and the Ryckaert-Bellemans (RB) potentials.

The TraPPE dihedral potential (Transferable Potentials for Phase Equilibria force field) is define as

$$U^{torsion} = p_0 + p_1 [1 + \cos(\phi_{ijkl})] + p_2 [1 - \cos(2\phi_{ijkl})] + p_3 [1 + \cos(3\phi_{ijkl})] \quad [1.17]$$

where p_0/k_B , p_1/k_B , p_2/k_B , and p_3/k_B are the four arguments in units of K.

The Ryckaert-Bellemans potential is often used for alkanes. The use of this potential implies exclusion of LJ interactions between the first and last atoms of the dihedral, and $\theta = \phi - \pi$ is defined according to the polymer convention $\theta_{trans} = 0$.

$$U_{ijkn} = \sum_n C_n \cos^n(\theta) \quad [1.18]$$

The Ryckaert-Bellemans potential can also be used to include the Optimized Potentials for Liquid Simulations (OPLS) dihedral potential.

Because of the equalities $\cos(2\phi) = 2\cos^2(\phi) - 1$ and $\cos(3\phi) = 4(\cos^3(\phi) - 3\cos(\phi))$ one can translate the OPLS parameters to RB parameters as follows

$$\begin{aligned} C_0 &= A_0 + A_2 + \frac{1}{2}(A_1 + A_3) \\ C_1 &= \frac{1}{2}(3A_3 + A_1) \\ C_2 &= -A_2 \\ C_3 &= -2A_3 \\ C_4 &= 0 \\ C_5 &= 0 \end{aligned} \quad [1.19]$$

with OPLS parameters in protein convention and RB in polymer convention.

Non-bonded potentials

Non-bonded interactions act between atoms in the same molecule and those in other molecules. Force fields divide these interactions into two: Van der Waals interactions and electrostatic interactions.

- Van der Waals potential U^{VDW} . In this work we use the Lennard-Jones (LJ) potential, which describes short-range interactions. The LJ potential is a pair potential depending on the distance between two atoms of different molecules, as well as between two atoms in the same molecule. The interactions of the adsorbed molecules with the zeolite are dominated by the dispersive forces between the pseudo-atoms and the oxygen atoms of the zeolite[28,49,50]. LJ potential is defined as

$$U^{LJ} = 4\varepsilon \left[\left(\frac{\sigma}{r_{ij}} \right)^{12} - \left(\frac{\sigma}{r_{ij}} \right)^6 \right] \quad [1.20]$$

where σ and ε are the intermolecular parameters often fitted from experimental data such as the critical temperature and density[51]. For interactions with zeolites, LJ parameters are fitted to experimental adsorption data[52]. The parameters of σ_{ij} and ε_{ij} between different atoms i and j can be estimated from the LJ parameters of σ_{ii} and ε_{jj} of identical atoms. The mixing rules used in this work are the Lorentz-Berthelot mixing rules:

$$\sigma_{ij} = \frac{\sigma_{ii} + \sigma_{jj}}{2} \quad [1.21]$$

$$\varepsilon_{ij} = \sqrt{\varepsilon_{ii} \cdot \varepsilon_{jj}} \quad [1.22]$$

The LJ potentials have an infinite range, so we must analyze $n \times (n - 1)$ pair-potentials each time step. This is computationally unaffordable for large systems, being necessary to establish a cutoff radius. The typical cutoff distance of LJ potential is usually chosen as 12 Å. Interactions longer than this distance are omitted from the energy and force computations. The potential can either be shifted to zero at the cutoff, or can be just neglected after the cutoff, or the remainder of the potential energy can be approximated

using tail corrections. This is specified in the force fields and can be applied for each interaction individually. The length of the simulation box needs to be at least twice as large as the cutoff distance.

- Electrostatic interactions $U^{Coulomb}$. They are important interactions in many molecular simulations. The interactions between point charges are generally modeled by Coulomb potentials

$$U^{Coulomb} = \frac{1}{4\pi\epsilon_0 \epsilon_r} \frac{q_i q_j}{r_{ij}} \quad [1.23]$$

where ϵ_0 is the permittivity of free space, ϵ_r the relative dielectric constant of the medium which the charges are placed, q are the magnitude of the atomic charges of atoms, and r_{ij} is the distance between atoms i and j . The electrostatic potential energy will be negative if the charges have opposite sign and positive if the charges have the same sign. Negative mutual potential energy corresponds to attraction between two charges; positive mutual potential energy involves repulsion between two charges. This potential can be neglected for non-polar guest molecules. The Coulombic interactions in the system are calculated by Ewald summation for periodic systems[53].

Accurate parameters provide quantitative good predictions for adsorption and transport properties in these systems. Despite the increasing amount of publications dealing with the synthesis of new MOFs, much less effort has been devoted to a better understanding of the interactions between the MOF and the guest molecules. The chemical diversity of these materials has made general force fields attractive. However, specific force fields have been developed for zeolites. In this work we use a method, developed by Dubbeldam et al., to obtain accurate sets of parameters for zeolites, based on fitting to experimental isotherms with inflection points[54].

1.4 Simulation methods

This section focuses on force field-based methods to compute adsorption and diffusion properties in porous materials. Modeling adsorption and diffusion in porous materials is generally based on classical mechanics. *Periodic boundary conditions* allow to predict properties valid for an extended crystal lattice. They are a set of boundary conditions that are often used to simulate a large system; they are applied to avoid the problems of surface effects. The original simulation box, including all the atoms within it, is replicated throughout the space. When a molecule passes through one side of the unit cell, it

reappears on the opposite side at the same conditions. The *minimum-image convention* is a useful form of periodic boundary conditions, which means that an individual atom in the simulation only interacts with the closest image of the remaining particles in the system[53]. The number of unit cells in the simulation box has chosen such the minimum length in each of the coordinate directions was larger than two times the cutoff distance.

Monte Carlo methods involve performing many simulations using random numbers and probability to get an approximation of the answer to the problems. The Monte Carlo simulation technique had formally existed since the early 1940s, but only with the increase of the computational power and technology has become more widely used.

The Markov Chain Monte Carlo method (MCMC) is an important tool that provides average properties of systems with a very large number of accessible states. This method is based on sequences of random numbers to perform the simulations. A random walk is constructed in such a way that the probability of visiting a particular system state is proportional to the Boltzmann factor $\exp[-\beta U_i]$.

The Monte Carlo scheme makes use of the fact that only the relative probability of visiting points in configuration space is needed, not the absolute probability. To visit points with the correct frequency, the MCMC algorithm generate random trial moves from the current state (o) to a new state (n), for example, giving one of the particles a random displacement. This new state (n) is either accepted or rejected in such way that states are visited with a probability proportional to $P_B(o)$. It is often convenient to apply the condition of detailed balance. If $P_B(o)$ and $P_B(n)$ denotes the probability of finding the system in state (o) and (n), respectively, and $\alpha(o \rightarrow n)$ and $\alpha(n \rightarrow o)$ denote the conditional probability to perform a trial move from $o \rightarrow n$ and $n \rightarrow o$, respectively, then the probability of leaving state (o), ($P_{acc}(o \rightarrow n)$) must be equal to that of entering state (n) $P_{acc}(n \rightarrow o)$ by the following

$$P_B(o) \alpha(o \rightarrow n) P_{acc}(o \rightarrow n) = P_B(n) \alpha(n \rightarrow o) P_{acc}(n \rightarrow o) \quad [1.24]$$

In the Metropolis method α is chosen to be a symmetric matrix, namely $\alpha(o \rightarrow n) = \alpha(n \rightarrow o)$ so the acceptance probability is

$$P_{acc}(o \rightarrow n) = \min\left(1, \frac{P_B(n)}{P_B(o)}\right) \quad [1.25]$$

Computing Vapor-Liquid Equilibrium Curve (VLEC)

Non-bonded interactions between guest molecules are fitted to reproduce specific properties, such as the vapor-liquid equilibrium curve. Those are obtained using MC simulations in the Gibbs ensemble.

The two coexisting phases (vapor and liquid) are simulated simultaneously in two separate boxes where the temperature, the total number of particles in the two boxes (this number depends on the density of the molecule and the size of the boxes), and the total volume of the two boxes are kept fixed. A change of the volume of one box (box 1) is made, while the volume of the other box (box 2) also changes in the same proportion. The thermodynamic conditions for the equilibrium are: equal chemical potential (μ), equal pressure (P), and equal temperature (T).

Computing adsorption

Adsorption isotherms, Henry coefficients, and isosteric heats of adsorption are obtained using MC simulations.

Monte Carlo simulations in the grand-canonical ensemble (GCMC) are usually used to obtain **adsorption isotherms**. In this ensemble, the temperature T , volume V , and chemical potential μ of the adsorbed molecules are kept fixed. During grand-canonical Monte Carlo simulations one had to add or remove particles from the system. These particles are exchanged with a reservoir at the same temperature and chemical potential. Hence, the number of molecules fluctuates and during the simulation the average number of adsorbed molecules is computed. The chemical potential (μ) is directly related to the fugacity f by

$$\mu(T, p) = \mu^0 + RT \ln f \quad [1.26]$$

and the fugacity is related to the pressure p by

$$f = \emptyset p \quad [1.27]$$

where \emptyset is the fugacity coefficient computed directly from the Peng-Robinson equation of the state of the vapor in the reservoir.

In these simulations, the insertion of a particle at a random position will be rejected if the particle is added on top of one of the atoms of the porous material or other adsorbed molecules. For big molecules, random insertion becomes very inefficient as the probability that one of the atoms in the chains overlaps with the porous materials atoms increases enormously with chain length. Therefore, conventional Monte Carlo simulations can be time-consuming for these molecules. Configurational-bias Monte Carlo technique (CBMC) makes possible the insertion of this type of molecules avoiding overlap with the framework. This technique constructs a long molecule segment by segment. To generate the new configuration of a molecule, we use the following steps based on the method developed by Rosenbluth and Rosenbluth[55]. For each segment we generate a set of k trial positions according to the internal energy and compute the external energy $U_i^{ext}(j)$ of each trial position j of segment i . The new trial orientation is selected with a probability

$$P_{i(j)} = \frac{e^{-\beta U_i^{ext}(j)}}{\sum_{l=1}^k e^{-\beta U_i^{ext}(l)}} = \frac{e^{-\beta U_i^{ext}(j)}}{w(i)} \quad [1.28]$$

and added to the chain. The procedure is repeated until the entire molecule has been grown. The number of trial positions is set to 10 in this work. Then, we compute the Rosenbluth factor of the new configuration

$$W^{new} = \prod_i w(i). \quad [1.29]$$

To compute the old Rosenbluth factor W^{old} of an already existing chain, $k - 1$ trial positions are generated for each segment. These positions and the previous one form the set of k trial orientations. The Rosenbluth weight $\langle W^{IG} \rangle$ of the reference state of the ideal gas is needed to compare with real experimental data. This algorithm is used in grand-canonical (μ VT), canonical (NVT), and Gibbs ensemble simulations.

Absolute adsorption is generally considered in simulations. Nevertheless, when we compare with experimental data “excess adsorption” is needed. “Excess adsorption” provides the average number of molecules in the pores in excess above the number of molecules that would occupy the free volume at bulk-gas conditions[56-59]. This can be calculated by the equation

$$n_{ex} = n_{abs} - V^g \rho^g \quad [1.30]$$

where V^g is the pore volume and ρ^g is the gas-phase density. We obtain the value of V^g measurement the helium adsorption by simulation[59].

Henry coefficients (K_H) and **isosteric heats of adsorption at zero loading** (Q_{st}^0) inform about how much the adsorbate can adsorb under dilute conditions and about the adsorption behavior with temperature. These variables are computed in the canonical ensemble. In this ensemble, the number of particles N , the temperature T , and the volume V are constant.

For calculating the Henry coefficient and the isosteric heat of adsorption at zero loading of molecules in porous materials, simulations in the limit of zero loading are necessary. Concerning to the simulations, zero loading implies simulations with only one molecule present in the system. Henry coefficients are directly related to the excess free energy of the adsorbed molecules. They can be calculated from the expression[52]

$$K_H = \frac{1}{RT\rho_f} \frac{\langle W \rangle}{\langle W^{IG} \rangle} \quad [1.31]$$

where T is the temperature, R is the gas constant, ρ_f is the density of the framework, $\langle W \rangle$ is the Rosenbluth factor of the single chain molecule in porous materials, and $\langle W^{IG} \rangle$ is the Rosenbluth factor of the molecule in the ideal gas.

The ensemble average potential energy of the host–guest system ($\langle U_{hg} \rangle$), the energy of the isolated chain molecule in the ideal gas ($\langle U_g \rangle$), and the average host energy ($\langle U_h \rangle$) (zero for a rigid framework) are computed from two independent simulations of a single chain: a NVT simulation of a chain molecule adsorbed in the framework and a NVT simulation of an isolated chain in the ideal gas phase.

In the limit of zero loading the isosteric heat of adsorption can be obtained from the derivative of the Henry constant from the Clausius-Clayperon equation. However it is more efficient to calculate it directly from the energies of the system[52]

$$Q_{st}^0 = RT - \Delta U = RT - (\langle U_{hg} \rangle - \langle U_h \rangle - \langle U_g \rangle). \quad [1.32]$$

This method of energy differences is very efficient for pure silica structures but it is unsuitable to compute the isosteric heat of adsorption in structures with non-framework cations as same as at low to intermediate loading. When cations move around the energies of cation–cation, cation–framework energies are very large and the final result consists of the subtraction of two very large energy values. The standard error is difficult to reduce in such a system. In 2008 Vlucht et al. resolved the impediment by proposing the Widom test particle method making use of as much cancellation in energy terms as possible. The method provides significantly better and reliable results. More information about this new method can be found in literature[60].

Several Monte Carlo moves[53] can be employed during a simulation in the ensembles mentioned above: the canonical ensemble, the grand-canonical ensemble, and the Gibbs ensemble. For all ensembles we use

- Translation. A molecule is selected at random and given a random displacement. The maximum displacement is taken in such a way that the acceptance probability is on average 50% of the moves.
- Rotation. A molecule, which consists of more than one interaction center, is selected at random and given a random rotation. The center of rotation is the center of mass. The maximum rotation angle is set such that 50% of the moves are accepted.
- Regrowth. A molecule is selected at random and is either completely or partially regrows at a random position. This move is essential for canonical ensemble to change the internal configuration of a molecule.

Additional moves are used in grand-canonical ensemble

- Insertion. A molecule is inserted at a random position.
- Deletion. A randomly selected molecule is deleted. This move can be considered as the reverse process of the previous move.
- Identity change. This move is only used for mixtures. One of the components is selected at random and an attempt is made to change its identity.

Computing diffusion

Diffusion of guest molecules inside the pores of these materials strongly influences the performance of the structure in many potential applications. From a simulation point of view, computing diffusion coefficients is challenging, and several publications on this topic have been published recently[61-68].

The first simulation studies for diffusion of guest molecules in confined systems focused on self-diffusivities[69] calculations for a single adsorbed component using equilibrium Molecular Dynamics (MD) simulations. This diffusion coefficient quantifies motion of single molecules at equilibrium. With growing computer the simulation studies have gradually shifted towards computing self-diffusivities for mixtures[70-72] as well as transport diffusivities[73-80] that are the relevant diffusion coefficients for use in technological applications. Transport diffusion coefficient describes net mass transfer in the presence of a concentration gradient in the adsorbed species (non-equilibrium conditions). From a phenomenal point of view, there are three equivalent approaches that correspond to the Fick, the Onsager, and the Maxwell-Stefan formulations[75,81,82].

The earliest attempts to compute transport diffusivities in porous materials were achieved for methane in MFI[76] and LTA[77] using non-equilibrium MD methods. Self-diffusivities are easier to obtain from MD than the other diffusion coefficients. For this reason it is often the only diffusion coefficient that is examined in simulation studies. However, most recently, the increase of computer power made it possible to compute transport diffusivities from equilibrium MD simulations[78,80,83,84], and also to extend those calculations for obtaining diffusivities over loading providing insights into the mechanisms that control the molecular traffic along the pores[85,86].

In conventional NVE molecular dynamics simulations, the total energy E , the number of particles N , and the volume V are constant. In MD simulations successive configurations of the system are generated by integrating Newton's equations of motion, which then yield trajectories that describe the positions, velocities, and accelerations of the particles as they vary with time.

One can measure the Mean-Squared Displacement (MSD) of an individual particle by taking the gradient of the MSD at long times. The self-diffusivity coefficient can be computed from the Einstein equation.

$$D_{\alpha}^S = \frac{1}{2dN_{\alpha}} \lim_{t \rightarrow \infty} \frac{d}{dt} \left\langle \sum_{i=1}^{N_{\alpha}} [r_i^{\alpha}(t) - r_i^{\alpha}(0)]^2 \right\rangle \quad [1.33]$$

where D_α^S is the self-diffusivity of component α , N_α represents the number of molecules of component α , d is the spatial dimension of the system, t is the time, and r_i^α is the center of mass of molecule i of component α . The angular brackets denote that the quantity is an ensemble average property.

The diffusion coefficients can be calculated to each x , y , and z direction individually (when the dimension of the system is taken in each case as $d = 1$). In the same fashion it can be applied to the two dimensional case $d = 2$, or to the three dimensional system $d = 3$. In this last case, the overall diffusion coefficient is given by

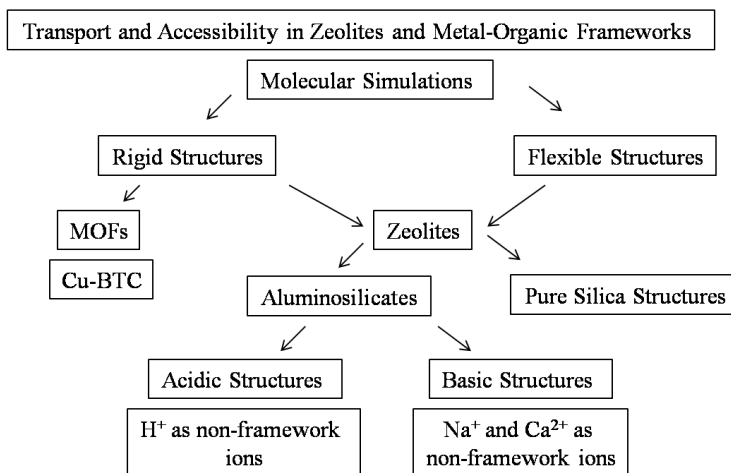
$$D = \frac{D_x + D_y + D_z}{3} \quad [1.34]$$

Computing infrared spectra (IR)

Among the experimental techniques, the methods of vibrational spectroscopy are some of the most extensively used to study the dynamics of the porous materials. The total interpretation of their vibrational spectra generally needed the use of some computational methods which permit an assignment of the bands and a quantitative description of the influence of different parameters on the spectra. The IR spectra are calculated from the molecular dynamics trajectories by the Fast Fourier Transform (FFT) of the total dipole correlation function[87]. Our code samples the dipole components every 4 time steps. Since the MD simulations used 1 fs time step, this means that every 4 fs a dipole moment is calculated. The spectra had a bandwidth of approximately 8300 cm^{-1} , therefore ruling out aliasing artefacts. Multiple time origins at half-overlapping sampling times are used in calculating the dipole correlation function, and the spectrum is smoothed with a triangular window function. The intensities obtained by this method are qualitative because the quantum corrections needed to give completely accurate intensities are impractical for such a large system.

1.5 Context and scope of this thesis

The context and scope of this thesis is based on the following scheme:



Work scheme followed in this thesis.

Molecular simulations were firstly performed for rigid frameworks. Two types of porous materials were studied: zeolites and Metal-Organic Frameworks (MOFs). The studied zeolites can be built a) from silicon and oxygen atoms (pure silica zeolites), b) from silicon, aluminum, and oxygen atoms with sodium and/or calcium as non-framework cations (basic zeolites), and c) from silicon, aluminum, and oxygen atoms with protons as non-framework ions (acidic zeolites). In these structures we study adsorption and diffusion processes of alkanes, CO₂, and N₂. Concerning MOFs, adsorption properties of short alkanes, N₂, and O₂ in a Cu-BTC structure were studied. Also, we analyzed the preferential sites of adsorption of these guest molecules in the mentioned structure.

Molecular simulations using flexible models were performed to study the effect of molecular loading on structural phase transitions.

For all the studies, molecular simulation techniques described in the first chapter have been used.

Study of the adsorption and diffusion properties of polar and non-polar molecules in rigid pure silica zeolites. (Chapters 2 and 3)

In chapter 2 adsorption properties of CO₂, N₂, and CH₄ in all-silica zeolites (MFI, MOR, ISV, ITE, CHA, and DDR) were studied using molecular simulations. We performed adsorption isotherms for a wide range of pressures and temperatures and for single components as well as binary and ternary mixtures varying bulk compositions. Our simulations provided a tool to predict the adsorption behavior of multicomponent

mixtures and the location of the molecules for a given temperature, pressure, and bulk chemical composition.

In chapter 3, molecular dynamics simulations were carried out to determine self-diffusivities of CH₄ and CO₂ for pure components and in 50-50 mixtures for a range of molar loadings in MFI, CHA, and DDR rigid zeolites. The obtained results showed that the diffusion selectivity is strongly dependent on both the loading and choice of zeolite.

Study of the adsorption properties of linear alkanes in rigid aluminosilicates and the effect of the aluminum location in the structure. (Chapters 4, 5, 6, 7, and 8)

In chapters 4 and 5 we performed Configurational-bias Monte Carlo to provide adsorption isotherms, Henry coefficients, and heats of adsorption of linear alkanes in sodium exchanged MFI-, MOR-, and FAU-type zeolites. In this section empirical expressions were derived from simulation data to describe the adsorption properties in these zeolites. In the low coverage regime we provided expressions that adequately describe the Henry coefficients and heats of adsorption of *n*-alkanes as a function of sodium density and temperature. Our results compared extremely well to available experimental data.

In chapter 6 we developed a new force field including calcium-type ions to describe the adsorption properties of linear alkanes in Ca, Na-LTA-type zeolite. Having obtained our force field, and confirmed its reliability on predictions outside the calibration set, we studied a) the heats of adsorption and Henry coefficients as a function of chain length and b) the effect of cations in LTA-type zeolites.

In chapters 7 and 8 we proposed a computational method to a) characterize framework aluminum in aluminosilicates, b) identify the most likely positions of aluminum TON, FER, and MOR zeolites, and c) understand their different adsorption behaviors in detail. Our simulation results showed that the location of aluminum affects the positions of the ions, and thus influences the adsorption.

Study of the molecular adsorption in Cu-BTC metal-organic framework and identification of the preferential adsorption sites. (Chapter 9)

We analyzed here the adsorption of several quadrupolar (N₂ and O₂) and non-polar (methane, ethane, and propane) gases on Cu-BTC by Monte Carlo simulations.

Furthermore, we determined the preferential adsorption sites for the different adsorbates on the structure as a function of pressure and coverage.

Study the argon adsorption processes in MFI-type zeolite. (Chapter 10)

In this chapter, a new approaching into the argon adsorption processes at 77 K was proposed by a combined insight using both experiments and molecular simulations. The presence of a substep on the argon adsorption isotherm of MFI at cryogenic temperature was previously corroborated with a variety of experimental studies, but its origin was still unclear. Our results showed that the interplay between the guest molecules and the flexible host structure could be the responsible for kinks/steps in the isotherms.

The last chapter (Chapter 11) summarizes the main conclusions of this work.

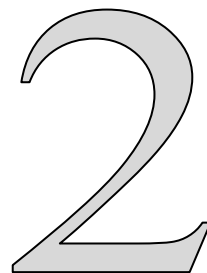
Bibliography

- [1] Krishna, et al. *Chemical Society Reviews* **2002**, 31, 185.
- [2] Martin-Calvo, et al. *Physical Chemistry Chemical Physics* **2008**, 10, 7085.
- [3] Baerlocher *Atlas of Zeolite Framework Types*, 6th ed.; Elsevier: Amsterdam, 2007.
- [4] Chen, et al. *Science* **2001**, 291, 1021.
- [5] Cheetham and Rao. *Science* **2007**, 318, 58.
- [6] Rowsell, et al. *Science* **2005**, 309, 1350.
- [7] Zhao, et al. *Science* **2004**, 306, 1012.
- [8] Eddaoudi, et al. *Science* **2002**, 295, 469.
- [9] Li, et al. *Nature* **1999**, 402, 276.
- [10] Mueller, et al. *Journal of Materials Chemistry* **2006**, 16, 626.
- [11] Kondo, et al. *Angewandte Chemie-International Edition in English* **1997**, 36, 1725.
- [12] Ferey and Serre. *Chemical Society Reviews* **2009**, 38, 1380.
- [13] Natarajan and Mahata. *Chemical Society Reviews* **2009**, 38, 2304.
- [14] Li, et al. *Chemical Society Reviews* **2009**, 38, 1477.
- [15] Czaja, et al. *Chemical Society Reviews* **2009**, 38, 1284.
- [16] Kitagawa, et al. *Angewandte Chemie-International Edition* **2004**, 43, 2334.
- [17] Ferey. *Chemical Society Reviews* **2008**, 37, 191.
- [18] Kitagawa and Matsuda. *Coordination Chemistry Reviews* **2007**, 251, 2490.
- [19] Thomas. *Dalton Transactions* **2009**, 1487.
- [20] Baerlocher, et al. *Atlas of Zeolite Structure Types*, sixth revised edition ed.; Elsevier: London, 2007.
- [21] Jaramillo and Auerbach. *Journal of Physical Chemistry B* **1999**, 103, 9589.
- [22] Calero, et al. *Journal of the American Chemical Society* **2004**, 126, 11377.

- [23] Beerdsen, et al. *J. Phys. Chem. B* **2002**, *106*, 10659.
- [24] Beerdsen, et al. *Journal of Physical Chemistry B* **2003**, *107*, 12088.
- [25] <http://www.ccdc.cam.ac.uk/>.
- [26] Rappe, et al. *Journal of the American Chemical Society* **1992**, *114*, 10024.
- [27] Mayo, et al. *Journal of Physical Chemistry* **1990**, *94*, 8897.
- [28] Bezus, et al. *Journal of the Chemical Society-Faraday Transactions II* **1978**, *74*, 367.
- [29] Leroy, et al. *Physical Chemistry Chemical Physics* **2004**, *6*, 775.
- [30] Greathouse and Allendorf. *Journal of the American Chemical Society* **2006**, *128*, 10678.
- [31] Dubbeldam, et al. *Angewandte Chemie-International Edition* **2007**, *46*, 4496.
- [32] Amirjalayer, et al. *Angewandte Chemie-International Edition* **2007**, *46*, 463.
- [33] Han and Goddard. *Journal of Physical Chemistry C* **2007**, *111*, 15185.
- [34] Demontis, et al. *Journal of Physical Chemistry* **1988**, *92*, 867.
- [35] Nicholas, et al. *J. Am. Chem. Soc.* **1991**, *113*, 4792.
- [36] Ryckaert and Bellemans. *Faraday Discussions* **1978**, 95.
- [37] Harris and Yung. *Journal of Physical Chemistry* **1995**, *99*, 12021.
- [38] Murthy, et al. *Molecular Physics* **1980**, *41*, 1387.
- [39] Mellot and Lignieres. *Molecular Simulation* **1996**, *18*, 349.
- [40] Nath, et al. *Journal of Chemical Physics* **1998**, *108*, 9905.
- [41] Martin and Siepmann. *J. Phys. Chem. B* **1998**, *102*, 2569.
- [42] Smit and Siepmann. *Journal of Physical Chemistry* **1994**, *98*, 8442.
- [43] Jorgensen and Swenson. *Journal of the American Chemical Society* **1985**, *107*, 1489.
- [44] Vlugt, et al. *J. Am. Chem. Soc.* **1998**, *120*, 5599.
- [45] Lubna, et al. *Journal of Physical Chemistry B* **2005**, *109*, 24100.
- [46] Zeng, et al. *Separation and Purification Technology* **2007**, *55*, 82.
- [47] Zeng, et al. *Industrial & Engineering Chemistry Research* **2007**, *46*, 242.
- [48] Ryckaert, et al. *Molecular Physics* **1989**, *67*, 957.
- [49] Kiselev, et al. *Zeolites* **1985**, *5*, 261.
- [50] Vlugt, et al. *J. Phys. Chem. B* **1999**, *103*, 1102.
- [51] Bourasseau, et al. *Journal of Physical Chemistry B* **2002**, *106*, 5483.
- [52] Dubbeldam, et al. *Journal of Physical Chemistry B* **2004**, *108*, 12301.
- [53] Frenkel and Smit *Understanding Molecular Simulations: From Algorithms to Applications*, second edition ed.; Academic Press: San Diego, CA, 2002.
- [54] Dubbeldam, et al. *Physical Review Letters* **2004**, 93.
- [55] Rosenbluth and Rosenbluth. *Journal of Chemical Physics* **1955**, *23*, 356.
- [56] Macedonia, et al. *Langmuir* **2000**, *16*, 3823.
- [57] Myers. *Aiche Journal* **2002**, *48*, 145.

- [58] Myers and Monson. *Langmuir* **2002**, *18*, 10261.
- [59] Talu and Myers. *Aiche Journal* **2001**, *47*, 1160.
- [60] Vlugt, et al. *Journal of Chemical Theory and Computation* **2008**, *4*, 1107.
- [61] Dubbeldam and Snurr. "Recent developments in the molecular modeling of diffusion in nanoporous materials"; 3rd International Conference on Foundations of Molecular Modeling and Simulation (FOMMS), 2006, Blaine, WA.
- [62] Jobic and Theodorou. *Microporous and Mesoporous Materials* **2007**, *102*, 21.
- [63] Yashonath and Ghorai. *Journal of Physical Chemistry B* **2008**, *112*, 665.
- [64] Auerbach. *International Reviews in Physical Chemistry* **2000**, *19*, 155.
- [65] Sholl. *Accounts of Chemical Research* **2006**, *39*, 403.
- [66] Sarkisov, et al. *Molecular Physics* **2004**, *102*, 211.
- [67] Skoulidas. *Journal of the American Chemical Society* **2004**, *126*, 1356.
- [68] Snurr. Molecular Modeling of Metal-Organic Frameworks. In *Metal-Organic Frameworks: Design and Application*; MacGillivray, Ed.; Wiley-VCH, 2010.
- [69] Demontis and Suffritti. *Chem. Rev.* **1997**, *97*, 2845.
- [70] Snurr and Karger. *Journal of Physical Chemistry B* **1997**, *101*, 6469.
- [71] Gergidis and Theodorou. *Journal of Physical Chemistry B* **1999**, *103*, 3380.
- [72] Jost, et al. *Journal of Physical Chemistry B* **1998**, *102*, 6375.
- [73] Krishna and van Baten. *Chemical Engineering Science* **2008**, *63*, 3120.
- [74] Krishna and van Baten. *Microporous and Mesoporous Materials* **2008**, *109*, 91.
- [75] Krishna and van Baten. *Chemical Engineering Science* **2009**, *64*, 870.
- [76] Maginn, et al. *Journal of Physical Chemistry* **1993**, *97*, 4173.
- [77] Fritzsche, et al. *Zeitschrift Fur Physikalische Chemie-International Journal of Research in Physical Chemistry & Chemical Physics* **1995**, *189*, 211.
- [78] Arya, et al. *Journal of Chemical Physics* **2001**, *115*, 8112.
- [79] Sholl. *Industrial & Engineering Chemistry Research* **2000**, *39*, 3737.
- [80] Hoogenboom, et al. *Journal of Chemical Physics* **2000**, *113*, 6875.
- [81] Krishna and Baur. *Separation and Purification Technology* **2003**, *33*, 213.
- [82] Krishna and van Baten. *Journal of Physical Chemistry B* **2005**, *109*, 6386.
- [83] Sastre, et al. *J. Phys. Chem. B* **2000**, *104*, 416.
- [84] Sastre, et al. *Journal of Physical Chemistry B* **1999**, *103*, 5187.
- [85] Derouane and Gabelica. *Journal of Catalysis* **1980**, *65*, 486.
- [86] Krishna, et al. *Journal of Physical Chemistry B* **2004**, *108*, 14820.
- [87] Berens and Wilson. *J. Chem. Phys.* **1981**, *74*(9), 4872.

The adsorption properties of CO₂, N₂, and CH₄ in all-silica zeolites were studied using molecular simulations. Adsorption isotherms for single components in MFI were both measured and computed showing good agreement. In addition simulations in other all silica structures were performed for a wide range of pressures and temperatures and for single components as well as binary and ternary mixtures with varying bulk compositions. The adsorption selectivity was analyzed for mixtures with bulk composition of 50:50 CO₂/CH₄, 50:50 CO₂/N₂, 10:90 CO₂/N₂, and 5:90:5 CO₂/N₂/CH₄ in MFI, MOR, ISV, ITE, CHA, and DDR showing high selectivity of adsorption of CO₂ over N₂ and CH₄ that varies with the type of crystal and with the mixture bulk composition.



E. García-Pérez, J.B. Parra, C.O. Ania, A. García-Sánchez, J.M. van Baten, R. Krishna, D. Dubbeldam, and S. Calero

A Computational Study of CO₂, N₂, and CH₄ Adsorption in Zeolites

2.1 Introduction

The development of new advanced adsorbents for gas separation in many industrial applications via adsorption processes is receiving increasing attention. These materials need to be characterized for a wide variety of gases. Zeolites as adsorbents are rapidly becoming the technology of choice for the petroleum and chemical industry for minimizing emissions to the environment, of mainly volatile organic compounds. Besides their well-known importance in many industrial catalytic processes, zeolites are currently finding broad applications in industry, especially in environmentally sensitive industrial processes. Separation of methane, nitrogen, and carbon dioxide mixtures is a challenging research topic for both environmental and economical reasons. From the environmental point of view, it is necessary to develop effective separation technologies to reduce the carbon dioxide emissions that are noticeably increasing due to the use of fossil fuels. From the economical point of view, the removal of carbon dioxide from natural gas and the recovery of methane from landfill gas (containing methane, carbon dioxide, and small amounts of nitrogen) are examples of interesting separations. Among the potential routes explored for gas separations, adsorption processes involving zeolites have shown an increasing importance because these materials have a high thermal, mechanical, and chemical stability. The zeolite pores have a size comparable to the molecular dimensions

of many substances[1] and therefore they show peculiar mechanisms of diffusion in which the framework geometry plays the most important role[2-5].

Zeolites are aluminosilicates with crystalline structures constructed from TO_4 tetrahedra ($T = \text{Si}, \text{Al}$). These crystals are characterized by a uniform three-dimensional pore structure, with pores that vary in shape and of well-defined diameters of molecular dimensions. Most of the zeolitic materials investigated to date for separations of mixtures involving carbon dioxide, nitrogen, and methane belong to the MFI-type[6-12], although other structures such as MOR[13], LTA[14,15], FAU[16-18], DD3R[19,20], CHA[21], and SAPO34[22-24] have also been studied. The mechanism for separation in zeolites can be quite complex since variations in the size and geometry of the cavities and pores will contribute to the overall performance of the zeolite[5,25].

Molecular simulations are currently playing an important role in developing our understanding of the relation between microscopic and macroscopic properties of confined molecular fluids in zeolites[2,3,26]. We use here molecular simulations to analyze the influence of both, structure, and bulk mixture composition on the adsorption of CH_4 , CO_2 , and N_2 , and on the selectivity performance of *all silica zeolites*. A good knowledge of the adsorption properties of these materials can be helpful to explain the underlying mechanisms of adsorption and diffusion processes, as well as to identify further applications of zeolites as catalysts and adsorbents[27].

2.2 Methodology

The adsorption isotherms were computed using Monte Carlo (MC) simulations in the grand canonical (GC) ensemble. The zeolite lattices are assumed rigid during simulations, with static atomic charges that are assigned by choosing $q_{\text{Si}} = +2.05$ and $q_{\text{O}} = -1.025$, following the work of Jaramillo and Auerbach[28]. The crystallographic data are available elsewhere[29]. The interactions between guest molecules adsorbed (CO_2 , N_2 , and CH_4) with other adsorbates and with the zeolite are modeled by Lennard-Jones and Coulombic potentials. The Coulombic interactions in the system are calculated by Ewald summation for periodic systems[30]. The interactions dominated between adsorbed molecules and the zeolite are dispersive forces between the pseudo-atoms and the oxygen atoms of the zeolite[31,32] and the interactions of silicon and aluminum are considered through an effective potential with only the oxygen atoms. The internal structure of the adsorbate and the adsorbate–adsorbate interactions are as important as the properties dominated by the strong interactions with the force field produced by the zeolite (adsorbate–adsorbent). We are using force field parameters that accurately reproduce the properties of pure gas adsorption of CO_2 , N_2 , and CH_4 , as well as their mixtures in

different types of all-silica zeolites. Most of these force field parameters were fitted to reproduce the adsorption isotherms in silicalite and validated in other pure silica structures. CH₄ molecules are described with a united atom model, in which each molecule is treated as a single interaction center[33]. CO₂ molecules are taken linear and rigid with bond length C–O of 1.16 Å according to the model developed by Harris and Young[34]. N₂ molecules are modeled as a dumbbell with a rigid interatomic bond of 1.098 Å. The partial charges of N₂ and CO₂ are distributed along each molecule to reproduce experimental quadrupole moment. The interaction between adsorbed molecules is described with Coulombic and Lennard-Jones terms. The parameters for methane are taken from Dubbeldam et al.[35] and Calero et al.[36] In this work we are using the model proposed by Harris et al.[34] for CO₂ and the model proposed by Murthy et al.[37] for N₂. These models were also used by Watanabe et al.[38] and Makrodimitris et al.[9] The partial charges and Lennard-Jones parameters used in our simulations are listed in Table 2.1. The Lennard-Jones potentials are shifted and cut at 12 Å. The number of unit cells in the simulation box was chosen such that the minimum length in each of the coordinate directions was larger than 24 Å. Periodic boundary conditions were employed. Further GCMC details are available in previous publications[35,36,39].

Experimental adsorption isotherms were performed for nitrogen and carbon dioxide in MFI at several temperatures. The zeolite used in this investigation was kindly supplied by ITQ[40] and corresponds to a virtually pure porous crystalline silicon dioxide; the highly siliceous form of silicalite-1 with the MFI crystal structure. The porous network of the zeolite was characterized by means of helium density (2.36 g cm⁻³) and N₂ adsorption isotherm at 77 K (see Figure 2.1). In good agreement with literature[41], the experimental N₂ isotherm at 77 K silicalite exhibits two adsorption sub-steps. The initial adsorption step up to $p/p_0 < 0.1$ corresponds to microporous pore filling. The second sub-step occurs at relative pressures between 0.1–0.3 and the volume adsorbed of nitrogen increase by 25 cm³ STP g⁻¹. This behavior has been interpreted as an adsorbate transition from a lattice fluid-like phase to crystalline-like solid one (i.e., solidification type phase transition)[41].

Table 2.1 Partial charges and Lennard-Jones force field parameters for adsorbent–adsorbate and adsorbate–adsorbate interactions. Top-left corner ϵ/k_B (K). Bottom-right corner σ (Å).

	O_{zeo}	CH_4	C	O_{CO_2}	N
CH_4	115	158.5	66.77	112.96	75.96
C	50.2	66.77	28.129	47.59	32.0
O_{CO_2}	84.93	112.96	47.59	80.507	54.13
N	58.25	75.96	32.0	54.13	36.4
Charge [e⁻]	-1.025	+0.6512	-0.3256	-0.40484	+0.80968

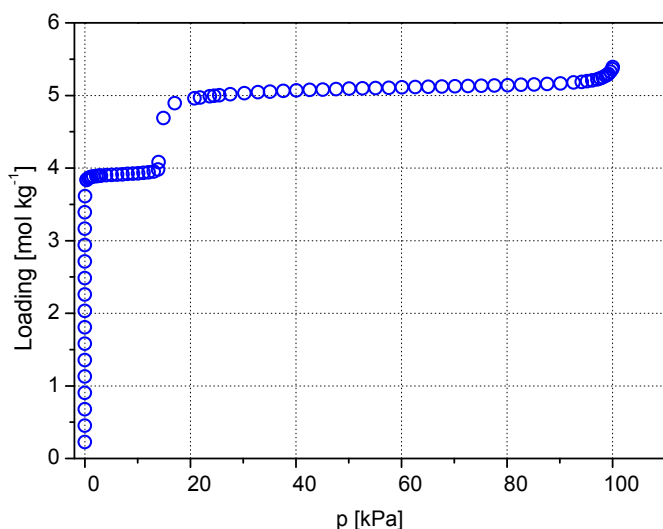


Figure 2.1 Measured adsorption isotherm of N_2 in MFI-type zeolite at 77 K.

Detailed experimental methods were reported and discussed elsewhere[42]. Briefly, prior to the adsorption measurements the samples were outgassed in-situ under vacuum at 673 K overnight to remove any adsorbed impurities. A Micromeritics ASAP 2010 gas adsorption analyzer was used to accurately measure the N_2 uptake at 77 K in the pressure range from 10^{-4} kPa to 100 kPa. The instrument was equipped with a molecular drag vacuum pump and three different pressure transducers (0.133 kPa, uncertainty within 0.12 % of reading; 1.33 kPa and 133 kPa, uncertainty within 0.15 % of reading) to enhance the sensitivity in the low-pressure range, which is especially useful in adsorption studies on

microporous materials. The CO₂ adsorption isotherms were carried out in a TriStar 3000 from Micromeritics, using a circulating temperature-controlled bath, in the pressure range from 10⁻¹ kPa up to 120 kPa. The gaseous adsorptives, N₂ and CO₂, were purchased with an ultra-high purity (i.e., 99.9992 and 99.995 %, respectively).

2.3 Results and discussion

We have performed molecular simulations to (1) reproduce our measured single component isotherms in MFI, (2) compare with available experiments of CH₄, CO₂, and N₂ single and binary mixtures in MFI, DDR, ITE, and ISV zeolites[29], (3) predict the location of the molecules in the crystal pores, and (4) obtain ternary mixture adsorption isotherms for a given bulk composition. To study the ternary mixture adsorption behavior we have selected three structures with different type of porous: MOR (structure with one-dimensional channels), MFI (structure with intersecting channels), and CHA (structures with cages separated by narrow windows).

Our computed and measured adsorption isotherms for CO₂ at 253 K, 273 K, and 303 K are shown in Figure 2.2. Additional adsorption isotherms for CO₂ and N₂ in MFI were obtained for several temperatures and compared with available previous data. Figure 2.2 shows good agreement between our computed isotherm for N₂ at 308 K and the one of Goj et al.[14] Similar good agreement is observed between the data obtained in this work for CO₂ and the experimental measurements of Zhu et al.[43], Hirotani et al.[44], Sun et al.[45], and Choudhary et al.[46] Adsorption isotherms of CO₂, CH₄, and N₂ in MOR were computed at 300 K and 210 K and compared with the isotherms of Delgado et al.[13] and Webster et al.[47] as shown in Figure 2.3 (top). The calculated isotherms show excellent agreement with experiments in all range of pressures. The small discrepancies between our results and the experimental values are attributed to the Si/Al ratio of MOR structures used in the experimental measurements. Simulations were performed for pure silica MOR whereas experimental data for methane and CO₂ were obtained for H-MOR with Si/Al = 6 and 7 protons per unit cell, and experimental data of N₂ were obtained for Na-MOR with Si/Al = 20 and 2 sodium cations per unit cell.

Figure 2.3 (bottom) compares the simulated isotherms of CO₂, CH₄, and N₂ in CHA with the experimental isotherms of Li et al.[48] for SAPO-34—an isotype of CHA—proving very good agreement up to the range of pressures used for the experimental isotherms.

The computed values for N_2 are also in excellent agreement with previous data of Grey et al.[21]

Besides computing the adsorption of pure components in various zeolites, we have performed simulation on mixtures of the selected gases. Figure 2.4 shows the obtained adsorption isotherms for equimolar mixtures of CO_2/N_2 in MFI at 308 K (Figure 2.4-top) and the computed adsorption selectivity for the equimolar and the 10:90 CO_2/N_2 bulk mixture in MFI at the same temperature (Figure 2.4-bottom). Similar calculations were performed for ITE (50:50 bulk mixture) and ISV (50:50 and 10:90 bulk mixture) at 498 K and 308 K, respectively.

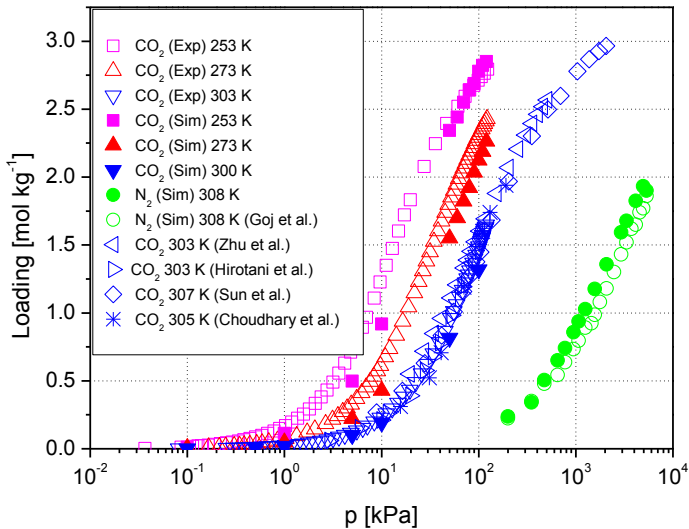


Figure 2.2 Computed (Sim) and measured (Exp) adsorption isotherms of CO_2 and N_2 in MFI-type zeolite. Previous experimental[43-46] and simulation[14] data are included for comparison.

The resulting simulation data are shown in Figure 2.5. The selectivity is defined as the ratio of adsorbed molar fraction over bulk molar fraction. Our results are consistent with the previous atomistic results of Goj et al.[14] proving for all the structures the preferential adsorption of CO_2 over N_2 . The preferential adsorption of carbon dioxide is partially due to its large quadrupole moment that strengthens the adsorbate–adsorbent Coulombic interactions, thereby increasing the adsorption in the structure.

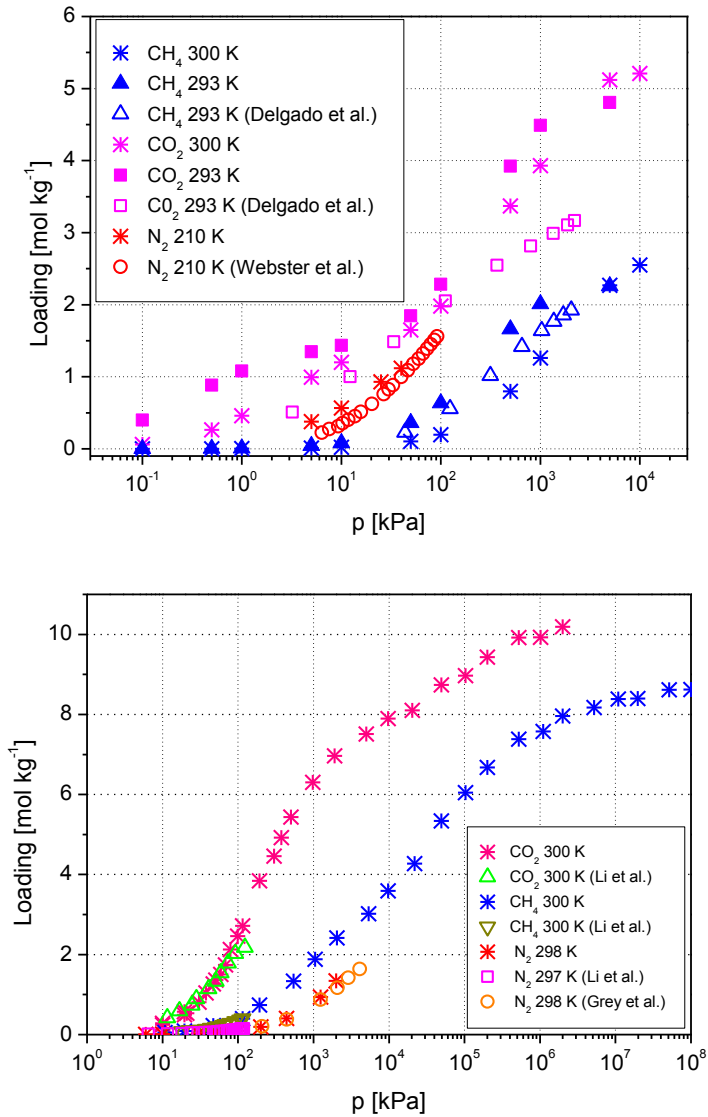


Figure 2.3 Computed adsorption isotherms of CO₂, CH₄, and N₂ in (top) MOR-type zeolite and (bottom) CHA-type zeolite at several temperatures. Available experimental data are included for comparison[13,21,47,48].

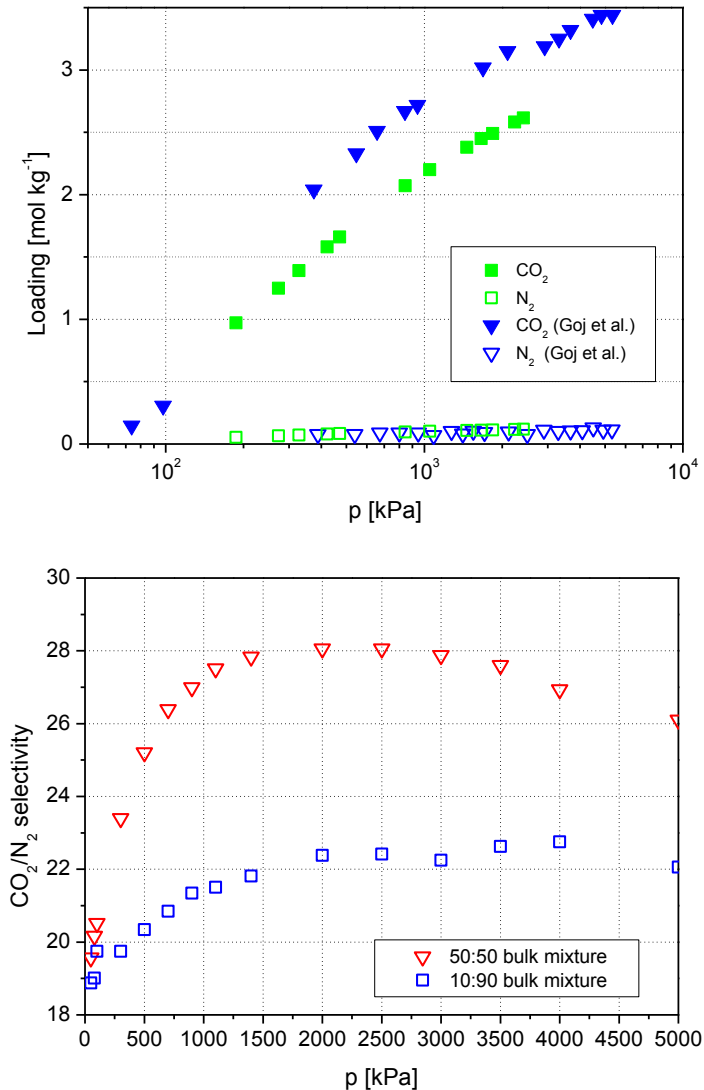


Figure 2.4 Molecular simulations of CO₂/N₂ mixtures in MFI at 308 K. (Top) Adsorption isotherm of the equimolar bulk mixture compared with previous simulation data[14]. (Bottom) CO₂/N₂ selectivity for the equimolar (50:50) and 10:90 bulk mixtures.

Similar behavior can be therefore expected during the adsorption of CO₂/CH₄ mixtures and the obtained results in MFI and DDR structures are shown in Figure 2.6. The simulated isotherms are in concordance with previous experimental results[43,49], as shown in Figure 2.6 (top). The adsorption selectivity is favorable for CO₂ in both cases and is nearly constant with increasing pressure. The adsorption of CO₂ is almost unaffected by the presence of nitrogen, but N₂ adsorption is extremely sensitive to

presence of CO_2 . Figure 2.6 (bottom) shows the isothermal-isobaric (100 kPa) gas phase adsorbed diagram for the mixture methane and carbon dioxide on DDR (298 K) and MFI (313 K). Our results indicate a fast rise in the mole fraction of CO_2 in adsorbed phases at low CO_2 fraction in gas phase. This behavior has also been observed by Himeno et al.[19] and Harlick and Tezel[50] in DDR and MFI respectively and is attributed to the dominant CO_2 adsorption in the binary system. Our results are in perfect agreement with those obtained by Himeno but show some discrepancies with the experimental data of Harlick and Tezel for MFI that can be explained by the differences in the structures.

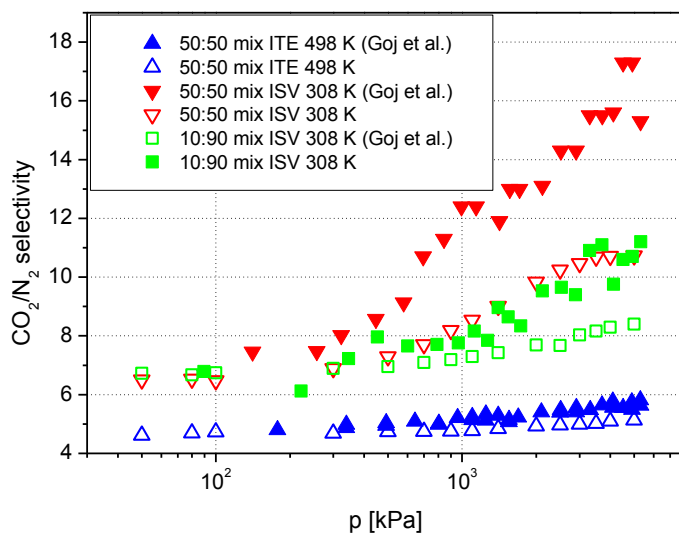


Figure 2.5 Molecular simulations of CO_2/N_2 mixtures in ITE (50:50 bulk mixture) and ISV (50:50 and 10:90 bulk mixture). Simulations were performed at 498 and 308 K, respectively and previous atomistic data are included for comparison[14].

The simulations for this work have been performed in all silica MFI whereas Harlick and Tezel used ZSM-5. As we mentioned before the Coulombic interactions between the CO_2 and the electric field of the zeolite will favor the preferential adsorption of carbon dioxide over methane in the structure. This selectivity will be enhanced in protonated aluminosilicates structures as ZSM-5 since these materials exhibit stronger local electric fields than the all silica zeolites.

The computed adsorption isotherms for 50:50 mixtures of CO_2 and CH_4 and 5:95 mixtures of CO_2 and N_2 in MOR are shown in Figures 2.7 (top) and 2.7 (bottom), respectively.

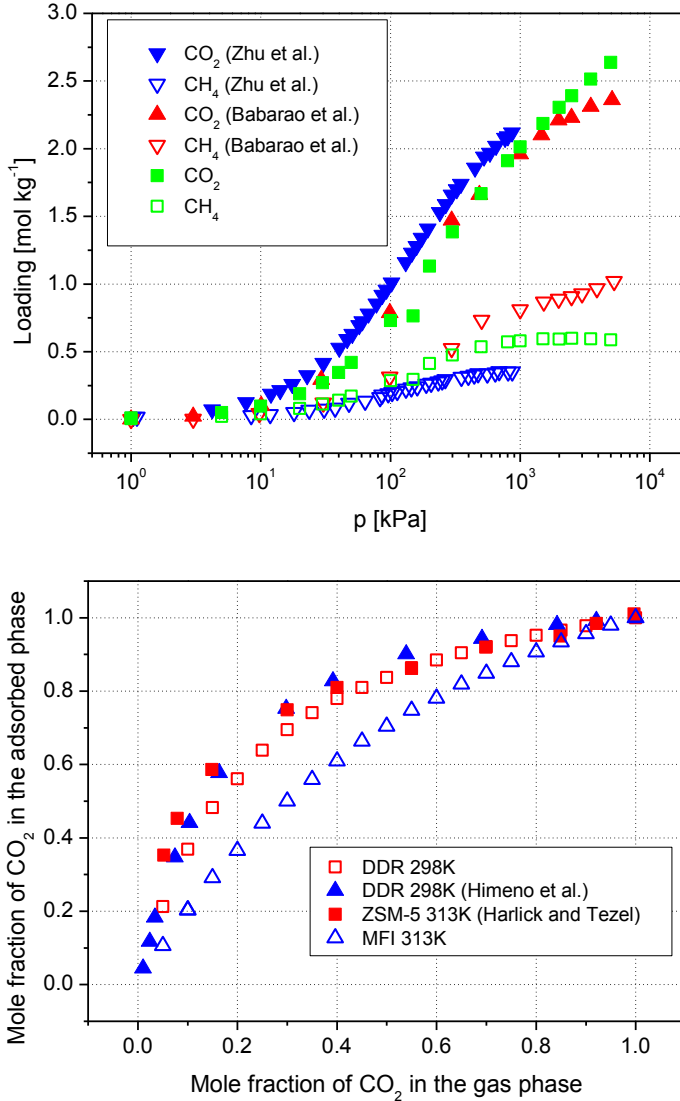


Figure 2.6 Molecular simulations of CO_2/CH_4 mixtures in zeolites compared with previous experimental[43,49,50] and theoretical[19] data. (Top) Equimolar bulk mixtures in MFI at 303 K. (Bottom) Isothermal, isobaric (100 kPa) gas phase-adsorbed-phase diagram in DDR at 298 K and MFI at 313 K.

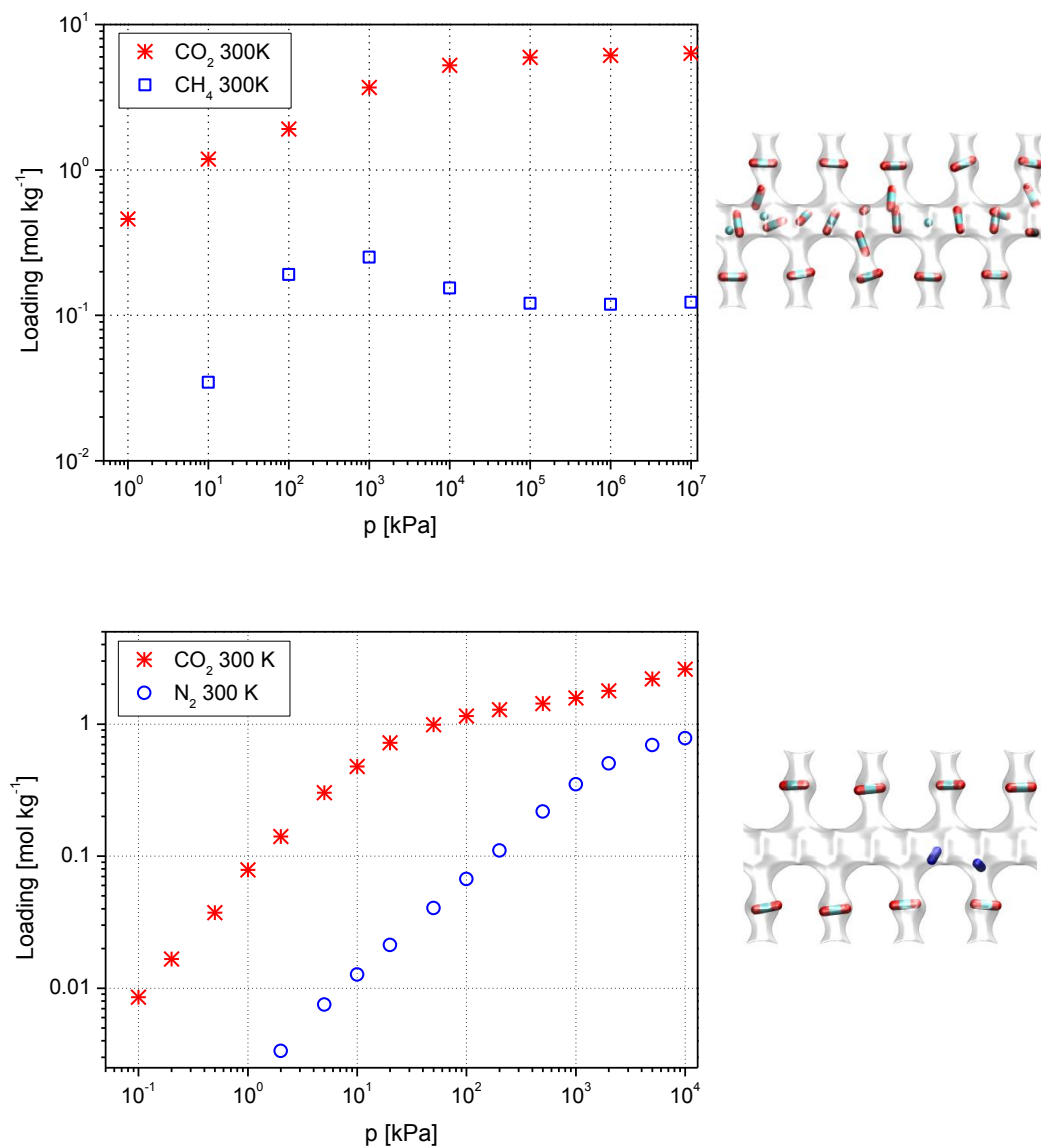


Figure 2.7 Computed adsorption isotherms of mixtures of CH₄, CO₂, and N₂ in MOR at 300 K. The snapshots show the molecular locations at 1000 kPa. (Top) 50:50 bulk CH₄/CO₂ mixture. (Bottom) 5:95 bulk CO₂/N₂ mixture.

CO₂ adsorbs stronger than methane and N₂ in this structure for all range of pressures. MOR structures consist of parallel channels with small side-pockets. These pockets are the preferred adsorption sites for small molecules (such as CO₂, N₂, and CH₄) at room

temperature. When these sites are filled, the main channels become occupied. In a mixture of CO_2 with CH_4 or N_2 , the former adsorbs preferentially in the side pockets and the latter fill then the main channels. This can be clearly observed in Figure 2.7 from the snapshots taken from our simulations at 1000 kPa and room temperature. At low pressure CO_2 molecules adsorb in the side pockets. Once these are full, they adsorb in the main channels together with the CH_4 and N_2 molecules

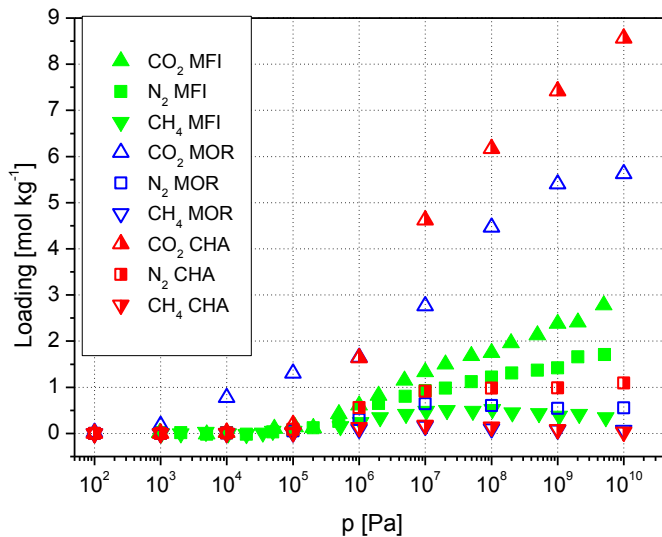


Figure 2.8 Computed adsorption isotherms of the 5:5:90 bulk CH_4 / CO_2 / N_2 mixture in MFI, MOR, and CHA zeolites at 300 K.

The adsorption isotherms for 5:5:90 ternary mixture of CH_4 , CO_2 , and N_2 were computed at 300 K for a range of pressures that spans from 0.01 to 107 kPa. Figure 2.8 shows that as for the binary mixtures, CO_2 achieves the highest adsorption in all cases. The lower or higher CO_2 adsorption selectivity is decided by the shape and the size of the crystal pore. CO_2 achieves the highest adsorption when increasing the confinement due to a combination of entropic (it is bigger than CH_4 and N_2) and Coulombic (higher quadrupole moment than CH_4 and N_2) effects. Hence, CHA with small cages separated by narrow windows provides higher selectivity than MOR -with wide one dimensional channels- and this one higher than MFI that is formed by three dimensional intersecting channels.

2.4 Conclusions

This work analyzes the adsorption behavior of CO_2 , N_2 , and CH_4 in all silica zeolites. Isotherms for pure components were measured and computed, showing in all cases good

agreement with previous available experiments. The adsorption selectivity for binary and ternary mixtures is always in favor of CO₂ and strongly depends on the type of structure and on the mixture bulk composition. Our simulations provide a tool to predict (1) the adsorption behavior of multicomponent mixtures and (2) the location of the molecules for a given temperature, pressure, and bulk chemical composition.

Bibliography

- [1] Breck *Zeolite Molecular Sieves*; Wiley: New York, 1974.
- [2] Kärger, et al. "Diffusion in zeolites" in *Handbook of Zeolite Science and Technology*; Marcel Dekker Inc.: New York, 2003.
- [3] Dubbeldam, et al. *Physical Review Letters* **2003**, 90, 245901.
- [4] Dubbeldam, et al. *Proceedings of the National Academy of Sciences of the United States of America* **2005**, 102, 12317.
- [5] Krishna, et al. *Chemical Society Reviews* **2002**, 31, 185.
- [6] Bernal, et al. *Aiche Journal* **2004**, 50, 127.
- [7] Gardner, et al. *Desalination* **2002**, 149, 435.
- [8] Harlick and Tezel. *Separation Science and Technology* **2002**, 37, 33.
- [9] Makrodimitris, et al. *Journal of Physical Chemistry B* **2001**, 105, 777.
- [10] Poshusta, et al. *Journal of Membrane Science* **1999**, 160, 115.
- [11] van den Broeke, et al. *Chemical Engineering Science* **1999**, 54, 245.
- [12] Yu, et al. *Journal of Physical Chemistry B* **2006**, 110, 4291.
- [13] Delgado, et al. *Separation and Purification Technology* **2006**, 48, 223.
- [14] Goj, et al. *Journal of Physical Chemistry B* **2002**, 106, 8367.
- [15] Nam, et al. *Journal of Chemical and Engineering Data* **2005**, 50, 72.
- [16] Hasegawa, et al. *Chemical Engineering Science* **2001**, 56, 4273.
- [17] Jia and Murad. *Journal of Chemical Physics* **2004**, 120, 4877.
- [18] Kusakabe, et al. *Aiche Journal* **1999**, 45, 1220.
- [19] Himeno, et al. *Microporous and Mesoporous Materials* **2007**, 98, 62.
- [20] Tomita, et al. *Microporous and Mesoporous Materials* **2004**, 68, 71.
- [21] Grey, et al. *Microporous and Mesoporous Materials* **2001**, 48, 203.
- [22] Bodoardo, et al. *Microporous and Mesoporous Materials* **2005**, 79, 275.
- [23] Li, et al. *Journal of Membrane Science* **2005**, 251, 59.
- [24] Poshusta, et al. *Industrial & Engineering Chemistry Research* **1998**, 37, 3924.
- [25] Schenk, et al. *Angewandte Chemie-International Edition* **2002**, 41, 2500.
- [26] Maesen, et al. *Journal of Catalysis* **2006**, 237, 278.
- [27] Garcia-Perez, et al. *Angewandte Chemie-International Edition* **2007**, 46, 276.

- [28] Jaramillo and Auerbach. *Journal of Physical Chemistry B* **1999**, *103*, 9589.
- [29] Baerlocher *Atlas of Zeolite Structure Types*, 5th ed.; Elsevier: London, 2001.
- [30] Frenkel and Smit *Understanding Molecular Simulations: From Algorithms to Applications*, second edition ed.; Academic Press: San Diego, CA, 2002.
- [31] Bezus, et al. *Journal of the Chemical Society-Faraday Transactions II* **1978**, *74*, 367.
- [32] Kiselev, et al. *Zeolites* **1985**, *5*, 261.
- [33] Ryckaert and Bellemans. *Faraday Discussions* **1978**, 95.
- [34] Harris and Yung. *Journal of Physical Chemistry* **1995**, *99*, 12021.
- [35] Dubbeldam, et al. *Journal of Physical Chemistry B* **2004**, *108*, 12301.
- [36] Calero, et al. *Journal of the American Chemical Society* **2004**, *126*, 11377.
- [37] Murthy, et al. *Molecular Physics* **1980**, *41*, 1387.
- [38] Watanabe, et al. *Molecular Simulation* **1995**, *15*, 197.
- [39] Dubbeldam, et al. *Physical Review Letters* **2004**, 93.
- [40] Lillerud *Verified synthesis of zeolitic materials*; Elsevier: Amsterdam, 2001.
- [41] Llewellyn, et al. *Langmuir* **1993**, *9*, 1852.
- [42] Parra, et al. *Adsorption Science & Technology* **2006**, *24*, 439.
- [43] Zhu, et al. *Industrial & Engineering Chemistry Research* **2006**, *45*, 767.
- [44] Hirovani, et al. *Applied Surface Science* **1997**, *120*, 81.
- [45] Sun, et al. *Journal of Physical Chemistry B* **1998**, *102*, 1466.
- [46] Choudhary and Mayadevi. *Zeolites* **1996**, *17*, 501.
- [47] Webster, et al. *Journal of the American Chemical Society* **1999**, *121*, 12127.
- [48] Li, et al. *Journal of Membrane Science* **2004**, *241*, 121.
- [49] Babarao, et al. *Langmuir* **2007**, *23*, 659.
- [50] Harlick and Tezel. *Separation and Purification Technology* **2003**, *33*, 199.

Molecular dynamics simulations were carried out to determine the self-diffusivities of CH₄ and CO₂ both for pure components and in 50–50 mixtures for a range of molar loadings in MFI, CHA, and DDR zeolites. In CHA and DDR zeolites, that consist of cages separated by narrow windows, the inter-cage hopping of molecules occur practically independent of one another and, consequently, the diffusivities of pure components are the same as in the mixture. In sharp contrast, in MFI that consists of intersecting channels, the more mobile species is slowed down significantly in the mixture.



R. Krishna, J.M. van Baten, E. García-Pérez, and S. Calero

Diffusion of CH₄ and CO₂ in MFI, CHA, and DDR Zeolites

3.1 Introduction

The separation of carbon dioxide (CO₂) from natural gas, consisting predominantly of methane (CH₄), is an important practical problem. One method for separation of CO₂ from CH₄ is to exploit the subtle differences in the molecular dimensions of the two molecules (see Figure 3.1) by allowing these molecules to adsorb and diffuse through zeolites. MFI, CHA, and DDR zeolite membranes are currently being investigated for this separation task[1-3]. For economical separations CH₄ needs to be retained at high pressures; consequently the molecular loadings within the zeolite are expected to be high. For development and design of a zeolite membrane based separation process it is essential to have a proper understanding of the diffusion characteristics of the pure components, and mixtures, within the zeolites for a wide range of loadings. The major objective of this Letter is to gain the required insights by means of Molecular Dynamics (MD) simulations. For the interpretation of the MD simulation results, Grand Canonical Monte Carlo (GCMC) simulations were carried out to determine the adsorption isotherms of the pure components.

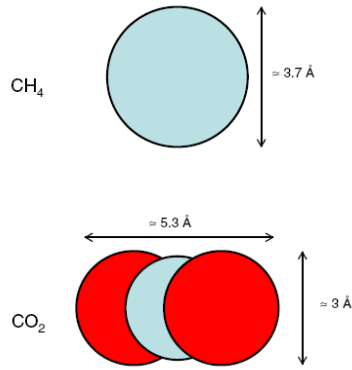


Figure 3.1 Cartoon showing the approximate molecular dimensions of CH₄ and CO₂.

3.2 GCMC and MD simulation methodologies

The adsorption isotherms for CH₄ and CO₂ in MFI, CHA, and DDR were computed using Monte Carlo (MC) simulations in the grand canonical (GC) ensemble. The crystallographic data are available elsewhere[4]. The MFI, CHA, and DDR zeolite lattices are rigid during simulations, with static atomic charges that are assigned by choosing $q_{\text{Si}} = +2.05$ and $q_{\text{O}} = -1.025$, following the work of Calero et al.[5] CH₄ molecules are described with a united atom model, in which each molecule is treated as a single interaction center[6]. CO₂ molecules are taken linear and rigid, with bond length C–O of 1.16 Å and partial charges distributed around each molecule to reproduce experimental quadrupole moment. The interaction between adsorbed molecules is described with Coulombic and Lennard-Jones terms. The parameters for methane are taken from Dubbeldam et al.[7]. For CO₂ we use the 3LJ3CB.EPM2 potential[8]. The Lennard-Jones parameters for CH₄–zeolite and CO₂–zeolite interactions are taken from Dubbeldam et al.[7] and Makrodimitris et al.[9], respectively. The Lennard-Jones potentials are shifted and cut at 12 Å. The number of unit cells in the simulation box was chosen such that the minimum length in each of the coordinate directions was larger than 24 Å. The detailed validation of the force fields used for CH₄ and for CO₂ are available elsewhere[7,10]. Periodic boundary conditions were employed. Further GCMC and MD simulation details are available in earlier publications[5,7,11-15].

The self-diffusivities, $D_{i,\text{self}}$, were computed by analyzing the mean square displacement of each component:

$$D_{i,\text{self}} = \frac{1}{2N_i} \lim_{\Delta t \rightarrow \infty} \frac{1}{\Delta t} \left\langle \left(\sum_{l=1}^{N_i} (r_{l,i}(t + \Delta t) - r_{l,i}(t))^2 \right) \right\rangle \quad [3.1]$$

In this expression N_i represents the number of molecules of species i , respectively, and $r_{l,i}(t)$ is the position of molecule l of species i at any time t . For DDR the reported diffusivities are the averages in x and y directions $D = (D_x + D_y)/2$. For other cases (MFI, CHA) the average values calculated according to $D = (D_x + D_y + D_z)/3$ are presented. In all cases reported here, the MSD values were linear in t .

3.3 Results and discussion

Figure 3.2 (left) compares the GCMC simulated isotherms for CH₄ and CO₂ in MFI with the experimental isotherm data of Zhu et al.[1] and Golden and Sircar[16]. The GCMC simulation data are obtained in terms of fugacities, and these are plotted on the x -axis rather than pressures. Up to the range of fugacities used in the experimental isotherms, 1 MPa, there is good agreement between the experiments and GCMC simulations, pointing to the validity of the force field used in the simulations. The saturation capacities $q_{i,sat}$ of CH₄ and CO₂ are determined to be 4 and 5.9 mol/kg, respectively. Figure 3.2 (right) presents the MD simulation results for the self-diffusivities both for pure components, and the values in a 50–50 mixture as a function of the total loading in MFI. The $D_{i,self}$ values of both species tends to reduce to zero as $q_{i,sat}$ is approached. Since all the vacant ‘sites’ within the zeolite framework are nearly all occupied, most of molecular jumps will be unsuccessful and the molecule will invariably return to its original site, resulting in vanishingly small diffusivities. The $D_{i,self}$ for CH₄ is higher than that of CO₂ for the entire range of loadings; the lower value for CO₂ can be attributed to the fact that it is a longer molecule (Figure 3.1), and its jumps along the channel structure of MFI occur at a slower rate than that of the more compact CH₄. Snapshots obtained from the GCMC simulations at a pressure of 10⁶ Pa, show the location of the molecules along the straight and zig-zag channels; see Figure 3.2 (bottom). The CO₂ molecules appear to align themselves perpendicular to the channels; this could be an explanation for the lower diffusivity.

From Figure 3.2 (right) we note that the $D_{i,self}$ of the more mobile CH₄ species is significantly lower in the mixture than for pure species, when compared at the same total loading q . This is to be contrasted with the fact that $D_{i,self}$ of the tardier CO₂ is practically the same in the mixture as for the pure component. The presence of the tardier molecule within the MFI channels tends to slow down the more mobile species; this effect is due to correlations in the molecular jumps[11,17,18]. The corresponding speeding up of CO₂ due to the presence of CH₄ appears to be negligibly small.

Figure 3.3 (left) compares the GCMC simulated isotherms in CHA with the experimental isotherm data of Li et al.[19] for SAPO-34, an isotype of CHA. Up to the range of

fugacities used in the experimental isotherms, 120 kPa, there is good agreement between the experiments and GCMC simulations. The $D_{i,self}$ of both species tends to reduce to zero as $q_{i,sat}$ is approached; see Figure 3.3 (right). In contrast to the results for MFI, in CHA the $D_{i,self}$ for CO_2 is higher than that of CH_4 for the entire range of loadings. The reason for this can be gleaned from the snapshots in Figure 3.3 (bottom). The windows separating two cages of CHA are only about 3.8 Å wide and can accommodate only one molecule at a time. CO_2 is a more slender molecule than CH_4 , and the energy barrier for inter-cage hopping is lower than that for methane. The self-diffusivity of CH_4 *increases* with q in the range 0–6 mol/kg, before reducing, inevitably to zero value as $q_{i,sat}$ is approached. The reason for the increase in $D_{i,self}$ is the reduction of the free energy barrier for inter-cage hopping of molecules with intra-cage loading, as has been explained in some detail by Beerdsen et al.[20-22]

For CO_2 the diffusivity remains practically independent of q in the range 0–4 mol/kg, before reducing to vanishing values at $q_{i,sat}$. Apparently, the influence of intra-cage loading of CO_2 does not lead to a reduction in the free energy barrier.

Comparing the pure component diffusivities to those in the mixture we observe that for a range of loadings up to 5 mol/kg there is no speeding-up of CH_4 or slowing-down of CO_2 in the mixture; the inter-cage hopping of molecules are practically independent of one another.

Figure 3.4 (left) presents the GCMC simulated isotherm data in DDR. Figure 3.4 (right) presents the MD simulation results for the self-diffusivities; the $D_{i,self}$ of both species tends to reduce to zero as $q_{i,sat}$ is approached. The loading dependence of the diffusivities of both species in DDR is analogous to that observed for CHA. Interestingly, there is approximately a 50-fold increase in $D_{i,self}$ of CH_4 as q is increased to 3 mol/kg.

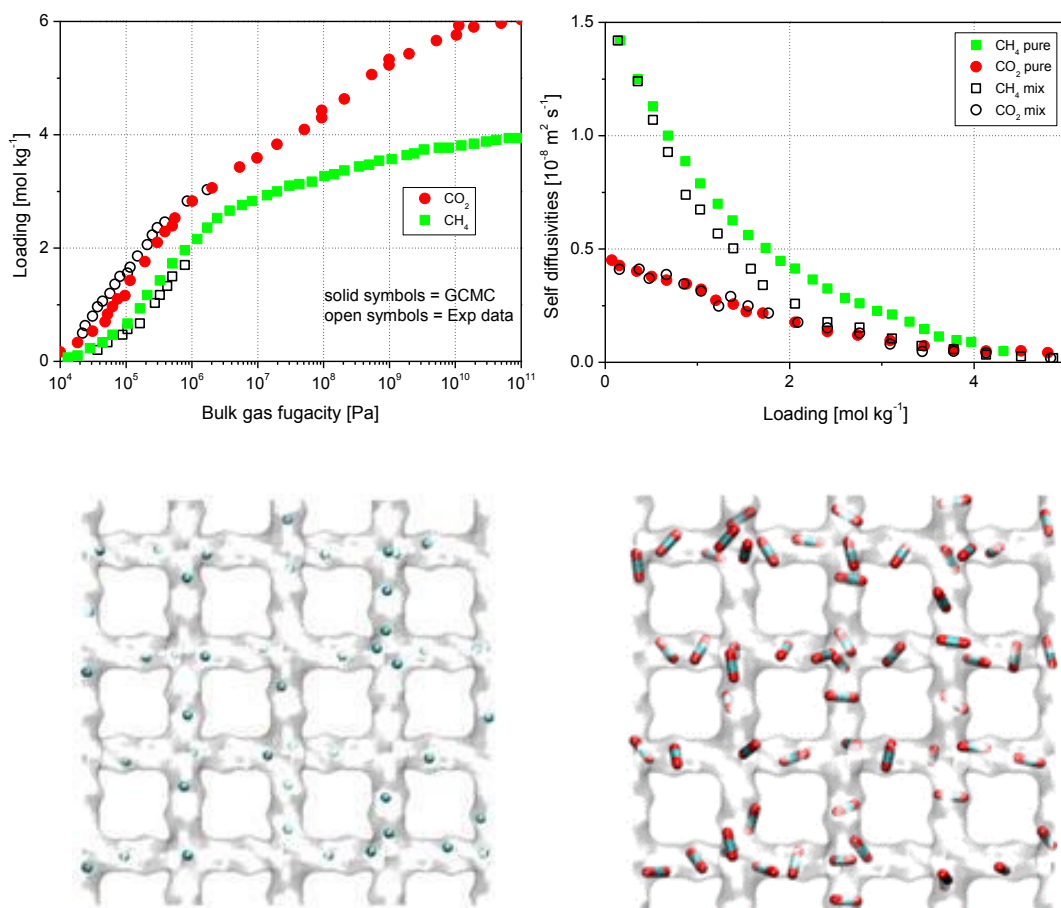


Figure 3.2 (Left) Sorption isotherm data for CH₄ and CO₂ in MFI at 300 K. The filled symbols are GCMC simulation results. The open symbols are experimental data of Zhu et al.[1] and Golden and Sircar[16]. (Right) MD simulations of self-diffusivities of CH₄ and CO₂ obtained for both pure components and in a 50–50 mixture plotted against the total molar loading, q . Snapshots showing the location of (left) CH₄ and (right) CO₂ molecules along the straight and zig-zag channels at 1000 Mpa.

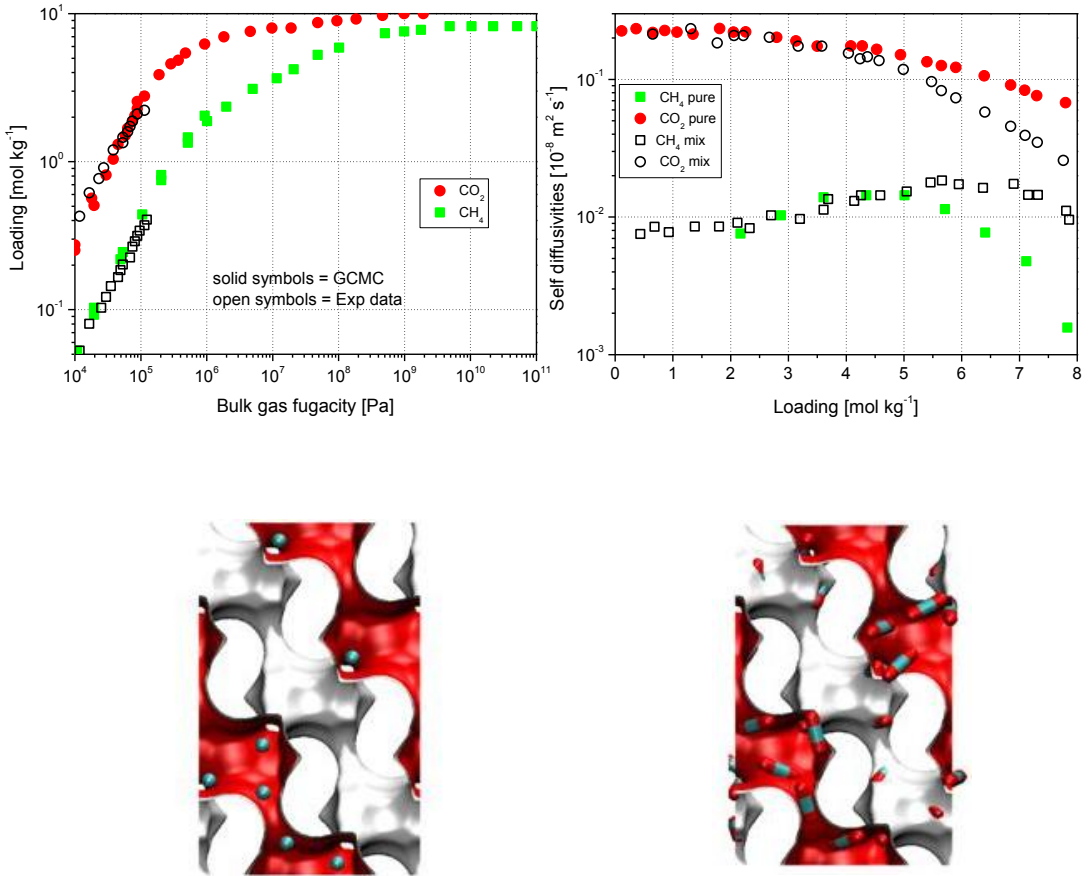


Figure 3.3 (Left) Sorption isotherm data for CH₄ and CO₂ in CHA at 300 K. The filled symbols are GCMC simulation results. The open symbols are experimental data of Li et al.[19] for SAPO-34, an isotype of CHA. (Right) MD simulations of self-diffusivities of CH₄ and CO₂, obtained for both pure components and in a 50–50 mixture plotted against the total molar loading. Snapshots showing the location of (left) CH₄ and (right) CO₂ molecules at 1000 Mpa.

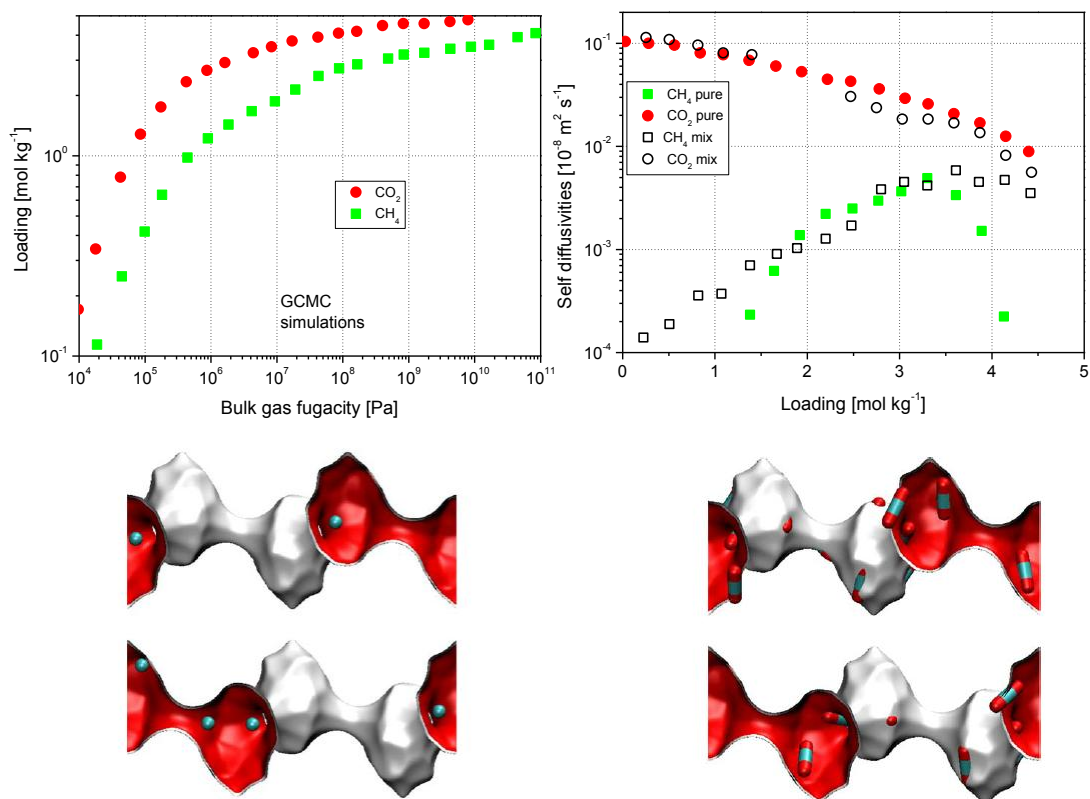


Figure 3.4 (Left) Sorption isotherm data for CH₄ and CO₂ in DDR at 300 K. (Right) MD simulations of self-diffusivities of CH₄ and CO₂ obtained for both pure components and in a 50–50 mixture plotted against the total molar loading. Snapshots showing the location of (left) CH₄ and (right) CO₂ molecules at 1000 Mpa.

The reduction in the free energy barrier for inter-cage hopping of CH₄ appears to be more strongly influenced by intra-cage loading in DDR than in CHA. One possible reason could be that the window size of DDR is 3.6 Å, slightly smaller than that in CHA. Up to a loading of 3.5 mol/kg the self-diffusivities of pure components are virtually the same as in the mixture and inter-cage hops are independent of one another. There is no speeding-up of CH₄ or slowing-down of CO₂ in the mixture. The narrow windows of DDR allow only one molecule to jump across cages at a time; see snapshots in Figure 3.4 (bottom).

Within the framework of the Maxwell-Stefan diffusion formulation for mixture diffusion in zeolites, the MD simulation results presented above indicate that the binary exchange coefficient D_{ij} can be taken to be infinitely large for CHA and DDR membranes, in

agreement with the conclusion reached by independent considerations and analysis of experimental data.

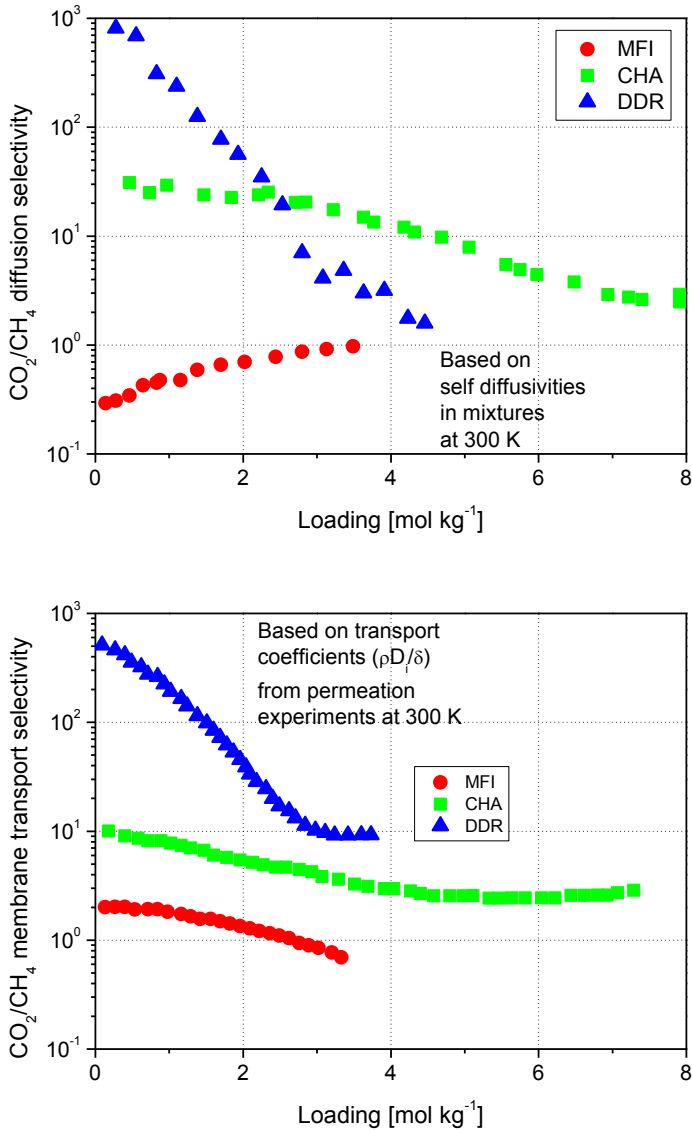


Figure 3.5 (Top) Diffusion selectivity, defined as the ratio of the self-diffusivity of CO_2 to that of CH_4 in a 50–50 mixture as a function of loading for MFI, CHA, and DDR zeolites. (Bottom) Membrane transport selectivity calculated from information in Krishna et al.[10]

The ratio of $D_{i,self}$ of CO_2 to that of CH_4 in the 50–50 mixture is plotted against the loading in Figure 3.5 (top). We see that diffusion selectivity is strongly dependent on both the loading and choice of zeolite; the variation is about five orders of magnitude. CHA and DDR zeolites are both promising candidates for separation, and are clearly superior to MFI. Experimental data on transport coefficients, $\rho D_i/\rho$, i.e. the diffusivity times the zeolite density divided by the membrane film thickness have been determined for MFI, CHA, and DDR membranes at 300 K by Krishna et al.[10] using published experimental data[1-3]; the ratio of these transport coefficients for CO_2 and CH_4 are plotted in Figure 3.5 (bottom). We note that the hierarchy of the diffusion selectivity values, as well as the dependence of the selectivity on the total loading is in broad agreement with those obtained from MD simulated self diffusivities.

3.4 Conclusions

In this Letter the self-diffusivities $D_{i,self}$ of CH_4 and CO_2 have been determined in three different zeolites, MFI, CHA, and DDR. The following conclusions can be drawn from the results presented in this Letter:

(1) In all three zeolites the $D_{i,self}$ of any species reduces to zero as the saturation loading $q_{i,sat}$ is approached.

(2) In the intersecting channel structures of MFI, CO_2 has a lower diffusivity than CH_4 possibly due to a higher molecular length. In CHA and DDR, that consist of cages separated by narrow windows, the more slender CO_2 has the higher diffusivity.

(3) In CHA and DDR there is a significant increase in $D_{i,self}$ of CH_4 for a range of loadings; this increase is due to the reduction in the free energy barrier for inter-cage hopping of molecules[22].

(4) In the intersecting channel structures of MFI correlation effects cause a significant slowing down of the faster diffusing species.

(5) For DDR, for loadings < 3.5 mol/kg the self-diffusivities in the mixture are virtually the same as for pure components indicating that the inter-cage hopping of molecules through the narrow windows separating the cages occur independently of one another. This conclusion is also true for CHA for a limited range of loadings < 5 mol/kg; beyond this loading the CO_2 appears to get slowed down by the presence of the CH_4 .

(6) On the basis of the results presented in Figure 3.5 we note that the highest diffusion selectivity for separation is offered by either CHA and DDR, depending on the loading.

Bibliography

- [1] Zhu, et al. *Industrial & Engineering Chemistry Research* **2006**, 45, 767.
- [2] Li, et al. *Industrial & Engineering Chemistry Research* **2005**, 44, 3220.
- [3] Tomita, et al. *Microporous and Mesoporous Materials* **2004**, 68, 71.
- [4] Baerlocher *Atlas of Zeolite Framework Types*; Elsevier: Amsterdam, 2002.
- [5] Calero, et al. *Journal of the American Chemical Society* **2004**, 126, 11377.
- [6] Ryckaert and Bellemans. *Faraday Discussions* **1978**, 95.
- [7] Dubbeldam, et al. *Journal of Physical Chemistry B* **2004**, 108, 12301.
- [8] Harris and Yung. *Journal of Physical Chemistry* **1995**, 99, 12021.
- [9] Makrodimitris, et al. *Journal of Physical Chemistry B* **2001**, 105, 777.
- [10] Krishna, et al. *Industrial & Engineering Chemistry Research* **2007**, 46, 2974.
- [11] Krishna and van Baten. *Journal of Physical Chemistry B* **2005**, 109, 6386.
- [12] Krishna and van Baten. *Chemical Physics Letters* **2005**, 407, 159.
- [13] Krishna and van Baten. *Chemical Physics Letters* **2006**, 420, 545.
- [14] Jobic, et al. *Journal of Physical Chemistry B* **2006**, 110, 2195.
- [15] van Baten and Krishna. *Microporous and Mesoporous Materials* **2005**, 84, 179.
- [16] Golden and Sircar. *Journal of Colloid and Interface Science* **1994**, 162, 182.
- [17] Kärger. Chapter 10: Diffusion in zeolites. In *Handbook of Zeolite Science and Technology* Auerbach, Ed.; Marcel Dekker: New York, 2003.
- [18] Skoulidas, et al. *Langmuir* **2003**, 19, 7977.
- [19] Li, et al. *Journal of Membrane Science* **2004**, 241, 121.
- [20] Beerdsen, et al. *Physical Review Letters* **2004**, 93.
- [21] Beerdsen, et al. *Physical Review Letters* **2005**, 95.
- [22] Beerdsen, et al. *Physical Review Letters* **2006**, 96.

We performed Configurational-bias Monte Carlo simulations to provide adsorption isotherms, Henry coefficients, and heats of adsorption of alkanes in sodium exchanged MFI- and MOR-type zeolites. We derived empirical expressions from the simulation data to describe the adsorption of linear alkanes in sodium exchanged MFI structures. These expressions adequately describe the Henry coefficient and adsorption enthalpy of *n*-alkanes as a function of sodium density and temperature. In the high coverage regime we provide an expression for saturation capacities of *n*-alkanes in the zeolite that combined with the obtained for Henry coefficients, gives a direct estimation of the complete adsorption isotherms of pure adsorbents and mixtures.



E. García-Pérez, I.M. Torréns, S. Lago, R. Krishna, B. Smit, and S. Calero

Molecular Simulation of Adsorption of *n*-Alkanes in Na-MFI Zeolites. Determination of Empirical Expressions

4.1 Introduction

Molecular simulations using classical potential models provide molecular level information inaccessible to experiment and beyond the reach of ab initio calculations. In particular, Configurational-bias Monte Carlo (CBMC) simulations are capable of accurately predicting adsorption of alkanes in zeolites[1-6] and molecular dynamics simulations using similar potentials can also predict diffusivities that closely match experiment[7]. MFI- and MOR-type topologies are among the most important synthetic zeolites from an industrial point of view[8-10]. MOR exists in a large Si/Al ratio domain and therefore it is particularly useful for catalytic applications. The structure with the highest Al-content has a composition $\text{Na}_8\text{Al}_8\text{Si}_{40}\text{O}_{96}$ and the structure can be refined with *Cmcm* symmetry[11]. The framework has a porous structure, which consists of main channels parallel to [001], having a slightly elliptical cross section with 12 TO_4 tetrahedron units ($\text{T} = \text{Si}, \text{Al}$), which are connected with small side channels parallel to [010], with 8 TO_4 cross sections called side-pockets.

The MFI-type zeolite can be synthesized with a composition range $8 \leq \text{Si}/\text{Al} \leq \infty$. It is a three-dimensional pore system consisting of straight, 0.53 nm across parallel channels

intersected by perpendicular zigzag channels and with 10-membered rings of oxygen atoms controlling the entrance to the channels[9]. At room temperature this zeolite typically has an orthorhombic symmetry (space group $Pnma$) with 12 distinct crystallographic T-sites[12]. In a previous work we presented a new force field able to reproduce accurately adsorption properties in sodium exchanged faujasites zeolites[13,14]. In this work we demonstrate that this force field can be successfully extended to other sodium exchanged zeolites. Firstly we have performed molecular simulations to provide adsorption properties of n -alkanes in several Na-MOR and Na-MFI structures varying the non-framework sodium concentration and secondly we have fitted the obtained results for Na-MFI structures with an empirical expression for Henry coefficients and heats of adsorption as a function of the sodium concentration, temperature, and type of alkane. Finally we have extended our calculations to mixtures of alkanes.

4.2 Methods

Simulations in the low and high coverage regime were computed using Configurational-bias Monte Carlo (CBMC) in the grand-canonical and NVT ensemble, respectively. The conventional simulation techniques to compute adsorption isotherms are prohibitively expensive for long alkanes whereas the CBMC technique simulates them at affordable cost[15]. In a CBMC simulation molecules are grown bead by bead biasing the growth process towards energetically favorable configurations avoiding overlap with the zeolite. During the growth the Rosenbluth factor is calculated. The average Rosenbluth factor is directly related to the free energy and the Henry coefficients[14,16]. More details on this simulation technique can be found elsewhere[16-18].

Zeolite frameworks have been constructed from silicon, aluminum, and oxygen atoms. The MFI-type zeolites were modeled from the crystallographic structure of silicalite[10] in which Si atoms were substituted by Al atoms[19,20]. The MOR models have been constructed from the crystallographic data of Meier[11]. In all cases simulation boxes were chosen large enough to obey the minimum image convention with a potential cut-off of 12 Å and periodic boundary conditions were applied in all directions. The charge distribution on the oxygen framework was considered static; i.e. polarization of oxygen by nearby sodium cations is implicitly modeled by distinguishing silicon from aluminum with a difference of $0.3 e^-$ between q_{Si} and q_{Al} [21]. Different charges are used for oxygen atoms bridging two silicon atoms, q_{OSi} , and oxygen atoms bridging one silicon and one aluminum atom q_{OAl} . q_{OSi} is obtained using the relation $q_{Si} + (2 \times q_{OSi}) = 0$, making the zeolite neutral in the absence of aluminum, while q_{OAl} is chosen to make the total system charge equal to zero[13,22,23].

The non-framework sodium cation density was adjusted to match the framework aluminum density and the density of the zeolites is determined by the framework atoms (aluminum, silicon, and oxygen) and the non-framework cations (sodium). In our model, the sodium cations can move freely (interactions defined through Lennard-Jones and Coulombic potentials) and adjust their position depending on their interactions with the framework atoms, other sodium cations, and alkane molecules.

The interactions between guest molecules (alkanes and sodium cations) with the zeolite host framework are modeled by Lennard-Jones and Coulombic potentials. The Coulomb interactions in the system are calculated using the Ewald summation[16]. The alkanes are described with a unit atom model, in which CH_x groups are considered as a single interaction centers with their own effective potentials[24]. The beads in the chain are connected by harmonic bonding potentials. The bond bending between three neighboring beads is modeled by a harmonic cosine bending potential and changes in the torsional angle are controlled by a Ryckaert-Bellemans potential. The beads in a chain separated by more than three bonds interact with each other through a Lennard-Jones potential. The interactions of the adsorbed molecules with the zeolite are dominated by the dispersive forces between the pseudo-atoms and the oxygen atoms of the zeolite[17,25,26] meaning that the silicon van der Waals interactions are taken into account through an effective potential with only the oxygen atoms. We use a newly developed force field, where the nature, density, and mobility of the non-framework cation, the density of the framework aluminum, and all host-guest interactions are carefully taking into account. The alkane-sodium, alkane-alkane, and alkane-zeolite interaction parameters were obtained by calibrating the force field through explicitly fitting a full isotherm over a wide range of pressures, temperatures, and sodium densities[13]. We fit complete adsorption isotherms, because experimental determination of the adsorption properties at very low and at very high coverage is fraught with difficulty resulting in a large spread in experimentally determined Henry coefficients and saturation loadings, respectively. The agreement between experimental data from different groups in the intermediate coverage regime is significantly better[13].

4.3 Results and discussion

Figure 4.1 (top) shows the excellent agreement of our computed isotherms for ethane in Na-MFI with available experimental data[27]. The isotherms reproduce the experimental isotherm shape and also the experimental saturation capacity of the validation data set. They were obtained for MFI structures with 3 Na⁺/uc at 295 and 297 K, respectively.

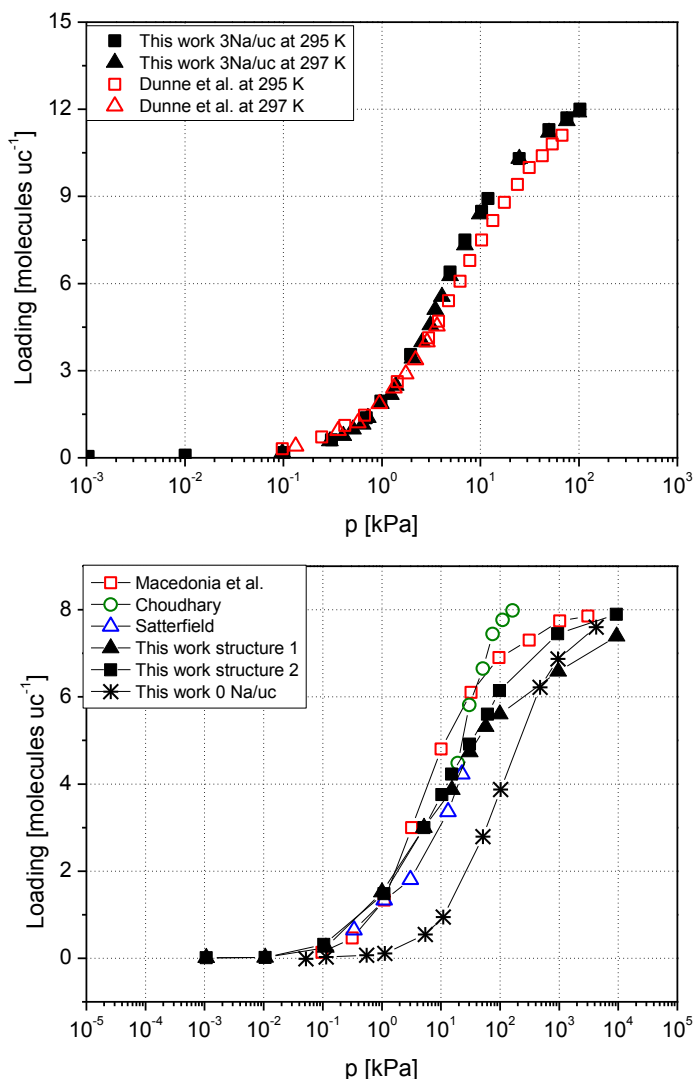


Figure 4.1 Simulated adsorption isotherms of ethane in sodium-exchanged zeolites. Available previous data are included for comparison[4,27-29]. (Top) Na-MFI structures with 3 Na⁺/uc at 295 and 297 K. (Bottom) Na-MOR structures with 8 Na⁺/uc at 296 K.

Henry coefficients and heats of adsorption of linear alkanes were computed for a wide range of temperatures and the full range of aluminum (and sodium) densities in both MOR and MFI-type zeolites. Table 4.1 summarizes the obtained values as a function of the sodium density for the MFI structure at 300 K.

Figure 4.1 (bottom) shows adsorption isotherms of ethane in sodium exchanged MOR structures (8 Na⁺/uc) at 296 K. Differences between previous experimental data are clearly observed [4,28,29]. Agreement between Maginn et al.[4] and Satterfield et al.[28] is good at low pressures but their isotherms diverge above 10 kPa.

Choudhary et al. show higher adsorption for their range of pressures leading to presume that small differences in sample preparation and aluminum distribution can play an important role on the adsorption in MOR topologies. Our simulations support this theory showing variation on the adsorption isotherms of ethane in Na-MOR structures with different Al distribution. Figure 4.1 (bottom) additionally compares the adsorption of ethane in both, pure silica and Na-exchanged structures. At 10 kPa the ethane loading is about one molecule per unit cell for the former, increasing up to four molecules per unit cell for the later. Our previous results showed similar behavior for Na-exchanged faujasites[6] and differences for MFI structures, though less significant, were also observed. This leads us to claim that non-framework sodium cations are vital to accurately obtain adsorption of alkanes in Na-exchanged zeolites.

As shown in Figure 4.2, Henry coefficients of linear alkanes in sodium exchanged MFI topologies adequately fit on a surface defined through the expression:

$$\ln K_H = (\eta \cdot N_s + \nu) \cdot CN - \xi \quad [4.1]$$

where η , ν , and ξ are given in Table 4.2 for a wide range of temperatures. This temperature dependence is captured by

$$z(T) = \frac{\left(\frac{x_1}{T} + x_2\right)}{T} + x_3 \quad , \quad z = \eta, \nu, \xi \quad [4.2]$$

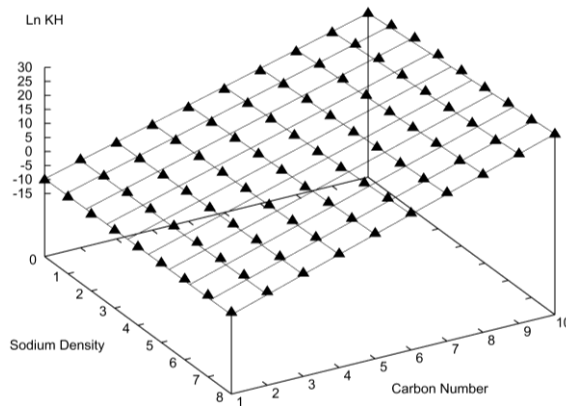


Figure 4.2 Henry coefficients of *n*-alkanes in Na-MFI obtained using CBMC simulations. Henry coefficients were computed at 300 K and they are plotted as a function of carbon number (methane to decane) and as a function of sodium density.

Table 4.1 Henry coefficients [$\text{mol kg}^{-1} \text{Pa}^{-1}$] at 300 K, and heats of adsorption [kJ mol^{-1}] in Na-MFI.

	2 Na/uc		4 Na/uc		6 Na/uc		8 Na/uc	
	$\text{Ln}K_{\text{H}}$	$-\Delta H^{\circ}$						
Methane	-11.8	18.6	-11.3	20.7	-10.7	22.6	-10.1	23.9
Ethane	-8.3	32.0	-8.0	32.9	-7.5	35.0	-7.2	36.1
Propane	-6.0	41.7	-5.5	43.2	-5.0	46.2	-4.6	47.2
Butane	-3.4	52.4	-2.8	55.0	-2.2	58.1	-1.8	59.3
Pentane	-0.8	62.4	-0.2	64.9	0.3	68.3	0.9	71.9
Hexane	2.0	73.4	2.5	74.9	3.1	79.6	4.0	84.4
Heptane	4.9	84.9	5.4	86.3	6.3	91.4	6.8	97.1
Octane	8.0	97.4	8.6	98.5	9.0	103.5	9.2	106.6
Nonane	11.1	110.0	11.7	110.7	12.1	116.0	12.0	119.2
Decane	14.4	122.2	15.0	122.9	15.1	128.2	15.1	131.9

Eqs. 4.1 and 4.2 can be combined into an empirical expression that describes the *n*-alkane Henry coefficient K_{H} [$\text{mol kg}^{-1} \text{Pa}^{-1}$] as a function of sodium density N_{s} [cations per unit cell], temperature T [K], and carbon number CN:

$$\begin{aligned}
LnK_H = & \frac{1}{T^2} [(4387.72N_s + 10570)CN - 11487.2] \\
& + \frac{1}{T} [(5N_s + 1166.4)CN + 1221.89] - (0.016N_s + 1.409)CN \\
& - 17.9
\end{aligned} \quad [4.3]$$

The temperature derivative of Eq. 4.3 provides an expression for the adsorption enthalpy ΔH_0 [kJ mol⁻¹]:

$$\begin{aligned}
-\Delta H_0 = & \frac{2}{T} [(4387.72N_s + 10570)CN - 11487.2] + (5N_s + 1166.4)CN \\
& + 1221.89
\end{aligned} \quad [4.4]$$

Table 4.2 Coefficients η , ν , and ξ as a function of temperature

T [K]	250	300	350	400	450	500
η	0.074	0.048	0.035	0.024	0.017	0.011
ν	342.42	26008	200.81	157.08	123.35	0.97
ξ	130.2	139.6	145.25	149.24	152.52	155.19

Figure 4.3 compares the heats of adsorption of n -alkanes obtained from the empirical expression with available experimental data[30-34]. The applicability of the new force field is by no means limited to low pressure for it also reproduces accurately the adsorption of alkanes at high pressures[13]. The saturation capacities (θ_{sat}) of n -alkanes (methane to hexadecane) for Na-exchanged MFI topologies can be fit to a second order exponential decay as a function of the carbon number (CN):

$$\theta_{sat} [\text{molecules/uc}] = 1.1 + 21.5 \exp - \left[\frac{CN}{2.7} \right] + 6.9 \exp - \left[\frac{CN}{13} \right] \quad [4.5]$$

$$\theta_{sat} [\text{molecules/uc}] = \theta_{sat} [\text{mol} \cdot \text{kg}^{-1}] \cdot N_{AV} \cdot \rho [\text{kg} \cdot \text{m}^{-3}] \cdot V [\text{m}^3] \quad [4.6]$$

where N_{AV} is Avogadro's number, ρ the zeolite density, and V is the volume of the unit cell.

The saturation capacity [mol kg⁻¹] combined with the expression for the Henry coefficients (Eq. 4.3) allow the direct estimation of the adsorption isotherms of linear alkanes in sodium MFI structures by using the Langmuir isotherm in the form:

$$\theta = \frac{K_H kp}{1 + (K_H/\theta_{sat})p} \quad [4.7]$$

where θ is the loading of alkane in the zeolite in mol per kilogram and p is the system pressure in Pa. Calculations using Eq. 4.7 are in good agreement with the adsorption isotherms of adsorbents obtained from CBMC in silicalite and sodium exchanged structures. This can be observed in Figure 4.4 for the adsorption of pure component methane, ethane, propane, and *n*-butane and the equimolar quaternary mixture in MFI at 300 K.

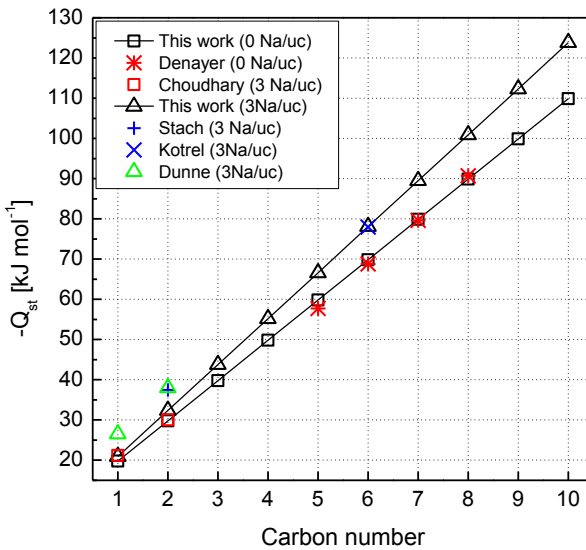


Figure 4.3 Heats of adsorption of linear alkanes in Na-MFI zeolites obtained from our empirical expression. In all cases deviation between empirical (Eq. 4.4) and computed results is smaller than the symbol size. Available experimental sets are included for comparison[30-34].

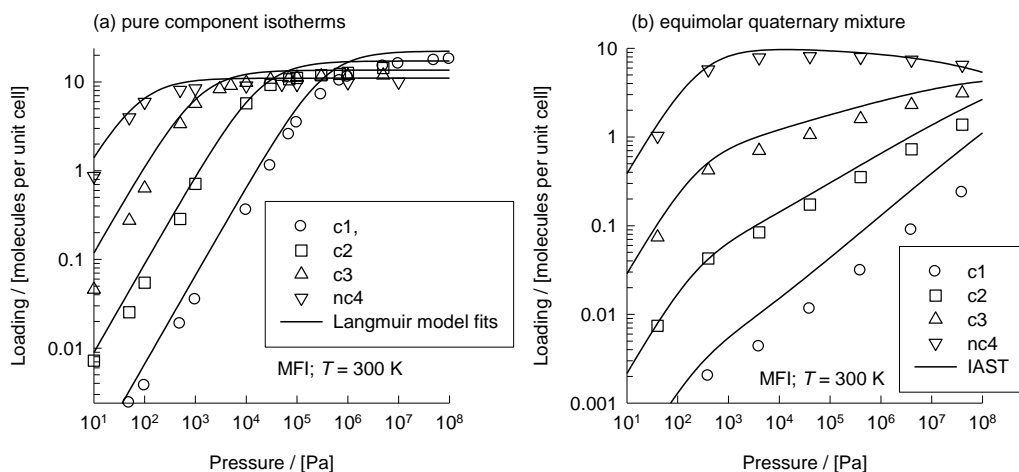


Figure 4.4 Adsorption isotherms of *n*-alkanes in MFI using 1) CBMC simulation (symbols) and 2) a Langmuir model in which the parameters are calculated from Eqs. 4.3 and 4.5 (line). (Left) Pure components. (Right) Equimolar mixture of methane, ethane, propane, and *n*-butane.

4. 4 Conclusions

Our recently developed united atom force field for alkanes in sodium faujasites has been successfully applied to a variety of MOR and MFI sodium exchanged topologies. In the low coverage regime we provide simple expressions that adequately describe the *n*-alkane Henry coefficient and adsorption enthalpy in Na-MFI topologies as a function of sodium density and temperature. The predicted Henry coefficients and heats of adsorption compare extremely well to available experimental data affording an adequate substitute for complex Configurational-bias Monte Carlo simulations. In the high coverage regime we provide an expression for saturation capacities of linear alkanes in sodium exchanged MFI. This expression combined with the expression for the Henry coefficients gives a direct estimation of adsorption isotherms of pure adsorbents and mixtures, in good agreement with the adsorption isotherms obtained from CBMC.

Bibliography

- [1] Lachet, et al. *Faraday Discussions* **1997**, 307.
- [2] Krishna, et al. *J. Phys. Chem. A* **1998**, 102, 7727.

- [3] Mellot, et al. *J. Am. Chem. Soc.* **1998**, 120, 5788.
- [4] Macedonia, et al. *Langmuir* **2000**, 16, 3823.
- [5] Calero, et al. *Phys. Chem. Chem. Phys.* **2001**, 3, 4390.
- [6] Krishna, et al. *Chemical Society Reviews* **2002**, 31, 185.
- [7] Auerbach, et al. *Diffusion in Zeolites*; Marcel Dekker Inc.: New York, 2003.
- [8] Olson, et al. *Journal of Physical Chemistry* **1981**, 85, 2238.
- [9] Flanigen, et al. *Nature* **1978**, 271, 512.
- [10] van Koningsveld, et al. *Acta Crystallographica Section B* **1987**, 43, 127.
- [11] Meier. *Kristallogr.* **1961**, 115, 439.
- [12] Baerlocher *Atlas of Zeolite Structure Types*, 5th ed.; Elsevier: London, 2001.
- [13] Calero, et al. *Journal of the American Chemical Society* **2004**, 126, 11377.
- [14] Dubbeldam, et al. *Physical Review Letters* **2003**, 90, 245901.
- [15] Smit and Maesen. *Nature* **1995**, 374, 42.
- [16] Frenkel and Smit *Understanding Molecular Simulations: From Algorithms to Applications*, second edition ed.; Academic Press: San Diego, CA, 2002.
- [17] Vlugt, et al. *J. Phys. Chem. B* **1999**, 103, 1102.
- [18] Smit and Siepmann. *Journal of Physical Chemistry* **1994**, 98, 8442.
- [19] Stave and Nicholas. *J. Phys. Chem. -US* **1995**, 99, 15046.
- [20] Alvarado-Swaisgood, et al. *J. Phys. Chem.* **1991**, 95, 10031.
- [21] Jaramillo and Auerbach. *Journal of Physical Chemistry B* **1999**, 103, 9589.
- [22] Beerdsen, et al. *J. Phys. Chem. B* **2002**, 106, 10659.
- [23] Beerdsen, et al. *Journal of Physical Chemistry B* **2003**, 107, 12088.
- [24] Ryckaert and Bellemans. *Faraday Discussions* **1978**, 95.
- [25] Bezus, et al. *Journal of the Chemical Society-Faraday Transactions II* **1978**, 74, 367.
- [26] Kiselev, et al. *Zeolites* **1985**, 5, 261.
- [27] Dunne, et al. *Langmuir* **1996**, 12, 5896.
- [28] Satterfield and Frabetti. *Aiche Journal* **1967**, 13, 731.
- [29] Choudhary, et al. *Journal of the Chemical Society-Faraday Transactions* **1995**, 91, 2935.
- [30] Dunne, et al. *Langmuir* **1997**, 13, 4333.
- [31] Stach, et al. *Pure and Applied Chemistry* **1993**, 65, 2193.
- [32] Kotrel, et al. *Journal of Physical Chemistry B* **1999**, 103, 818.
- [33] Denayer, et al. *J. Phys. Chem. B* **1998**, 102, 4588.
- [34] Choudhary and Mayadevi. *Separation Science and Technology* **1993**, 28, 2197.

Configurational-bias Monte Carlo (CBMC) simulations provide adsorption isotherms, Henry coefficients, and heats of adsorption of linear alkanes in sodium-exchanged MFI- and FAU-type zeolites. These simulations were carried out using our newly developed force field that reproduces experimental sodium positions in the dehydrated zeolites, and successfully predicts alkane adsorption properties over a wide range of sodium cation densities, temperatures, and pressures. We derived empirical expressions from the simulation data to describe the adsorption of linear alkanes in MFI- and FAU-type zeolites. These expressions afford a suitable substitute for complex CBMC simulations. In the low coverage regime we provide simple expressions that adequately describe the Henry coefficient and adsorption enthalpy of *n*-alkanes as a function of sodium density and temperature. The predicted Henry coefficients and heats of adsorption compare extremely well to available experimental data. In the high coverage regime we provide an expression for saturation capacities of linear alkanes in the zeolite. This expression, combined with the expression for the Henry coefficients, provides of the complete adsorption isotherms of pure adsorbents and mixtures, in good agreement with the adsorption isotherms obtained from CBMC.



E. García-Pérez, I.M. Torréns, S. Lago, D. Dubbeldam, T.J.H. Vlugt, T.L.M. Maesen, B. Smit, R. Krishna, and S. Calero

Elucidating Alkane Adsorption in Sodium-Exchanged Zeolites from Molecular Simulations to Empirical Equations

5.1 Introduction

Zeolites are microporous materials with widespread use in several areas of technology. They yield efficient heterogeneous catalysts, adsorbents, and gas separators[1-4]. Molecular simulations are a powerful tool for gaining insight into the physics underlying the widespread use of zeolites in these industrial processes at a molecular level. In particular, Configurational-bias Monte Carlo (CBMC) simulations are capable of accurately predicting adsorption isotherms of linear and branched alkanes[5-9] and their mixtures[10,11] in zeolites.

Among the numerous synthetic zeolites known to date, zeolites with FAU and MFI topologies are the most widely studied and the most commercially important[12-18]. The FAU-type zeolite topology consists of small (sodalite) cages arranged so as to form 1.2 nm wide supercages accessible through 0.72 nm wide windows. The composition of the unit cell is $\text{Na}_x\text{Al}_x\text{Si}_{192-x}\text{O}_{384}$, where $96 \geq x \geq 0$. FAU-type zeolites are called either *X* and *Y*—depending on their framework aluminum density (x). *X* has a framework aluminum density between 96 and 77 aluminum atoms per unit cell, whereas *Y* contains fewer than 77 framework aluminum atoms per unit cell. The MFI-type zeolite can be synthesized with a composition range $8 \leq \text{Si}/\text{Al} \leq \infty$. It is a three-dimensional pore system consisting of straight, 0.53 nm across parallel channels intersected by perpendicular zigzag channels. At room temperature the composition of the unit cell is $\text{Na}_x\text{Al}_x\text{Si}_{96-x}\text{O}_{192}$, where $27 \geq x \geq 0$ [19]. MFI-type zeolites are called either ZSM-5 or silicalite depending on the framework aluminum density (x). The name silicalite is used for zeolites with a very low x value.

The remainder of the paper is organized as follows: in Section 2 we present our simulation methods. We continue in Section 3 with the results of our simulations. These include adsorption isotherms, Henry coefficients, and heats of adsorption of linear alkanes in several MFI and FAU structures varying the non-framework sodium concentration. We fit the results with an empirical expression for Henry coefficients and heats of adsorption as a function of the sodium concentration, temperature, and linear alkane, and we extend our calculations to mixtures of alkanes at high pressure. Finally, we give some concluding remarks in Section 4.

5.2 Methodology

Simulations in the low and high coverage regime were computed using Configurational-bias Monte Carlo simulation in the grand-canonical ensemble (constant chemical potential, constant volume V , and constant temperature T) and NVT ensemble (constant number of particles N , constant volume V , and constant temperature T), respectively. The conventional simulation techniques to compute adsorption isotherms are prohibitively expensive for long alkanes whereas the CBMC technique simulates them at affordable cost[20]. In a CBMC simulation molecules are grown bead by bead biasing the growth process towards energetically favorable configurations avoiding overlap with the zeolite. During the growth the Rosenbluth factor is calculated. The average Rosenbluth factor is directly related to the free energy and the Henry coefficient[21,22]. More details on this simulation technique can be found elsewhere[21,23,24].

Zeolite frameworks have been constructed from silicon, aluminum, and oxygen atoms. FAU-type zeolites were modeled utilizing the crystallographic atom positions in

dehydrated Na-X[25]. The structures with lower framework aluminum densities were obtained by randomly substituting aluminum by silicon. This procedure automatically satisfies the Löwenstein rule and it should afford a reasonable approximation of the framework aluminum distributions obtained by experimental methods[26-29]. The MFI-type zeolites were modeled from the crystallographic structure of silicalite of van Koningsveld et al.[30] in which Si atoms were substituted by Al atoms at the preferred positions as indicated by Stave and Nicholas[31] and Alvarado-Swaisgood et al.[32] In all cases the simulation boxes were chosen large enough to obey the minimum image convention with a potential cutoff of 12 Å and periodic boundary conditions were applied in all directions. The charge distribution on the oxygen framework was considered static, i.e. polarization of oxygen by nearby sodium cations is implicitly modeled by distinguishing silicon from aluminum with a difference of $0.3 e^-$ between q_{Si} and q_{Al} [33]. Different charges are used for oxygen atoms bridging two silicon atoms, q_{OSi} , and oxygen atoms bridging one silicon and one aluminum atom q_{OAl} . q_{OSi} is obtained using the relation $q_{\text{Si}} + (2 \times q_{\text{OSi}}) = 0$, making the zeolite neutral in the absence of aluminum, while q_{OAl} is chosen to make the total system charge equal to zero[34-36].

The non-framework sodium cation density was adjusted to match the framework aluminum density and the density of the zeolites is determined by the framework atoms (aluminum, silicon, and oxygen) and the non-framework cations (sodium). In our model, the sodium cations can move freely and adjust their position depending on their interactions with the framework atoms, other sodium cations, and alkane molecules.

The interactions between guest molecules (alkanes and sodium cations) with the zeolite host framework are modeled by Lennard-Jones and Coulombic potentials. The Coulomb interactions in the system are calculated using the Ewald summation[21]. The alkanes are described with a united atom model, in which CH_x groups are considered as a single interaction centers with their own effective potentials[37]. The beads in the chain are connected by harmonic bonding potentials. The bond bending between three neighboring beads is modeled by a harmonic cosine bending potential and changes in the torsional angle are controlled by a Ryckaert-Bellemans potential. The beads in a chain separated by more than three bonds interact with each other through a Lennard-Jones potential. The interactions of the adsorbed molecules with the zeolite are dominated by the dispersive forces between the pseudo-atoms and the oxygen atoms of the zeolite[23,38,39] meaning that the silicon van der Waals interactions are taken into account through an effective potential with only the oxygen atoms. We use a newly developed force field, where the

nature, density, and mobility of the non-framework cation, the density of the framework aluminum, and all host–guest interactions are carefully taking into account. The alkane–sodium, alkane–alkane, and alkane–zeolite interaction parameters were obtained by calibrating the force field through explicitly fitting a full isotherm over a wide range of pressures, temperatures, and sodium densities[36]. We fit complete adsorption isotherms, because experimental determination of the adsorption properties at very low and at very high coverage is fraught with difficulty resulting in a large spread in experimentally determined Henry coefficients and saturation loadings, respectively. The agreement between experimental data from different groups in the intermediate coverage regime is significantly better[36].

5.3 Results and discussion

In our previous work, we presented a new force field able to reproduce accurately all adsorption properties in sodium-exchanged faujasite zeolites[36]. The following results demonstrate that this force field can be successfully extended to sodium-exchanged MFI-type zeolites. Figure 5.1 shows the excellent agreement of our computed isotherms for ethane with available experimental data[40]. The number of sodium cations and the temperature used for each isotherm were chosen to facilitate comparison with these experimental data. Hence, the ethane isotherms in Figure 5.1 were obtained for MFI structures with 3 Na⁺/uc at 295 and 297 K, respectively. It is important to note (1) that the data obtained for MFI structures were not part of the calibration of validation data and (2) that our computed isotherms reproduce the experimental isotherm shape and also the experimental saturation capacity of the validation data set.

Henry coefficients and heats of adsorption of linear alkanes were computed for a wide range of temperatures and the full range of aluminum (and sodium) densities in both FAU- and MFI-type zeolites. Figures 5.2 (left) and 5.2 (right) show the obtained Henry coefficients as a function of the sodium density for the faujasite (500 K) and MFI (300 K) structures, respectively.

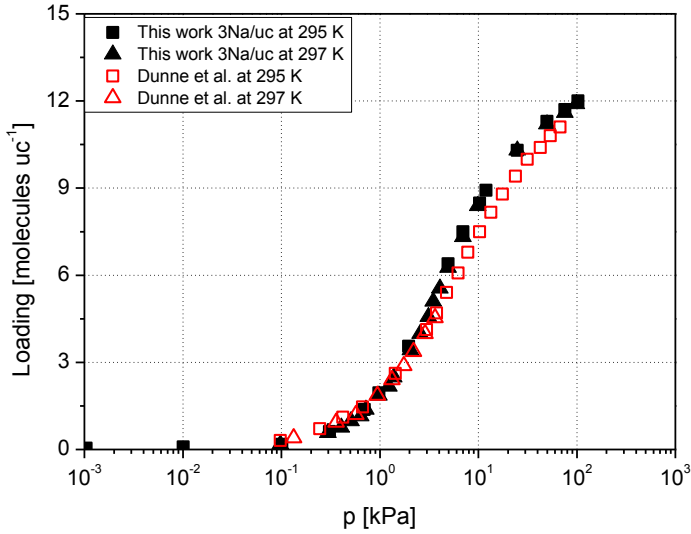


Figure 5.1 Adsorption isotherms of ethane in sodium-exchanged MFI obtained from our CBMC simulation. Experimental isotherms are included for comparison[40].

These values adequately fit on a surface defined through the expression:

$$\ln K_H = (\eta N_s + \nu)CN - \xi \quad [5.1]$$

where η , ν , and ξ are given in Table 5.1 for a wide range of temperatures. This temperature dependence is captured by a relationship with three sets of x_1 (K^2), x_2 (K), and x_3 defining the value of η , ν , and ξ as a function of temperature.

$$z(T) = \frac{((x_1/T) + x_2)}{T} + x_3, \quad z = \eta, \nu, \xi \quad [5.2]$$

Finally, Eqs. [5.1] and [5.2] can be combined into an empirical expression that describes the n -alkane Henry coefficient K_H [$\text{mol kg}^{-1} \text{Pa}^{-1}$] as a function of sodium density N_s (cations per unit cell), the temperature T [K], and the carbon number CN :

$$\ln K_H = \frac{1}{T^2} [(a_1 N_s + b_1)CN + c_1] + \frac{1}{T} [(a_2 N_s + b_2)CN + c_2] + (a_3 N_s + b_3)CN + c_3 \quad [5.3]$$

where a_i , b_i , and c_i , are listed in Table 5.2 for both, FAU and MFI topologies. The temperature derivative of this equation provides an expression for the adsorption enthalpy ΔH_0 [kJ mol⁻¹]:

$$-\Delta H_0 = \frac{2}{T} [(a_1 N_s + b_1)CN + c_1] + (a_2 N_s + b_2)CN + c_2 \quad [5.4]$$

Table 5.1 Coefficients η , ν , and ξ as a function of temperature T .

T (K)	η	ν	ξ
Na-FAU			
298	0.014957	1.39119	14.4646
350	0.012264	1.08779	14.866
400	0.010578	0.876027	15.1529
450	0.009006	0.73277	15.4171
500	0.007988	0.605648	15.6199
550	0.00708	0.504509	15.7754
600	0.006323	0.42539	15.9129
650	0.005722	0.358542	16.0439
Na-MFI			
250	0.074	342.42	130.20
300	0.048	260.08	139.60
350	0.035	200.81	145.25
400	0.024	157.08	149.24
450	0.017	123.35	152.52
500	0.011	0.97	155.19

The values were obtained by fitting the Henry coefficients obtained for linear alkanes in sodium-exchanged MFI- and FAU- type zeolites to the surfaces reproduced by Eq. [5.1]

Table 5.2 Coefficients used in Eqs. [5.3-5.5] for sodium-exchanged MFI- and FAU- type zeolites.

	a_1	a_2	a_3		
MFI	4387.72	5	-0.016		
FAU	144.1	4.37	-0.00135		
	b_1	b_2	b_3		
MFI	10570	1166.4	-1.409		
FAU	27438.4	432.8	-0.3716		
	c_1	c_2	c_3		
MFI	-11487.2	1221.89	-17.9		
FAU	-49567.3	1111.13	-17.634		
	D_1	D_2	D_3	E_1	E_2
MFI	1.1	21.5	6.9	2.7	13
FAU	2.6	144.9	50.6	1.7	9.3

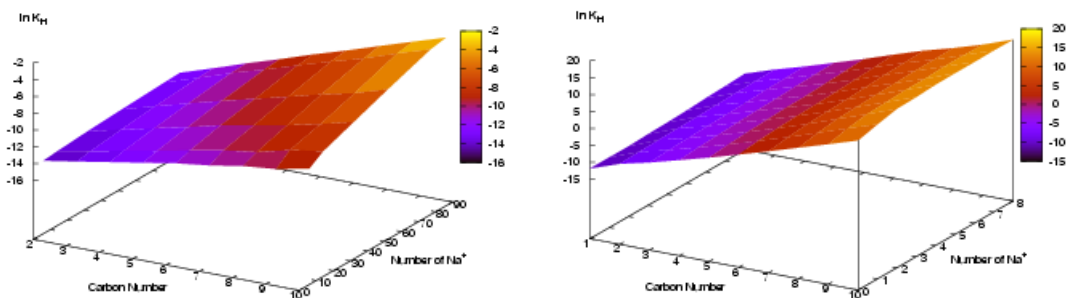


Figure 5.2 The Henry coefficients of n -alkanes as a function of the number of sodium cations fit nicely to a surface: (Left) Na-FAU at 500 K; (Right) Na-MFI at 300 K.

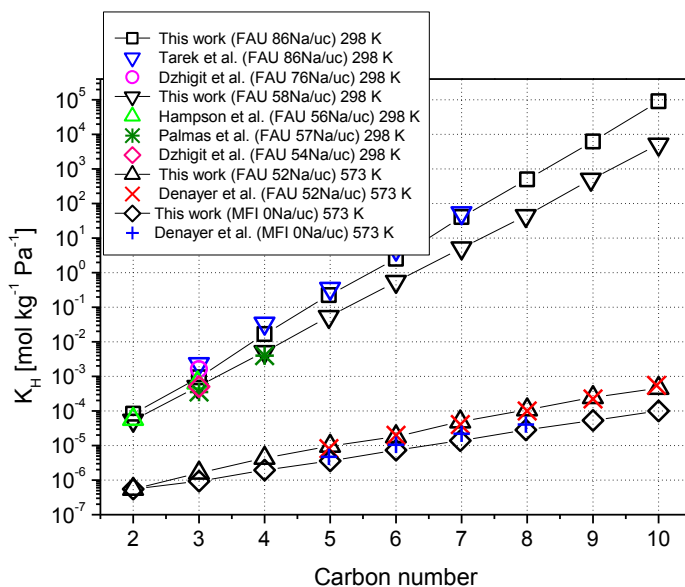


Figure 5.3 Henry coefficients of linear alkanes in sodium faujasites and MFI at several temperatures obtained from our empirical expression. In all cases deviation between our empirical Eq. [5.3] and computed results is smaller than the symbol size. Available experimental and simulation sets are included for comparison [41-46].

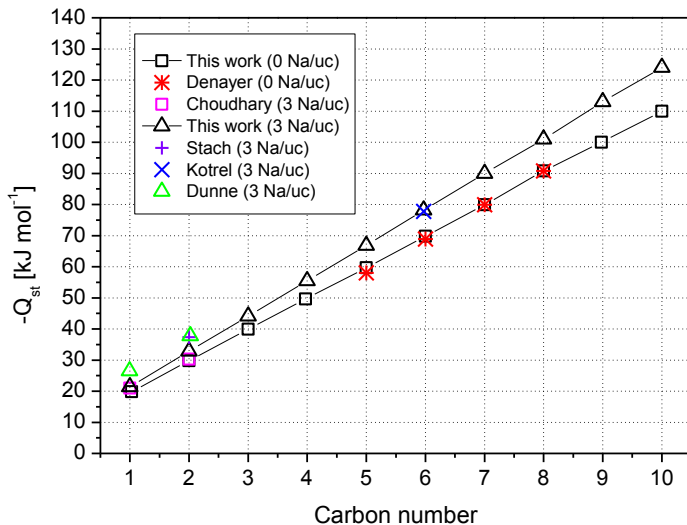


Figure 5.4 Heats of adsorption of linear alkanes in Na-MFI zeolites obtained from our empirical expression. In all cases deviation between our empirical Eq. [5.4] and the computed results is smaller than the symbol size. Available experimental and simulation sets are included for comparison[47-51].

Note that these expressions can be applied independently of the zeolite topology. Figure 5.3 compares the Henry coefficients obtained for n -alkanes from this empirical expression with available experimental data in both topologies[41-46]. The calculated heats of adsorption of methane to decane in sodium-exchanged MFI structures are given in Figure 5.4. A comparison with available experimental data is included[47-51].

As reported in our previous work[36], the applicability of the new force field is by no means limited to low pressure for it also reproduces accurately the adsorption of alkanes at high pressures. The saturation capacities of n -alkanes (methane to hexadecane) were computed for several Na-exchanged MFI. From our simulations we can conclude that (1) saturation capacities θ_{sat} (molecules per unit cell) are roughly independent on the amount of sodium non-framework cations and (2) saturation capacities can be fit to a second order exponential decay as a function of the carbon number (CN) for *both* FAU and MFI topologies:

$$\theta_{\text{sat}}(\text{molec/uc}) = D_1 + D_2 \exp - \left[\frac{CN}{E_1} \right] + D_3 \exp - \left[\frac{CN}{E_2} \right] \quad [5.5]$$

$$\theta_{\text{sat}}(\text{molec/uc}) = \theta_{\text{sat}}(\text{mol kg}^{-1}) N_{\text{AV}} \rho(\text{kg m}^{-3}) V(\text{m}^3) \quad [5.6]$$

where N_{AV} is Avogadro's number, ρ the zeolite density, V is the volume of the unit cell, and D_i and E_i are listed in Table 5.2. The saturation capacity (mol kg^{-1}) combined with the expression for the Henry coefficients Eq. [5.3] allow the direct estimation of the adsorption isotherms of linear alkanes in these zeolites. The above correlations for the Henry coefficient and the saturation capacity can be used to obtain a rough estimate of the complete adsorption isotherm, by using the Langmuir isotherm. This can be observed in Figure 5.5 for the adsorption of pure component C_1 , C_2 , C_3 , and $n\text{-}C_4$ and the equimolar quaternary mixture in MFI at 300 K.

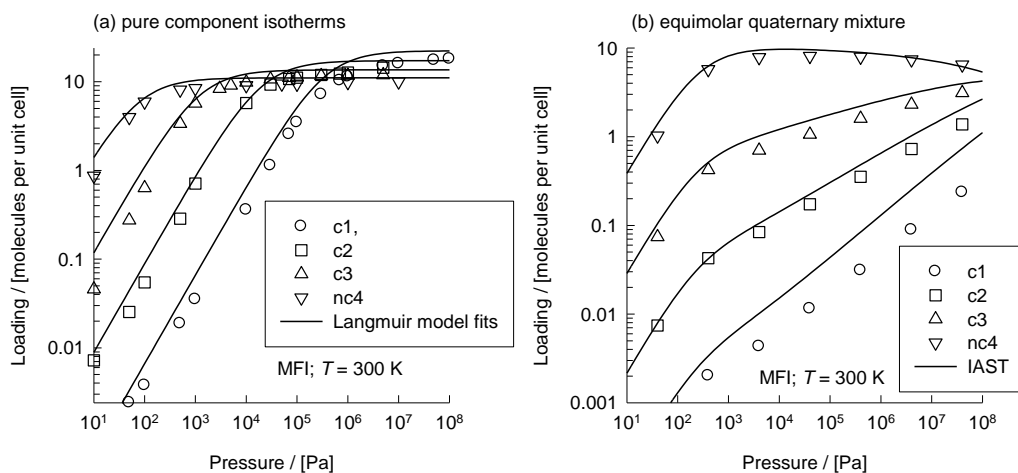


Figure 5.5 Adsorption isotherms of n -alkanes in MFI using 1) CBMC simulation (symbols) and 2) a Langmuir model in which the parameters are calculated from Eqs. [5.3] and [5.5] (line) using the Ideal Adsorbed Solution Theory (IAST). (Left) Pure components. (Right) Equimolar mixture of methane, ethane, propane and n -butane.

5.4. Conclusions

In this work, we have performed molecular simulations to determine adsorption isotherms, Henry coefficients, and heats of adsorption of linear alkanes (C_1 – C_{10}) in zeolites containing non-framework sodium cations and framework aluminum atoms. Our simulations reproduce accurately the available experimental adsorption data in sodium-exchanged MFI- and FAU-type zeolites over a wide range of cation densities, temperatures, and pressures. Firstly, our simulations predict adsorption properties in the low-pressure regime and from the resulting simulation data we have obtained a simple empirical expression that describes the n -alkane Henry coefficient and adsorption

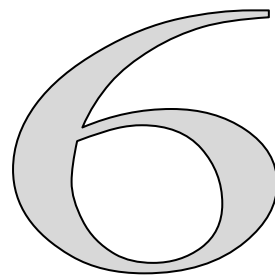
enthalpy as a function of sodium density and temperature at low coverage, affording an adequate substitute for complex Configurational-bias Monte Carlo simulations. Application of our newly developed force field is by no means limited to FAU topologies, as it successfully reproduces the adsorption properties of alkanes in sodium-exchanged MFI structures.

Bibliography

- [1] Zecchina and Otero Areán. *Chem. Soc. Rev.* **1996**, 25, 187.
- [2] van Santen and Kramer. *Chem. Rev.* **1995**, 95, 637.
- [3] Schenk, et al. *Angewandte Chemie-International Edition* **2002**, 41, 2500.
- [4] Schenk, et al. *Angewandte Chemie-International Edition* **2001**, 40, 736.
- [5] Lachet, et al. *Faraday Discussions* **1997**, 307.
- [6] Krishna, et al. *J. Phys. Chem. A* **1998**, 102, 7727.
- [7] Mellot, et al. *J. Am. Chem. Soc.* **1998**, 120, 5788.
- [8] Macedonia, et al. *Langmuir* **2000**, 16, 3823.
- [9] Schenk, et al. *Langmuir* **2001**, 17, 1558.
- [10] Calero, et al. *Journal of Catalysis* **2001**, 202, 395.
- [11] Calero, et al. *Phys. Chem. Chem. Phys.* **2001**, 3, 4390.
- [12] Hattori. *Chemical Reviews* **1995**, 95, 537.
- [13] Satterfield and Cheng. *Aiche Journal* **1972**, 18, 720.
- [14] Breck *Zeolite Molecular Sieves*; Wiley: New York, 1974.
- [15] Denayer, et al. *Journal of Catalysis* **2003**, 220, 66.
- [16] Flanigen, et al. *Nature* **1978**, 271, 512.
- [17] Olson, et al. *Journal of Physical Chemistry* **1981**, 85, 2238.
- [18] van Bekkum, et al. *Studies in Surface Science and Catalysis*; Elsevier Science B. V: Amsterdam, 1991; Vol. 58.
- [19] Baerlocher *Atlas of Zeolite Structure Types*, 5th ed.; Elsevier: London, 2001.
- [20] Smit and Maesen. *Nature* **1995**, 374, 42.
- [21] Frenkel and Smit *Understanding Molecular Simulations: From Algorithms to Applications*, second edition ed.; Academic Press: San Diego, CA, 2002.
- [22] Dubbeldam, et al. *Physical Review Letters* **2003**, 90, 245901.
- [23] Vlugt, et al. *J. Phys. Chem. B* **1999**, 103, 1102.
- [24] Smit and Siepmann. *Journal of Physical Chemistry* **1994**, 98, 8442.
- [25] Olson. *Zeolites* **1995**, 15, 439.
- [26] Melchior, et al. *Journal of the American Chemical Society* **1982**, 104, 4859.
- [27] Herrero. *Journal of the Chemical Society, Faraday Transactions* **1991**, 87, 2837.
- [28] Muller, et al. *Journal of Physical Chemistry* **1996**, 100, 1189.
- [29] Peterson. *Journal of Physical Chemistry B* **1999**, 103, 3145.

- [30] van Koningsveld, et al. *Acta Crystallographica Section B* **1987**, 43, 127.
- [31] Stave and Nicholas. *J. Phys. Chem. -US* **1995**, 99, 15046.
- [32] Alvarado-Swaisgood, et al. *J. Phys. Chem.* **1991**, 95, 10031.
- [33] Jaramillo and Auerbach. *Journal of Physical Chemistry B* **1999**, 103, 9589.
- [34] Beerdsen, et al. *J. Phys. Chem. B* **2002**, 106, 10659.
- [35] Beerdsen, et al. *Journal of Physical Chemistry B* **2003**, 107, 12088.
- [36] Calero, et al. *Journal of the American Chemical Society* **2004**, 126, 11377.
- [37] Ryckaert and Bellemans. *Faraday Discussions* **1978**, 95.
- [38] Bezus, et al. *Journal of the Chemical Society-Faraday Transactions II* **1978**, 74, 367.
- [39] Kiselev, et al. *Zeolites* **1985**, 5, 261.
- [40] Dunne, et al. *Langmuir* **1996**, 12, 5896.
- [41] Denayer and Baron. *Adsorption-Journal of the International Adsorption Society* **1997**, 3, 251.
- [42] Tarek, et al. *Zeolites* **1995**, 15, 67.
- [43] Palmas, et al. *Journal of Chemical and Engineering Data* **1991**, 36, 1.
- [44] Hampson and Pees. Adsorption of Lower Hydrocarbons in Zeolite Nay and Theta-1 - Comparison of Low and High-Pressure Isotherm Data. In *Zeolites and Microporous Crystals*, 1994; Vol. 83; pp 197.
- [45] Dzhigit, et al. *Zeolites* **1984**, 4, 389.
- [46] Dzhigit, et al. *J. Chem. Soc., Faraday Trans. 2* **1979**, 75, 2662.
- [47] Dunne, et al. *Langmuir* **1997**, 13, 4333.
- [48] Stach, et al. *Pure and Applied Chemistry* **1993**, 65, 2193.
- [49] Kotrel, et al. *Journal of Physical Chemistry B* **1999**, 103, 818.
- [50] Denayer, et al. *J. Phys. Chem. B* **1998**, 102, 4588.
- [51] Choudhary and Mayadevi. *Separation Science and Technology* **1993**, 28, 2197.

Recent adsorption isotherms of *n*-alkanes on Ca,Na-LTA-type zeolite afford development of a force field describing the interactions between calcium and *n*-alkanes in Configurational-bias Monte Carlo simulations. The force field of Calero et al. (*J. Am. Chem. Soc.* **2004**, 126, 11377-11386) is able to accurately describe the adsorption properties of linear alkanes in the sodium form of FAU-type zeolites. Here, we extend upon this type of force field by including calcium-type ions. The force field was fitted to reproduce the calcium and sodium cations positions on LTA 5A and the experimental adsorption properties of *n*-alkanes over all range of temperatures and pressures. This opens up a vast amount of experimental data on LTA 5A, both on adsorption and diffusion. Furthermore, evaluation of half a century of reported *n*-alkane adsorption data on LTA-type zeolites indicates that there are many inconsistencies between the various data sets, possibly as a result of (i) undisclosed calcium and sodium contents, (ii) less than perfect drying of the hygroscopic zeolite, and (iii) coadsorption of contaminants such as vacuum grease. Having obtained our force field, and confirmed its reliability on predictions outside the calibration set, we apply the force field on two “open” problems: (a) the heats of adsorption and Henry coefficients as a function of chain length and (b) the effect of cations in LTA-type zeolites. The molecular simulations shed new light on previous experimental findings, and we provide rationalizations on the molecular level that can be generalized to the class of cage/window-type nanoporous materials.



E. García-Pérez, D. Dubbeldam, T.L.M. Maesen, and S. Calero

Influence of Cation Na/Ca Ratio on Adsorption in LTA 5A: A Systematic Molecular Simulation Study of Alkane Chain Length

6.1 Introduction

LTA-type zeolites epitomize how ubiquitous zeolites have become. These zeolites are consumed in large quantities as water softener in detergents and in horticulture, as desiccant in double glazing, and as selective adsorbents for air separation and alkane isomer separation. Unfortunately, the synthesis of more stable (high silica) LTA-type zeolites has only recently been discovered[1] so that LTA-type zeolites have not had a

major impact on catalysis yet. From a scientific point of view, the LTA-type structure is an ideal case study, mainly because the structure is well defined (the positions of the aluminum and the cations are known), the topology is a simple cubic lattice, and there is experimental data on different Ca/Na ratios, cell sizes, and on adsorption and diffusion of alkanes varying from methane up to octadecane. Our main aim is to develop a high-quality force field that reproduces the experimental adsorption data and subsequently make an interpretation of the experimental findings at the molecular level. Up-to-date experiments have been unable to provide the link between macroscopic properties and the positions of the molecules inside the zeolite sample, and here is where the strength of molecular simulations comes into play. The force field developed here affords connecting the location, orientation, and configurations of the molecules with the observed experimental adsorption and diffusion properties for alkanes in a cage/window-type environment.

The structure of Linde type-A (LTA-) zeolite consists of an inner cavity that is large enough for structure changing reactions to take place. Access to this cage is severely restricted so that only relatively small compounds can enter and react, e.g., *n*-paraffins and olefins. The crystallographic unit cell consists of eight large spherical cages (named α -cages) of approximately 1.12 nm interconnected via windows of about 0.41 nm diameter. LTA-type zeolites are often synthesized in their sodium form. The Si/Al ratio is approximately unity with a composition of $[\text{Na}_{96}\text{Al}_{96}\text{Si}_{96}\text{O}_{384}]$. The Ca/Na form can be obtained by replacing the sodium with calcium cations in a postsynthesis exchange. The positions of ions are of critical importance. If they are located in the eight-ring windows, they obstruct the diffusion. The difference between the Na form of the LTA-type zeolite and the Ca/Na form is a good illustration[2]. The Ca/Na form (zeolite 5A) has approximately four calcium and four sodium ions per cage. None of the windows are blocked by an ion, and the free diameter of the windows is 4.1 Å. The Na form (zeolite 4A) contains 12 sodiums per cage and 100 % of the windows are occupied with an ion, partially blocking the window and therefore reducing the effective window size. Exchange with potassium would reduce the window size further (zeolite 3A).

There is an overwhelming amount of experimental data available on adsorption and diffusion in LTA-type zeolites. Despite the small difference in access size between zeolite 4A and 5A, diffusion coefficients in 4A are 4 orders of magnitude lower than in 5A. Because of the slow adsorption kinetics in 4A, equilibration of adsorption isotherms is problematic, and there is little agreement on what constitutes reliable adsorption and diffusion data. Adsorption characteristics of zeolite 5A depend critically on the Ca/Na ratio, but this ratio is not always known or given. The calcium and sodium positions depend on the pretreatment of the zeolite sample (the rate and conditions during the

dehydration/steaming process). For diffusion data, there is the additional problem that the source for discrepancies between different methods for measuring intracrystalline diffusion in zeolites is still unresolved. Recently, a collaborative research project has been initiated, with the aim of making comparative diffusion measurements for selected systems under similar conditions by different experimental techniques[3].

In view of the known problems associated with the cations in 4A and 5A, the discovery of a synthesis for LTA-type silica (ITQ-29)[1] was a welcome event. Well before LTA-type silica had become experimentally accessible, it had already been studied extensively in silico. Fritzsche et al. studied the diffusion of methane in LTA-type zeolite in great detail[4-7]. Bates et al. simulated the energetics of *n*-alkanes from butane to decane in a variety of different all-silica zeolite structures including LTA[8]. Demontis and Suffritti investigated how the sorbate loading controls the diffusion of spherically symmetric Lennard-Jones molecules[9]. Haberlandt discussed diffusion of guest molecules (CH₄, C₂H₆, Xe) in zeolites (LTA-zeolites, silicalite) under different thermodynamic conditions for different intermolecular potentials[10]. The thermal conductivity of model zeolites was investigated using nonequilibrium molecular dynamics calculations by Murashov[11]. Schüring et al. studied the self-diffusion of ethane in cation-free Linde type-A zeolite by molecular dynamics simulations for various temperatures. These simulations predicted that the diffusivity decreases with increasing temperature between 150 and 300 K for a low loading of one molecule per cage[12]. They also developed a random walk treatment of dumb-bell molecules in an LTA zeolite and in chabazite[13]. Dubbeldam et al. simulated self-diffusion coefficients in the range of C₁-C₂₄ at various temperatures[14,15]. Tunca and Ford developed a hierarchical approximation of diffusion and adsorption at nonzero loading in microporous materials using methane in LTA as a test system[16-18]. Beerdsen et al. developed a dynamically corrected transition state theory method capable of computing quantitatively the self-diffusivity of adsorbed molecules in confined systems at nonzero loading. For methane and ethane in the model system, LTA perfect agreement with MD was found[19-21]. Demontis et al. studied the equilibrium probability distribution of *N* methane molecules adsorbed in the interior of *n* α -cages of the all-silica LTA-type zeolite[22]. Recently, Beerdsen et al. constructed a classification of pore topologies based on a free energy match between the molecule and the structure of the confinement[23]. They showed that small alkanes in LTA-type zeolites fall into the class of cage-type zeolites, characterized by an initial *increase* in diffusion over loading followed by the usual decrease with loading close to saturation.

In contrast to LTA-type silica, there are precious few papers discussing LTA-type zeolites complete with the usual sodium or calcium cations. Jaramillo and Chandross performed Gibbs ensemble Monte Carlo simulations for the calculation of adsorption of NH₃, CO₂,

and H₂O on zeolite 4A[24]. It is clear from the above introduction that, for further advancement, a reliable force field for a LTA-type zeolite with an adjustable Na/Ca ratio is desperately needed. The force field of Calero et al. is able to accurately describe the adsorption properties of linear alkanes in the sodium form of FAU-type zeolites[25]. Here, we extend this force field so as to include calcium cations.

The remainder of this paper is organized as follows. We first describe the choice of the functional forms of the force field, the zeolite A structural details, the final force field parameters, and the simulation methods and details. In the Results Section III, we first show the calibration of the Na/Ca-zeolite parameters by reproducing experimentally known crystallographic positions and occupancies. Next, we show the isotherm set of experimental data along with our fitting results used for calibrating the force field. The section with the results is completed with the predictions of our force field along with available experimental data, i.e., isotherms, heats of adsorption, and Henry coefficients.

6.2 Methods

6.2.1 Force field type. The adsorption of hydrocarbons is dominated by dispersion forces. These interactions are notoriously difficult to describe using quantum mechanical approaches. The next level of sophistication is to use an all-atom model. These models are commonly used in the simulations of proteins and other large systems. Given the widespread use of partial atomic charge models, it is important to realize that partial charges cannot be unambiguously assigned to atoms because charge is not an experimentally observable quantity and cannot be unambiguously calculated from the wave function. The united-atom approach circumvents the use of charges. For alkanes in all-silica structures, it was possible to obtain a unique and optimal set of adsorbate–adsorbent parameters[26,27]. The alkane–alkane parameters were taken from refs [28,29]. The structure of these types of force field dates back to Kiselev et al.[30] They assumed that oxygen atoms dominate the interactions between the rigid framework and the guest molecules. This type of force field has only two optimization parameters per pseudo-atom, the strength parameter ϵ , and the size parameter σ of the Lennard-Jones potential. Dubbeldam et al. showed that both can be fitted uniquely by using isotherms with inflections[26]. The shape of the inflections are sensitive to size parameter σ , while the amount adsorbed at a particular pressure is dependent on the strength parameter ϵ . It is interesting to note that more elaborate force fields perform worse for adsorption properties in these systems[27]. This misfit reflects the complexity inherent to optimizing a multitude of parameters. Especially, the addition of charge increases the complexity of the approach, for it implies that the uniqueness of the Lennard-Jones parameters is lost. These parameters now have to be retrofitted assuming the chosen charges. With each step

of sophistication, e.g., polarization, the parametrization becomes more difficult to link to parameters that can be verified or falsified.

For the limited set of alkane adsorption in microporous silicas, Dubbeldam et al. developed a uniquely parametrized force field. Much more experimental data are available on sodium-containing aluminosilicates. Therefore, Calero et al. extended the force field so as to include sodium ions[25]. In an earlier attempt to include ions into these models, Beerdsen et al.[31,32] were among the first to allow the nonframework cations to move instead of keeping them fixed. In the model of Beerdsen et al.[31,32] and Calero et al. [25,33], the zeolite and the nonframework cations are assigned partial charges, but the alkanes are still modeled as united atoms. Note that the charges in these works were taken from Jaramillo and Auerbach[34] and the alkane–alkane interactions from Martin et al.[28,29] The charges are also used to represent some average polarization, while the optimization is focused on reproducing the experimentally known crystallographic positions and occupancies of the nonframework cations. The force field of Calero et al. is able to accurately describe the adsorption properties of linear alkanes in the sodium form of FAU-type zeolites[25]. It reproduces the sodium positions in dehydrated FAU-type zeolites known from crystallography and it predicts how the sodium cations distribute when *n*-alkanes adsorb. More recent works showed that this force field can be successfully extended to MOR- and MFI-type zeolites[35-37].

There are many other force fields published in the literature. The Consistent Valence Force Field (CVFF) for the adsorption of hydrocarbons in MFI gave a reasonable prediction of the adsorption isotherms[38]. Other examples include the model of June et al.[39], the AUA model[40], the models of Vlucht et al.[41], Smit et al.[42], and Jaramillo et al.[24,34]

6.2.2 LTA-type zeolites. The Ca/Na form of the LTA-type structure[43] has a cubic space group *Fm3c* (space group 225), with $a = b = c = 2.4555$ nm and $\alpha = \beta = \gamma = 90^\circ$. The crystallographic unit cell consists of eight large spherical cages (named α - cages) shown in Figure 6.1. In search of LTA-type zeolites with enough silica to be suited for catalysis, ZK-4 zeolite[44] and zeolite α were reported. However, these remained relatively unstable, for their framework Si/Al ratio remained below 1.7 mol/mol. Consistent with replacing long Al–O bonds by shorter Si–O bonds, the unit cell of such a higher silica LTA-type zeolite shrinks from 24.555 Å for Si/Al = 1 mol/ mol to 24.2 Å for Si/Al = 1.67. For recently reported LTA-type silica, the unit cell size is as small as 23.734 Å[1]. LTA-type zeolites obey the Löwenstein rule, i.e., all framework aluminum atoms link via four oxygen atoms to four framework silicon atoms. Because of this strict alternation between aluminum and silicon, capturing the periodicity of the unit cell of

LTA-type zeolites with a silicon-to-aluminum ratio of 1 mol/mol requires *two* cages in each direction. There are three types of rings: six-, eight-, and four-membered oxygen rings. The positions of ions are of critical importance if they are located in the windows obstructing the adsorption through the eight-membered oxygen rings. In addition to the relevant cages and channels, there are also topologically disconnected sites. A methane molecule may fit in, e.g., a β (sodalite) cage, but it cannot access such a site from the main (α or super) cages and channels. Accordingly these inaccessible pockets were artificially blocked in our model.

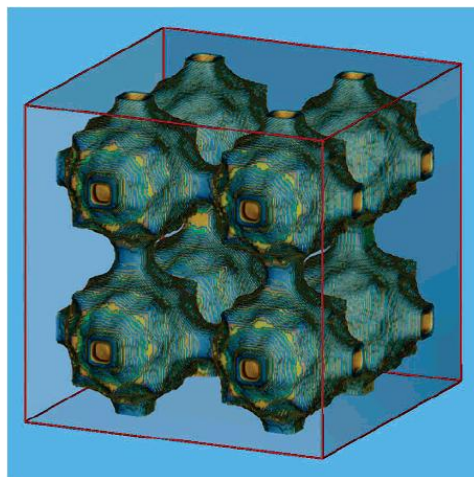


Figure 6.1 Unit cell of the LTA-type zeolite. The dimensions of the cubic unit cell are around 24–24.5 Å. It contains eight cages connected in a cubic arrangement, and each cage is connected to six other cages by windows of about 5 Å in diameter.

6.2.3 Force field model and parameters. The interactions between cations and the zeolite host framework are modeled by Lennard-Jones and Coulomb potentials. The alkane–alkane interactions, alkane–framework interactions, and alkane–cation interactions are modeled by Lennard-Jones potentials only (Table 6.1). The Coulomb interactions in the system are calculated using the Ewald summation[45,46]. The alkanes are described with a united atom model in which CH_x groups are considered as single interaction centers with their own effective potentials[47]. The beads in the chain are connected by harmonic bonding potentials. The bond bending between three neighboring beads is modeled by a harmonic cosine bending potential, and changes in the torsional angle are controlled by a Ryckaert-Bellemans potential. The beads in a chain separated by more than three bonds interact with each other through a Lennard-Jones potential. The interactions of the adsorbed molecules with the zeolite are dominated by the dispersive

forces between the pseudo-atoms and the oxygen atoms of the zeolite[30,41,48] meaning that the silicon van der Waals interactions are taken into account through an effective potential with only the oxygen atoms.

Table 6.1 Lennard-Jones parameters ϵ/k_B [K] in top corner, σ [Å] in bottom corner of each field, partial charges [e] of the framework and the cations, and the bond, bend, and torsion potential and parameters^a.

	O _{Si}	O _{Al}	Si	Al	Na ⁺	Ca ²⁺	CH ₄	CH ₃	CH ₂
CH ₄	115	115			582	590	158.5	130.84	94.21
	3.47	3.47			2.72	2.56	3.72	3.74	3.84
CH ₃	93.0	93.0			443	400	130.84	108	77.7
	3.48	3.48			2.65	2.6	3.74	3.76	3.86
CH ₂	60.5	60.5			310	440	94.21	77.7	56.0
	3.58	3.58			2.95	2.8	3.84	3.86	3.96
Na ⁺	23.0	23.0					582	443	310
	3.4	3.4					2.72	2.65	2.95
Ca ²⁺	18.0	18.0					590	400	440
	3.45	3.45					2.56	2.6	2.8
charge	q = -1.025	q = -1.2	q = +2.05	q = +1.75	q = +1.0	q = +2.0			
bond	$U^{bond} = 1/2 k_1 (r - r_0)^2$								
	$k_1/k_B = 96\,500\text{ K/Å}^2, r_0 = 1.54\text{ Å}$								
bend	$U^{bend} = 1/2 k_2 (\cos\theta - \cos\theta_0)^2$								
	$k_2/k_B = 62\,500\text{ K/Å}^2, \theta_0 = 114^\circ$								
torsion	$U^{torsion} = \sum_{n=0}^5 \eta_n \cos^n \phi$								
	$\eta_n = 0 \dots 5/k_B = \{1204.654, 1947.740, -357.845, -1944.666, 715.690, -1565.572\}$								
LJ	$U_{ij}^{gg, hh, intra} = \begin{cases} 4\epsilon_{ij} \left[\left(\frac{\sigma_{ij}}{r_{ij}} \right)^{12} - \left(\frac{\sigma_{ij}}{r_{ij}} \right)^6 \right] - E_{cut} & \text{if } r < r_{cut} \\ 0 & \text{if } r \geq r_{cut} \end{cases}$								

^a The O-CH_x interactions are taken from our previous works,[26,27] O_{Al} are the oxygens bridging one silicon and one aluminum atom, and O_{Si} are oxygens bridging two silicon atoms, $r_{cut} = 12\text{ Å}$ the cutoff distance, and E_{cut} denotes the energy at the cutoff radius (shifted potential).

In the force field described here, an “average” polarization is included implicitly in the parametrization by means of two effects: the polarization induced by the cation on the zeolite and on the alkanes. For the cation-zeolite interactions, we used the approach of Auerbach[34], taking into account the polarization effects by adjusting the partial charges on the oxygen, depending whether they are connected to Si or Al. Concerning the polarization effects for the cation-alkane interactions, alkanes are very difficult to

polarize, and therefore, a logical approach was to use effective Lennard-Jones interactions between the cations and the alkanes.

It should be noted that effective Lennard-Jones potentials implicitly included many-body interactions (polarization), the contributions arising from instantaneous dipole–quadrupole and quadrupole–quadrupole interactions, flexibility of the framework, etc. The flexibility of the framework has been shown to be a minor effect for adsorption of small alkanes[49].

6.2.4 Grand-Canonical Monte Carlo. In adsorption studies, one would like to know the amount of materials adsorbed as a function of pressure and temperature of the reservoir with which the sieve is in contact. Therefore, the natural ensemble to use is the grand-canonical ensemble (or μ, V, T ensemble). In this ensemble, the temperature T , the volume V , and the chemical potential μ are fixed. The equilibrium conditions are that the temperature and chemical potential of the gas inside and outside the adsorbent must be equal. The imposed chemical potential μ can be related to the fugacity, computed directly from the equation of state of the vapor in the reservoir. For all adsorbates, the experimental equation of state is well-known, and we use the Peng-Robinson equation of state to convert the pressure to the corresponding fugacity, introducing only a small correction for the currently studied systems. Another potential issue can arise at very high pressures where measured excess and computed absolute adsorption are not the same. For our systems, the difference is neglectible (smaller than 1%).

The conventional simulation techniques to compute adsorption isotherms are prohibitively expensive for long alkanes. The Configurational-bias Monte Carlo (CBMC) technique simulates the adsorption isotherms at affordable cost[50]. In a CBMC simulation, chains are grown bead by bead, biasing the growth process toward energetically favorable configurations and avoiding overlap with the zeolite. During the growth, the Rosenbluth factor is calculated. The average Rosenbluth factor is directly related to the excess chemical potential, the free energy, and the Henry coefficient K_H [46,51]. The CBMC algorithm greatly improves the conformational sampling of molecules and increases the efficiency of chain insertions by many orders of magnitude.

6.2.5 Simulation details. The crystallographic positions for the 5A zeolite are taken from Pluth et al.[52] The Si/Al ratio is exactly one, obeying the Löwenstein rule (framework silicon and aluminum strictly alternate). So as to compare with the 5A zeolite used by Ruthven et al., we employed 36 Ca^{2+} and 24 Na^+ per unit cell. To compare with Schirmer et al.[53], we used 32 Ca^{2+} and 32 Na^+ per unit cell. The simulations were performed using one unit cell with eight cages. Test simulations using $2 \times 2 \times 2$ gave

identical results but were deemed too computationally expensive for use with the Ewald summation for all the simulations. The Ewald summation is the most accurate way of computing the Coulomb energy in truly periodic systems, and in all our simulations, the convergence parameter was chosen as $\alpha = 0.3$, with $k = 9$ wave vectors for high accuracy.

Simulations are performed in cycles, and in each cycle, one move is chosen at random with a fixed probability of performing a molecule displacement (10 %), rotation around the center of mass (10 %), exchange with the reservoir (60 %), partial regrowth of a molecule (10 %), and a full regrowth at a random position (10 %). The maximum translational and rotational displacements are adjusted to achieve an acceptance probability of 50 %. The total number of cations remains constant during simulations so only translation movements and regrowth at a random position in the zeolite are considered for this type of particles. The regrowing at a new, randomly selected position bypasses energy barriers and allows for fast equilibration.

For the NVT simulations, the total number of cycles was at least 5×10^5 . For the grand-canonical simulations, the number of cycles for isotherms was at least 1×10^6 . Note that, in one cycle, one Monte Carlo move is attempted *per particle*. The number of Monte Carlo steps is the number of cycles times the average number of particles. More details on this simulation technique can be found elsewhere[25-27,41,46].

6.3 Results

6.3.1 Calibration of zeolite–ion interactions. The Na–O interactions were calibrated to reproduce the experimentally known positions in LTA 4A, assuming a charge of $q = +1$ for sodium. Crystallographic studies indicate that these sites are occupied for 97.2, 24.2, and 6.6 %, respectively. Molecular simulations with our optimized force field yield occupations of 100, 23.9, and 6.25 %, respectively. In addition, the crystallographic locations of the sites obtained through molecular simulations are within 0.2 Å from those obtained through X-ray diffraction. Using this set of parameters derived from this high-alumina LTA-type zeolite, we previously validated the potentials by computing the average sodium–oxygen distances in FAU-type zeolite[25].

This work uses a realistic description of the interaction between the sodium and calcium cations, the zeolite framework, and the alkanes. We performed simulations to obtain the average calcium–oxygen distances and calcium occupancies in LTA zeolite. The resulting calcium–oxygen distances and calcium occupancies are listed in Tables 6.2 and 6.3, respectively.

Table 6.2 Ca²⁺–O distances [Å] in LTA compared with Firor and Seff[54], Moon et. al.[55] Jang et al.[56], Pluth and Smith[57], and Adams and Haselden[58].

	this work	Firor	Moon	Jang	Pluth	Adams
Ca(I) – O(3)	2.328	2.328	2.224	2.098	2.273	2.287
Ca(II) – O(3)	2.244	2.272	2.307	2.158		
Ca(III) – O(3)	2.273	2.356	2.268	2.265	2.317	
Ca(IV) – O(1)	2.412	3.08				
Ca(V) – O(2)	2.454	3.0				

Table 6.3 Ca site occupancies in LTA compared to the experimental data of Firor and Seff[54].

	Ca I	Ca II	Ca III	Ca IV
this work	42.1	1.6	4.3	0
exptl data	24	8	8	8

6.3.2 Calibration on isotherms. Experimentally, measurements of adsorption and diffusion in Ca/Na forms of LTA are challenging. First, there are differences in the Ca/Na cation ratio. In addition, there might be trace of other cations, e.g., potassium, present. Second, diffusion of linear alkanes, especially for the longer ones, is quite slow. This results in very long equilibration times for higher pressures and lower temperatures. Third, Ca/Na forms are highly hydrophilic, so that avoiding water adsorption requires special care. Finally, there are the usual issues when dealing with nanoporous materials: the form of the sample (pellets with binder or crystals), adsorption on the exterior, the quality of the sample, etc. Ideally, one would like to calibrate a force field on various data sets from different authors. From the graphs in the next section, it can be seen that agreement between the various sets is generally only qualitative. We opted for utilizing Ruthven’s data as the calibration set because of the large amount of consistent data from a single trustworthy source, obtained through contemporary measurement methods with great care for the quality of the crystal samples. The parameters of methane and ethane could be fitted on the data of Ruthven and co-workers[59-61] with great accuracy (Figure 6.2). The overlap of the curves is excellent, i.e., the shape of the isotherms matches at all three temperatures. We have added the isotherm of Loughlin to show that the data for methane are similar but slightly different for different authors. From methane, we obtained the Ca–CH₄ parameter, and from ethane, we obtained Ca–CH₃. The data for propane[59,61,62] is used to obtain Ca–CH₂ and is illustrative for the problems one faces when designing and fitting force fields. First, we note that the data of Grande are different for pellets than for crystals. Obviously, the materials are different, the material based on pellets includes binder, but a correction for the influence of the binder is not trivial. Next,

we note that the data of Grande differ from the data of Ruthven, although they are in general agreement. Finally, when fitted on the data of Ruthven, we obtain excellent agreement for 358, 358, and also for 273 K, but *not* for 323 K. Still, there is some support that the simulation data at 323 K might still be correct: the data are consistent, i.e., the spacing over temperature is what you expect, and the simulation data agrees with Grande pellets at 323 K (and extrapolated 423 K).

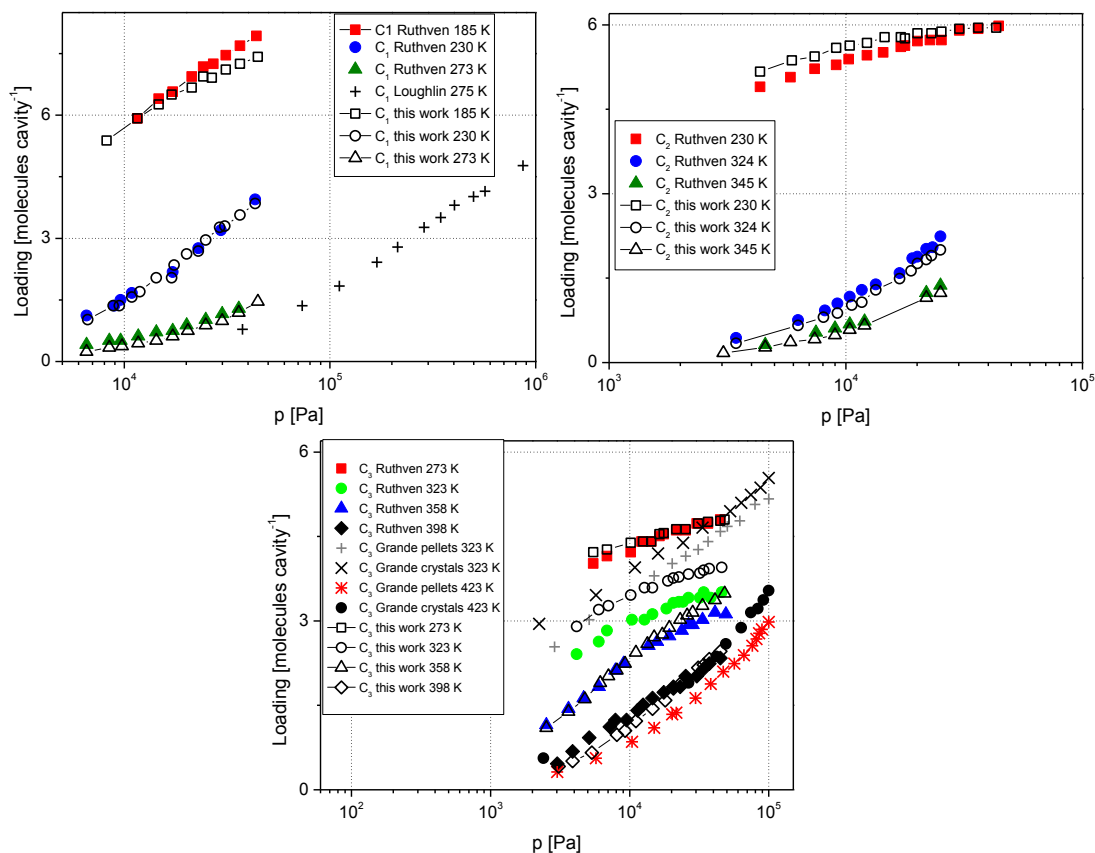


Figure 6.2 Isotherms of linear alkanes used in the *calibration set* of the force field (left) methane, (right) ethane, (middle) propane, in Ca/Na-LTA at various temperatures. Experimental data are taken from Ruthven and co-workers.

6.3.3 Predictions of isotherms. Having obtained the Ca-CH₃ parameters from ethane and the Ca-CH₂ parameters from propane, we are able to make predictions for isotherms on longer alkanes and check the validity of the parameters. The data for butane

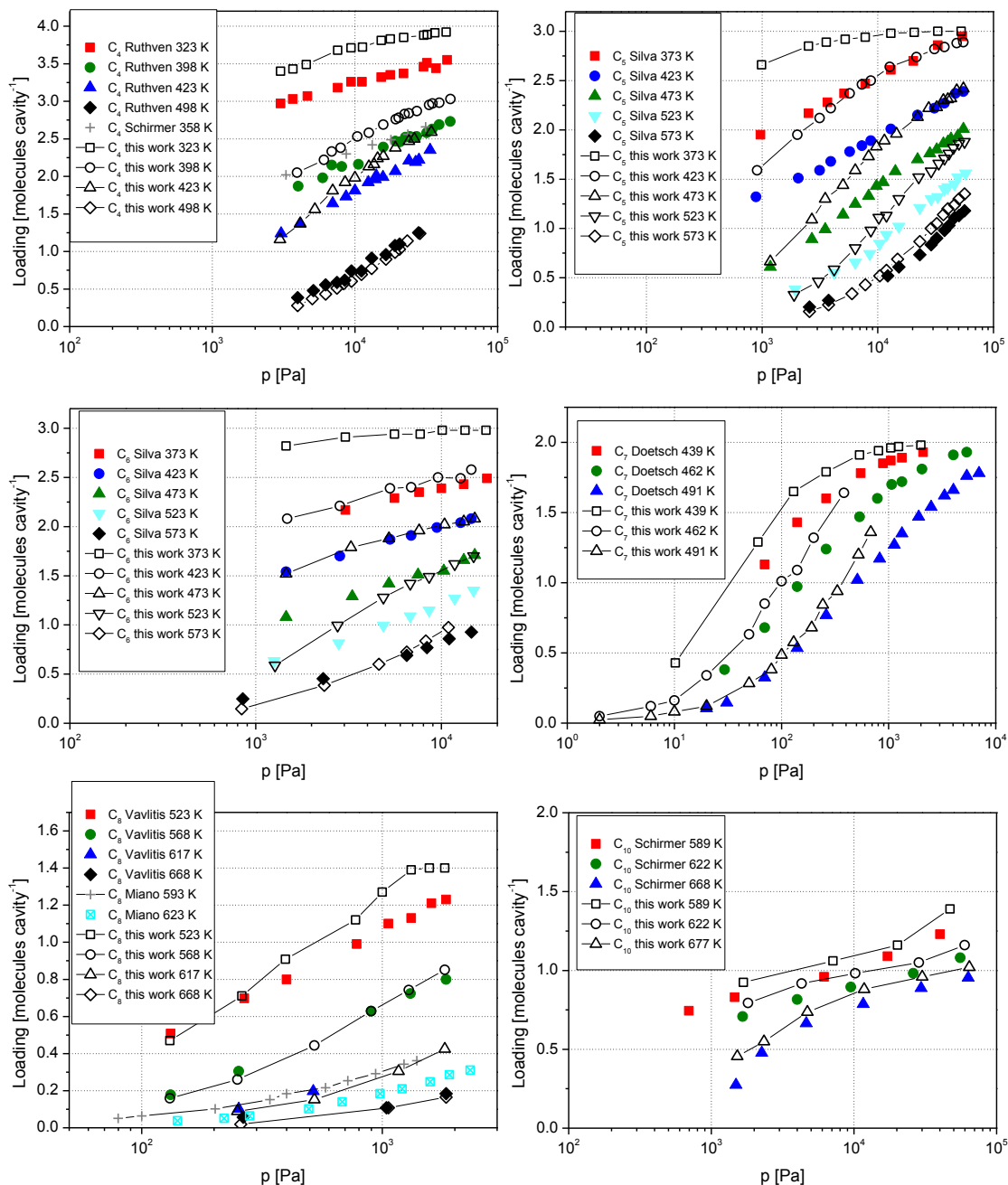


Figure 6.3 Predictions of isotherms of butane to decane compared to various experimental data. are taken from refs [59,63], the data for the medium chain length alkanes are taken from refs [64-68], and the data on the longest alkanes reported here are taken from ref [53].

We have plotted the predictions of our force field in Figure 6.3. For butane, we trace the shape of the curves well, but deviate from the data of Ruthven at the lowest temperatures. The same applies to pentane and hexane and the experimental data of Silva and Rodrigues. However, for heptane, we agree well with Doetsch, for octane, there is remarkable agreement with Vavlitis and Miano, and for decane, we agree very well with Schirmer[53]. We note that the Ca/Na ratio of the samples used by these various authors differ and sometimes are not reported. The adsorption isotherms of long alkanes are plotted in Figure 6.4. The data of Schirmer are for moderate to high loading.

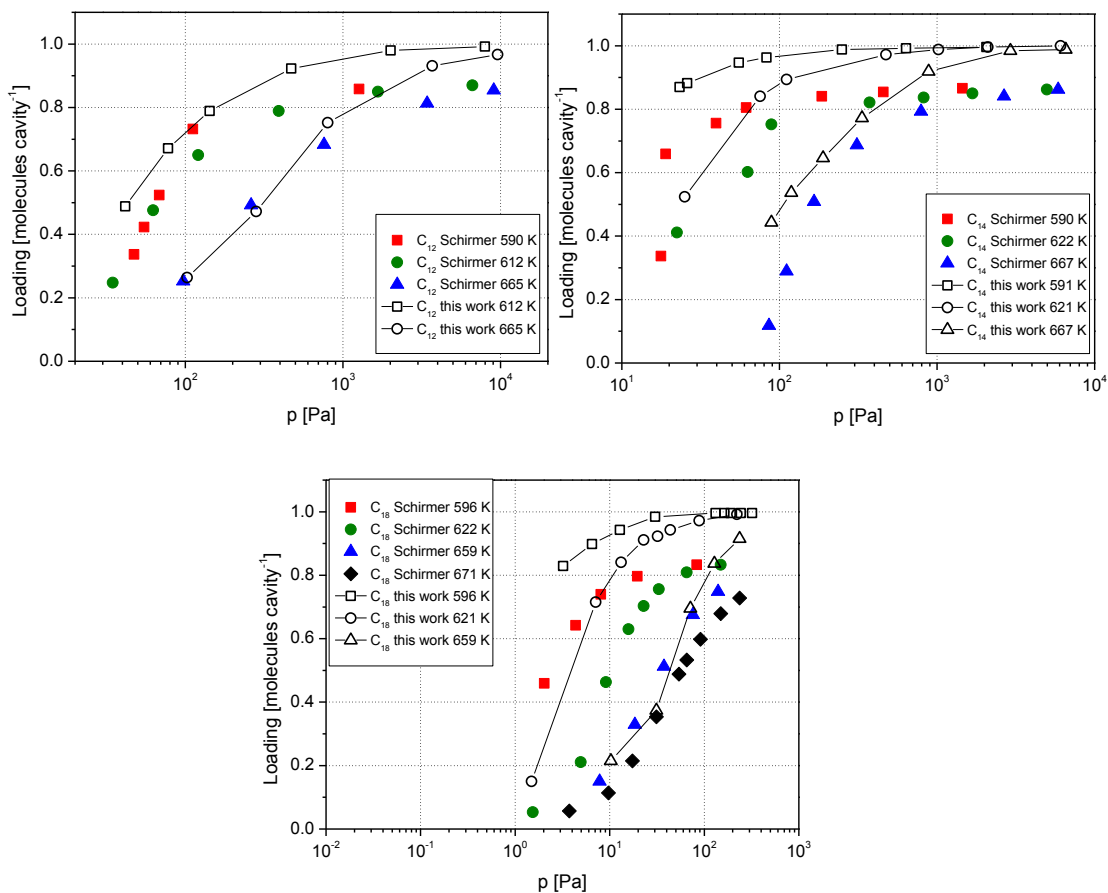


Figure 6.4 Predictions for long alkane: C₁₂, C₁₄, and C₁₈ at various temperatures in Ca/Na-LTA compared to experimental data of Schirmer.

For these loadings, differences between simulation and experiment are to be expected because simulation uses perfect crystals and real samples contain defects. However, for C₁₂, C₁₄, and C₁₈, the difference is systematic and agreement is good.

6.3.4 Predictions of Henry coefficients and heats of adsorption. At low pressures, the loading is linear in pressure with the Henry coefficient as the proportionality constant. A high Henry coefficient means that the zeolite is a strong adsorbent, at least at low loadings. The Henry coefficients for the Ca/Na form and siliceous LTA form obtained from simulation are compared to experimental data in Figure 6.5. Excellent agreement between the simulations and the experimental data can be observed. Note that the log of the Henry coefficients is not linearly increasing with carbon number. We stress that the Henry coefficients are predictions from our force field and were *not* included in the calibration set. When the log of the Henry coefficients is plotted versus the inverse temperature, two quantities can be obtained: the heat of adsorption as the slope, and the preexponential Henry coefficients as the intersection with the y-axis. The heats of adsorption are plotted in Figure 6.6 along with experimental data of Ruthven and other authors. For reference, we have included the simulation data on LTA-type silica with the same unit cell as 5A and for LTA-type silica proper (i.e., with the much smaller unit cell size).

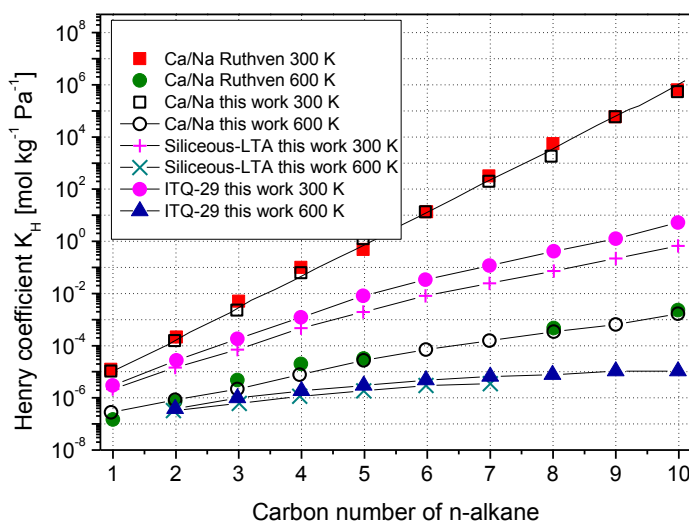


Figure 6.5 Henry coefficients for the Ca/Na form and siliceous LTA form obtained from simulation compared to experimental data of Ruthven et al. as a function of chain length at 300 and 600 K. At low pressures, the loading is linear in the pressure with the Henry coefficient as the proportionality constant.

The smallest unit cell size yields a better adsorption energy. A single experimental point on LTA-type silica (39 kJ/mol) agrees well with our simulation value (42 kJ/mol). Both are well below the value for zeolite 5A (60 kJ/mol). In Table 6.4, we have summarized

the comparison with the data of Ruthven. The agreement is excellent for heats of adsorption and good for the preexponential Henry coefficients.

The preexponential Henry coefficients for zeolite 5A simulations, LTA-type silica with and without unit cell correction, are plotted in Figure 6.7. The agreement with Ruthven is good for higher chain lengths. Some interesting effects can be seen here. The simulation shows the expected behavior, a strictly decreasing curve, with the 5A zeolite lower than the other two. Note that the data show two regimes; around $C_{6/7}$, the curves have a different slope. This slope of $\log(K_\infty)$ plotted as a function of carbon number is related to the entropy ΔS per carbon number. Up to medium chain lengths, the chain loses entropy linearly with carbon number compared to the gas phase. As soon as the molecule feels the other side of the cage, the molecule is forced to bend, thereby being even more restricted in freedom.

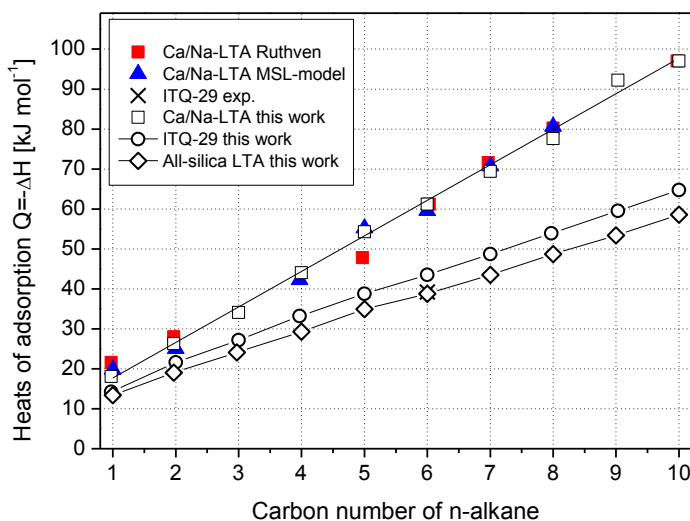


Figure 6.6 Heats of adsorption for the Ca/Na form and siliceous LTA form obtained from simulation compared to experimental data of Ruthven et al. as a function of chain length.

6.3.5 Effect of cations. An important observation can be made: the difference between zeolite 5A and LTA-type silica becomes many orders of magnitude for increasing chain lengths. The difference becomes even more pronounced at lower temperatures. In Figure 6.8, we have plotted the adsorption of decane at 300 K by examining the influence of the Ca/Na ratio. As can be seen, adsorption increases with the *amount* of ions present in the α -cages of LTA 5A. The amount is more important than the type of ions. LTA 4A with 96 sodium ions would show very high adsorption capacity, but

unfortunately also have all the eight-ring windows blocked. Methane and ethane would diffuse at acceptable rates (for practical purposes), but the diffusivities of longer alkanes are very low. Experimental data on LTA 4A are scattered and almost impossible to determine for the longest alkanes due to the excessively long equilibration times. Here, we show that also for LTA 5A much of the scatter can be explained by differences in the Ca/Na ratio and, therefore, in the amount of ions present. The Ca/Na ratio influences not only adsorption properties, but also diffusion and equilibration times.

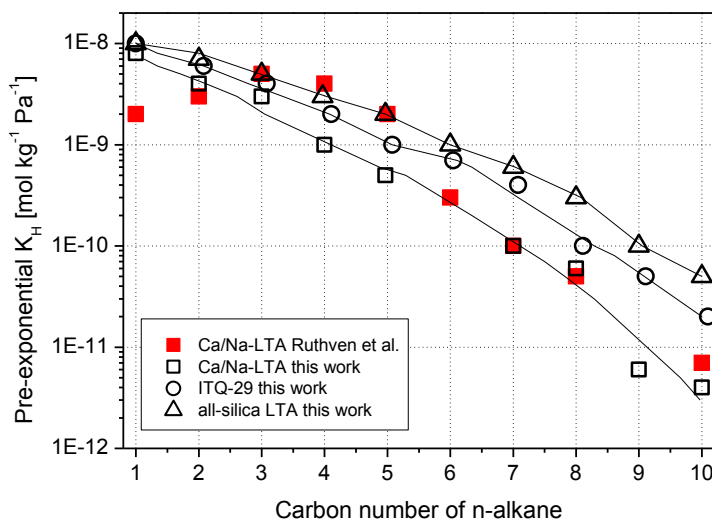


Figure 6.7 Preexponential Henry coefficients in log scale for the Ca/Na form, ITQ-29 siliceous LTA form obtained from simulation, and experimental data on Ca/Na-LTA of Ruthven et al. as a function of chain length.

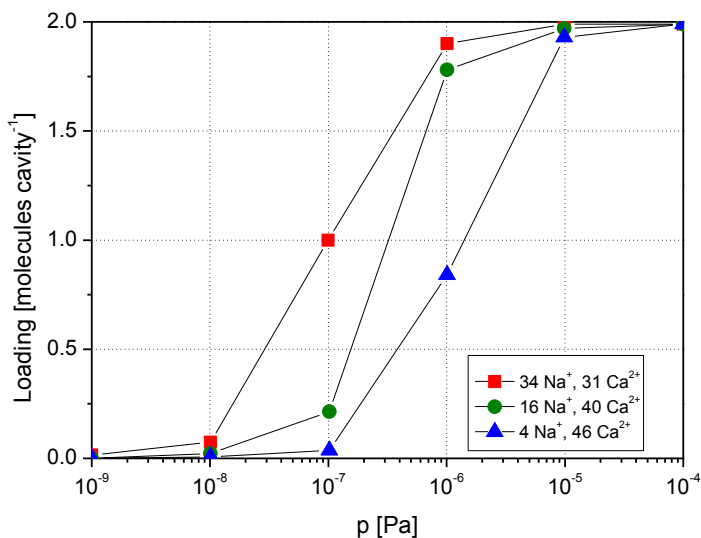


Figure 6.8 Influence of the Ca/Na ratio on adsorption of decane in LTA 5A at 300 K. Adsorption increases with the amount of ions present in the α -cages. LTA 4A has 96 Na ions and would have a very high adsorption capacity, but in LTA 4A, all eight-ring windows are blocked, rendering it practically useless for alkane adsorption.

Table 6.4 Comparison of our simulations results of low-coverage properties in Ca/Na-LTA with the experimental results of Ruthven et al.^a

CN	K_{∞} [mol/kg/Pa]		$-\Delta H$ [kJ/mol]	
	sim	exptl	sim	exptl
1	1.5×10^{-8}	1.9×10^{-9}	16.7	21.8
2	3.7×10^{-9}	3.3×10^{-9}	26.3	27.6
3	2.8×10^{-9}	5.2×10^{-9}	33.9	33.9
4	1.1×10^{-9}	3.6×10^{-9}	44.2	42.7
5	4.4×10^{-10}	2.3×10^{-9}	54.1	47.7
6	3.2×10^{-10}	3.2×10^{-10}	60.8	61.1
7	1.4×10^{-10}	9.5×10^{-11}	69.4	71.6
8	5.6×10^{-11}	4.7×10^{-11}	77.2	80.4
9	6.3×10^{-12}		91.3	
10	4.0×10^{-12}	7.6×10^{-12}	97.1	97.1

^a Both the Ruthven and the simulation Henry coefficients K_H of the linear alkanes have been fitted to $K_H = K_{\infty} e^{(-\Delta H/RT)}$ in the temperature range $T = 300$ - 600 K. Here K_{∞} denotes the pre-exponential Henry coefficient, ΔH the enthalpy of adsorption, and $R = 8.31451 \text{ J mol}^{-1} \text{ K}^{-1}$ the gas constant.

6.4 Conclusions

We have calibrated a new force field for Ca/Na-aluminosilicates applicable over a wide range of Si/Al ratios. The calibration set was the data of Ruthven for methane, ethane, and propane. The predicted isotherms show good agreement with other experimental isotherms although the scatter in the experimental data is large. The predicted heats of adsorption and Henry coefficient show almost perfect agreement. In addition to zeolite 5A, we also computed the heats of adsorption and Henry coefficients for the newly synthesized LTA-type silica. The only experimental data point for the heat of adsorption was in very good agreement with the value computed for this silica. Simulation and experimental data present differences in the Na/Ca ratios and in the equilibration times that can possibly explain the discrepancies between simulations and experiment, and between experimental datasets.

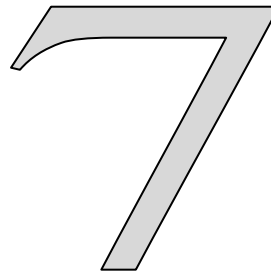
Bibliography

- [1] Corma, et al. *Nature* **2004**, 431, 287.
- [2] Kaerger and Ruthven *Diffusion in Zeolites and other Microporous Solids*; Jonh Wiley & Sons: New York, 1992.
- [3] Jobic, et al. *Adsorption-Journal of the International Adsorption Society* **2005**, 11, 403.
- [4] Fritzsche, et al. An MD Study of Methane Diffusion in Zeolites of Structure Type LTA. In *Zeolites and Related Microporous Materials: State of the Art 1994*, 1994; Vol. 84; pp 2139.
- [5] Fritzsche, et al. *Journal of Molecular Modeling* **1996**, 2, 286.
- [6] Fritzsche, et al. *Chemical Physics Letters* **1998**, 296, 253.
- [7] Fritzsche, et al. *Chemical Physics* **2000**, 253, 283.
- [8] Bates, et al. *J. Am. Chem. Soc.* **1996**, 118, 6753.
- [9] Demontis and Suffritti. *J. Phys. Chem. B* **1997**, 101, 5789.
- [10] Haberlandt. *Thin Solid Films* **1998**, 330, 34.
- [11] Murashov. *Journal of Physics-Condensed Matter* **1999**, 11, 1261.
- [12] Schuring, et al. *J. Chem. Phys.* **2002**, 116, 10890.
- [13] Schuring, et al. Random walk treatment of dumb-bell molecules in an LTA zeolite and in chabazite. In *Recent Advances in the Science and Technology of Zeolites and Related Materials, Pts a - C*, 2004; Vol. 154; pp 2110.
- [14] Dubbeldam, et al. *Physical Review Letters* **2003**, 90, 245901.
- [15] Dubbeldam and Smit. *Journal of Physical Chemistry B* **2003**, 107, 12138.
- [16] Tunca and Ford. *Journal of Chemical Physics* **1999**, 111, 2751.
- [17] Tunca and Ford. *Journal of Physical Chemistry B* **2002**, 106, 10982.
- [18] Tunca and Ford. *Chemical Engineering Science* **2003**, 58, 3373.

- [19] Beerdsen, et al. *Physical Review Letters* **2004**, 93.
- [20] Dubbeldam, et al. *Journal of Chemical Physics* **2005**, 122.
- [21] Beerdsen, et al. *Journal of Physical Chemistry B* **2006**, 110, 22754.
- [22] Demontis, et al. *Journal of Physical Chemistry B* **2005**, 109, 18081.
- [23] Beerdsen, et al. *Physical Review Letters* **2006**, 96.
- [24] Jaramillo and Chandross. *Journal of Physical Chemistry B* **2004**, 108, 20155.
- [25] Calero, et al. *Journal of the American Chemical Society* **2004**, 126, 11377.
- [26] Dubbeldam, et al. *Physical Review Letters* **2004**, 93.
- [27] Dubbeldam, et al. *Journal of Physical Chemistry B* **2004**, 108, 12301.
- [28] Martin and Siepmann. *Journal of Physical Chemistry B* **1999**, 103, 4508.
- [29] Martin, et al. *Journal of Chemical Physics* **2001**, 114, 7174.
- [30] Bezus, et al. *Journal of the Chemical Society-Faraday Transactions II* **1978**, 74, 367.
- [31] Beerdsen, et al. *Journal of Physical Chemistry B* **2003**, 107, 12088.
- [32] Beerdsen, et al. *J. Phys. Chem. B* **2002**, 106, 10659.
- [33] Calero, et al. *Journal of Physical Chemistry B* **2006**, 110, 5838.
- [34] Jaramillo and Auerbach. *Journal of Physical Chemistry B* **1999**, 103, 9589.
- [35] Garcia-Perez, et al. *Applied Surface Science* **2005**, 252, 716.
- [36] Garcia-Perez, et al. *Molecular Sieves: From Basic Research to Industrial Applications, Pts a and B* **2005**, 158, 1097.
- [37] Liu and Smit. *Physical Chemistry Chemical Physics* **2006**, 8, 1852.
- [38] Macedonia and Maginn. *Molecular Physics* **1999**, 96, 1375.
- [39] June, et al. *Journal of Physical Chemistry* **1992**, 96, 1051.
- [40] Pascual, et al. *Physical Chemistry Chemical Physics* **2003**, 5, 3684.
- [41] Vlugt, et al. *J. Phys. Chem. B* **1999**, 103, 1102.
- [42] Smit, et al. *Faraday Discuss.* **1997**, 106, 93.
- [43] Pluth and Smith. *J. Am. Chem. Soc.* **1980**, 102, 4704.
- [44] Kerr. *Inorganic Chemistry* **1966**, 5, 1537.
- [45] Allen and Tildesley *Computer Simulations of Liquids*; Clarendon Press: Oxford, 1987.
- [46] Frenkel and Smit *Understanding Molecular Simulation, 2nd ed.*; Academic Press: London, 2002.
- [47] Ryckaert and Bellemans. *Faraday Discussions* **1978**, 95.
- [48] Kiselev, et al. *Zeolites* **1985**, 5, 261.
- [49] Vlugt and Schenk. *J. Phys. Chem. B* **2002**, 106, 12757.
- [50] Smit and Maesen. *Nature* **1995**, 374, 42.
- [51] Smit and Siepmann. *Journal of Physical Chemistry* **1994**, 98, 8442.
- [52] Pluth and Smith. *Journal of the American Chemical Society* **1980**, 102, 4704.
- [53] Schirmer, et al. In *Molecular Sieves*. In *Proc. 1st International Conference on Zeolites*; Society of Chemical Industry London, 1968; pp 276.

- [54] Firor and Seff. *Journal of the American Chemical Society* **1978**, *100*, 3091.
- [55] Moon, et al. *Bulletin of the Korean Chemical Society* **1993**, *14*, 356.
- [56] Jang. *Korean J. Cryst.* **1990**, *1*, 76.
- [57] Pluth and Smith. *Journal of the American Chemical Society* **1983**, *105*, 2621.
- [58] Adams and Haselden. *Journal of Solid State Chemistry* **1984**, *51*, 83.
- [59] Ruthven and Loughlin. *J. Chem. Soc., Faraday Trans. I* **1972**, *68*, 696.
- [60] Ruthven. *Aiche Journal* **1976**, *22*, 753.
- [61] Loughlin, et al. *Industrial & Engineering Chemistry Research* **1990**, *29*, 1535.
- [62] Ruthven and Derrah. *Canadian Journal Chemistry Engineering* **1992**, *50*, 743.
- [63] Ruthven and Loughlin. *Chemical Engineering Science* **1971**, *26*, 1145.
- [64] Silva and Rodrigues. *Industrial & Engineering Chemistry Research* **1997**, *36*, 493.
- [65] Silva and Rodrigues. *Aiche Journal* **1997**, *43*, 2524.
- [66] Doetsch, et al. *Canadian Journal of Chemistry-Revue Canadienne De Chimie* **1974**, *52*, 2717.
- [67] Vavlitis, et al. *Journal of Colloid and Interface Science* **1981**, *84*, 526.
- [68] Miano. *Colloids and Surfaces a-Physicochemical and Engineering Aspects* **1996**, *110*, 95.

Molecular simulations were carried out to obtain the adsorption and diffusion properties of alkanes in a variety of zeolitic structures of industrial importance by varying the positions of the aluminum atoms. Our results show that adsorption properties of some of these zeolites are not sensitive to the aluminum distribution, while for another class of structures the distribution does matter. Based on these findings we propose a relation between adsorption/diffusion properties and aluminum distributions that can be exploited for designing more-efficient industrial adsorbents.



E. García-Pérez, D. Dubbeldam, B. Liu, B. Smit, and S. Calero

A Computational Method To Characterize Framework Aluminum in Aluminosilicates

Zeolites are aluminosilicates that are used in many applications involving catalysis, separation, and gas storage[1-3]. Unlike the Si/Al ratio of their framework, the location of the aluminum atoms is not well described. It has proved difficult to establish the local structure surrounding the aluminum sites by diffraction methods, since aluminum and silicon are very close in X-ray scattering power and thus XRD gives only the weighted average of the Si–O and Al–O distances. Extended X-ray absorption fine structure (EXAFS) spectroscopy can be used to probe the local structure around aluminum in zeolites. This information is less accurate than the average from XRD, but the ability of EXAFS to probe the local structure around a selected element allows easy in situ measurements[4]. Aluminum X-ray adsorption near edge structure (XANES) spectroscopy can also be used to extract such information, although it does not yield interatomic distances[5]. Several attempts have been made to probe structural variations by MAS-NMR spectroscopy[6-8], but as soon as even small amounts of aluminum are present in the framework, the resolution is degraded and the spectra provide insufficient information about aluminum site preferences[9].

These experimental challenges, combined with the importance of aluminum site distributions, have created a significant opportunity for molecular modeling, and important additional information about the local structure surrounding aluminum sites has come from simulations[7,10-13]. The aluminum distribution on the crystal level, as well as the distribution on the level of a single unit cell, remains a subject of debate[14-20]. Herein, we present an alternative theoretical approach in which we identify those

experimentally accessible properties that are crucially dependent on the aluminum distribution and associated cation distribution. Once these properties have been identified, we compute the most likely positions of aluminum in zeolites by matching simulation results with available experimental data. This crucially depends on the quality of the force field. Recently, two force fields were developed for sodium and protons in aluminosilicates that gave results that were not only qualitatively but also quantitatively in good agreement with experiments[21,22].

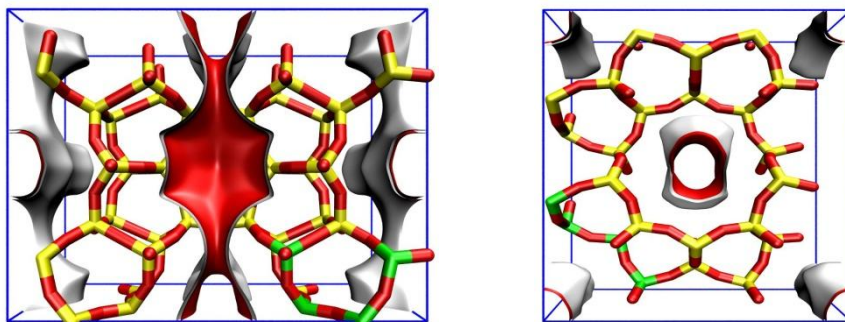


Figure 7.1 Units cells of FER- (left) and TON- (right) zeolites. O red, Si yellow, and the four crystallographically different T-atoms green.

We have performed molecular simulations to obtain the adsorption and diffusion properties of alkanes in a variety of zeolitic structures of industrial importance[23] by varying the positions of the aluminum atoms. Figure 7.1 shows the unit cells of FER and TON along with the four different crystallographic positions of the silicon and/or aluminum atoms (T-atoms). Although distributions over larger supercells may exist[14], our approach implicitly assumes a homogeneous aluminum distribution for the zeolite which is the same for each crystallographic unit cell. However, the method presented herein is in principle applicable to larger scale orderings. The best calibrated and optimized models for adsorption in these structures are the united-atom models, in which the CH_x groups of alkanes are represented as single, chargeless interaction centers with their own effective potentials[22]. Recently, these models also gave quantitative agreement with neutron scattering experiments for collective and transport diffusivity of ethane in silicalite[24].

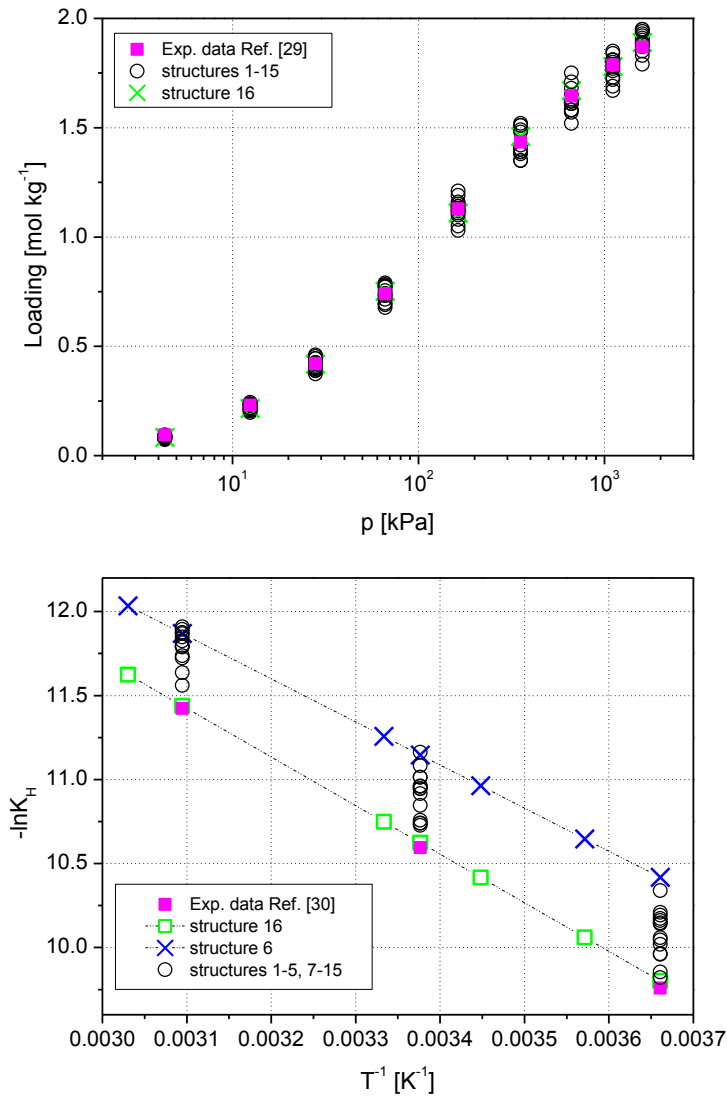


Figure 7.2 Adsorption of methane in $\text{Na}^+[\text{Al}_8\text{Si}_{40}\text{O}_{96}]$ -MOR obtained by molecular simulations in comparison with experimental data[28,29]. (Top) Adsorption isotherms at 293 K. (Down) Henry coefficients K_H [mol kg⁻¹ Pa⁻¹] as a function of temperature.

The force field we used implicitly includes an “average” polarization in the parameterization by means of the polarization effect induced by the nonframework ions on the zeolite and on the alkanes[21,22,25,26]. Adsorption and diffusion studies were

performed by means of Monte Carlo (MC) and molecular dynamics (MD) simulations, respectively. Further details are given in reference [27]. Henry coefficients of linear alkanes were computed for all structures at a fixed Si/Al ratio by varying the aluminum distribution and using Na^+ and H^+ as nonframework ions. Our results show that adsorption properties of certain zeolitic structures are insensitive to the aluminum distribution, while for another class of structures the distribution does matter. Structures such as LTA, MFI, FAU, and MEL are included in the first group, while LTL, MOR, FER, and TON belong to the second class (for small alkanes). The first group was previously used to unambiguously parameterize our simulation method[22,30], and with the second group we can reverse-engineer the average aluminum distribution.

To discuss and illustrate the method to identify the aluminum positions, we carefully analyzed three zeolites for which experimental data are available for comparison and it is also feasible to consider all possible aluminum distributions per unit cell: $\text{H}^+[\text{AlSi}_{23}\text{O}_{48}]$ -TON and $\text{H}^+[\text{AlSi}_{35}\text{O}_{72}]$ -FER (with 4 possible aluminum distributions per unit cell shown in Figure 7.1), and $\text{Na}^+_{8}[\text{Al}_8\text{Si}_{40}\text{O}_{96}]$ -MOR (with 16 possible aluminum distributions per unit cell).

The adsorption of alkanes in Na-MOR is strongly influenced by the aluminum distribution (Figure 7.2). Adsorption isotherms were calculated at 293 K for the 16 structures and compared with available experimental data[28] (Figure 7.2-top). Detailed adsorption behavior at low pressures is shown in Figure 7.2 (bottom), where Henry coefficients are computed at several temperatures. Methane shows the highest adsorption in structure 16 (Al atoms replace Si4, Si18, Si31, Si42, Si80, Si93, Si105, and Si115) and the lowest for structure 6 (Al atoms replace Si3, Si18, Si32, Si42, Si79, Si93, Si106, and Si115). The agreement with experimental values[29] is remarkable for structure 16. In this structure the eight Al atoms are located in the 4-rings, in complete conformity with the suggested preferential sites of aluminum provided by previous crystallographic, experimental, and theoretical work[16,19,31-34].

The method is transferable to other protonated aluminosilicate structures, as shown in Figures 7.3 and 7.4 for H-FER and H-TON-type zeolites, respectively. Simulations were performed for propane, butane, pentane, hexane, heptane, octane, and nonane for all feasible protonated structures (four possible Al positions for each zeolite). Structures with aluminum substitutions at Si1, Si2, Si3, and Si4 are labeled as structures 1, 2, 3, and 4, respectively. Direct comparison with the experimental values[35,36] predicts that most of the aluminum atoms in the experimental zeolite sample substituted Si3 in H-FER structures, and Si3 and Si4 in H-TON structures.

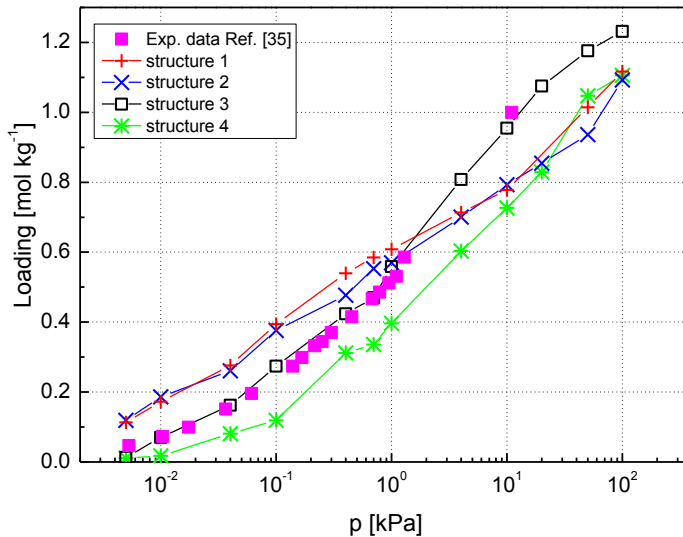


Figure 7.3 Adsorption isotherms of pentane in $H^+[AlSi_{35}O_{72}]$ -FER at 333 K obtained by molecular simulations and compared with experimental data[35]. Simulations were performed with 16 unit cells. The structure numbering is independent from that in Figure 7.2.

Diffusion coefficients of methane and ethane in TON and FER structures were computed (Table 7.1). Diffusion of methane and ethane is faster in FER structures than in TON structures. According to our results both types of structure provide lower diffusivity when Si3 and Si4 are substituted and the highest when Si2 and Si1 are substituted. Substitutions in Si2 and Si1 provide similar diffusivity to pure-silica TON and FER, respectively. We note that the idea of reverse-engineering aluminum positions is not restricted to adsorption properties alone but, when experimental data become available, could also be applied to diffusion or other dynamic information.

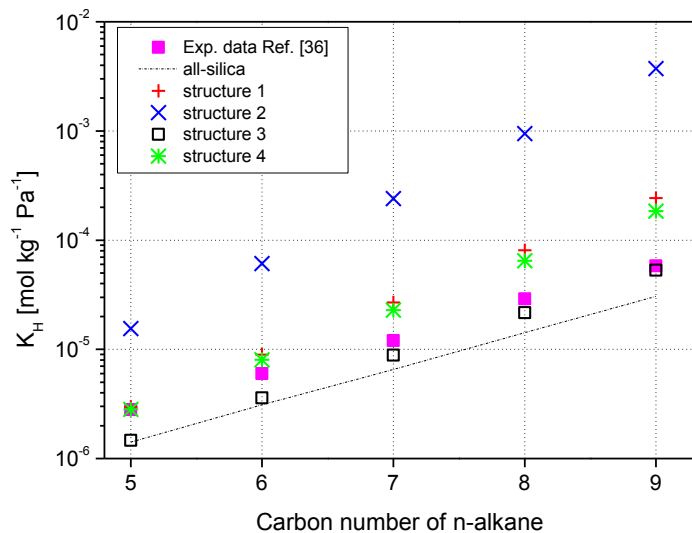


Figure 7.4 Calculated Henry coefficients as a function of the carbon number for the adsorption isotherms of linear alkanes –pentane, hexane, heptane, octane, and nonane– in $\text{H}^+[\text{AlSi}_{23}\text{O}_{48}]$ -FER at 548 K compared with experimental data[36]. Simulations were performed with 16 unit cells. The structure numbering is independent from that in Figure 7.3.

Table 7.1 Diffusion coefficients [$10^{-8}\text{m}^2\text{s}^{-1}$] of linear alkanes in $\text{H}^+[\text{Al}_1\text{Si}_{23}\text{O}_{48}]$ -TON and $\text{H}^+[\text{Al}_1\text{Si}_{35}\text{O}_{72}]$ -FER at 548 K.

	H-TON		H-FER	
	Methane	Ethane	Methane	Ethane
pure silica	0.74 ± 0.01	0.49 ± 0.01	2.2 ± 0.1	0.89 ± 0.03
structure 1	0.43 ± 0.04	0.29 ± 0.02	2.6 ± 0.1	1.04 ± 0.05
structure 2	0.67 ± 0.03	0.47 ± 0.04	1.5 ± 0.1	0.59 ± 0.04
structure 3	0.26 ± 0.01	0.22 ± 0.01	1.1 ± 0.1	0.31 ± 0.04
structure 4	0.39 ± 0.03	0.29 ± 0.04	1.3 ± 0.1	0.39 ± 0.05

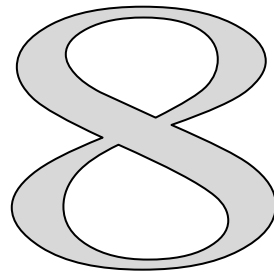
The field of molecular simulation is rapidly expanding, and future advances in force fields could lead to similar approaches for other systems. The presented relation between adsorption/diffusion properties and aluminum distributions can be exploited for designing more-efficient industrial adsorbents. It should be possible, in the longer term, to use these data to more clearly delineate any relationships between the aluminum locations and the catalytic activities and selectivities of aluminosilicates.

Bibliography

- [1] Guisnet and Gilson *Zeolites for cleaner technologies*; Imperial College Press: London, 2002; Vol. 3.
- [2] Krishna, et al. *Chemical Society Reviews* **2002**, 31, 185.
- [3] Corma and Garcia. *Chemical Communications* **2004**, 1443.
- [4] van Bokhoven, et al. *Journal of Physical Chemistry B* **1999**, 103, 7557.
- [5] van Bokhoven, et al. *Journal of Catalysis* **2002**, 211, 540.
- [6] Engelhardt and Michel *High resolution solid state NMR of silicates and zeolites*; John Wiley & Sons: New York, 1987.
- [7] Ehresmann, et al. *Journal of the American Chemical Society* **2002**, 124, 10868.
- [8] Fyfe, et al. *Angewandte Chemie-International Edition in English* **1983**, 22, 259.
- [9] Joyner, et al. *Physical Chemistry Chemical Physics* **2004**, 6, 5435.
- [10] Brandle, et al. *Journal of Chemical Physics* **1998**, 109, 10379.
- [11] Eichler, et al. *Journal of Physical Chemistry B* **1997**, 101, 10035.
- [12] Beerdsen, et al. *J. Phys. Chem. B* **2002**, 106, 10659.
- [13] Beerdsen, et al. *Journal of Physical Chemistry B* **2003**, 107, 12088.
- [14] Takaishi, et al. *Zeolites* **1995**, 15, 21.
- [15] Peterson. *Journal of Physical Chemistry B* **1999**, 103, 3145.
- [16] Koranyi and Nagy. *Journal of Physical Chemistry B* **2005**, 109, 15791.
- [17] Herrero, et al. *Physical Review B* **1992**, 46, 787.
- [18] Vega. *Journal of Physical Chemistry* **1996**, 100, 833.
- [19] Bodart, et al. *Journal of Physical Chemistry* **1986**, 90, 5183.
- [20] Ding, et al. *Zeolites* **1995**, 15, 569.
- [21] Calero, et al. *Journal of Physical Chemistry B* **2006**, 110, 5838.
- [22] Calero, et al. *Journal of the American Chemical Society* **2004**, 126, 11377.
- [23] Baerlocher *Atlas of Zeolite Structure Types*, 5th ed.; Elsevier: London, 2001.
- [24] Shang-Shan, et al. *Chemical Physics Letters* **2005**, 408, 157.
- [25] Dubbeldam, et al. *Physical Review Letters* **2004**, 93.
- [26] Jaramillo and Auerbach. *Journal of Physical Chemistry B* **1999**, 103, 9589.
- [27] Dubbeldam, et al. *Journal of Chemical Physics* **2005**, 122.
- [28] Delgado, et al. Adsorption equilibrium of carbon dioxide, methane and nitrogen onto mordenite at high pressures. In *Molecular Sieves: From Basic Research to Industrial Applications, Pts a and B*, 2005; Vol. 158; pp 1065.
- [29] Macedonia, et al. *Langmuir* **2000**, 16, 3823.
- [30] Garcia-Perez, et al. *Applied Surface Science* **2005**, 252, 716.

- [31] Schelenker, et al. *Materials Research Bulletin* **1968**, 13, 169.
- [32] Meier. *Kristallogr.* **1978**, 147, 329.
- [33] Derouane. Proceedings of the 6th International Zeolite Conference, 1984, Reno.
- [34] Debras, et al. *Chemistry Letters* **1983**, 199.
- [35] Eder, et al. *J. Phys. Chem. B* **1997**, 101, 5414.
- [36] Ocakoglu, et al. *Journal of Physical Chemistry B* **2003**, 107, 398.

In our previous work, a computational method to characterize framework aluminum in aluminosilicates was proposed (García-Pérez, E., et al. *Angew. Chem., Int. Ed.* **2007**, 46, 276). In this work, the method was adopted to identify the most likely positions of aluminum in TON, FER, and MOR zeolites and to understand their different adsorption behaviors in detail. The simulations show that the location of aluminum affects the positions of the ions, and thus influences the adsorption. With the determined structures, the effects of non-framework ions on the adsorption behaviors of alkanes in these zeolites were studied systematically and the relations of the macroscopic adsorption behaviors of alkanes to their microscopic structures were elucidated. The results provided a better understanding of the influences of the position and density of aluminum on adsorption in zeolites from a microscopic level that may guide the future rational synthesis of new structures.



B. Liu, E. García-Pérez, D. Dubbeldam, B. Smit, and S. Calero

Understanding Aluminum Location and Non-Framework Ions Effects on Alkane Adsorption in Aluminosilicates: A Molecular Simulation Study

8.1 Introduction

Zeolites are microporous materials that have found wide applications as efficient heterogeneous catalysts and adsorbents in the petrochemical industry. In these materials the adsorption and diffusion of hydrocarbons in the zeolite pores play an important role[1,2]. The structure of zeolites is composed of silicon and aluminum oxide tetrahedra and charge-balancing ions. The presence of ions influences the adsorption properties of the zeolites. As the positions and stability of ions in the zeolites are strongly related to their Al distributions[3], it is therefore important to identify the aluminum site locations. Whereas it is relatively easy to determine the Si/Al ratio of the material, it is much more difficult to locate the exact positions of the aluminum atoms in the framework experimentally[4-9]. These difficulties motivate us to complement the experimental efforts with modeling and simulations.

H-TON, H-FER, and Na-MOR are structures used for industrial applications and many experimental investigations have been performed on the adsorption properties of these zeolites[10-30]. In these studies the positions of the aluminum atoms in these materials are not very clear, and the understanding of the effects of non-framework ions on the adsorption properties at the molecular level is yet incomplete. To date, all the simulations[31-39] about the adsorption properties of alkanes have been performed on the pure silica representation of TON and FER zeolites and only a limited simulations[26,40-42] on Na-MOR zeolites. In this work we perform a systematic study on these materials by molecular simulations to reveal the underlying mechanisms at a microscopic level.

The aluminum distribution on the crystal level, as well as the distribution on the level of a single unit cell, remains a subject of much debate and continued research efforts[43-49]. Macroscopically, the amount of aluminum might vary from the center of the crystal to the outer edges, while microscopically the Löwenstein rule, that is, two negatively charged Al atoms can never bond the same O atom, is well established. Our approach implicitly assumes a homogeneous aluminum distribution for the entire zeolite. To obtain some insights in the effect of variations of the amount of aluminum around an average value, we estimated the Henry coefficients of model materials in which some unit cells contain slightly less and others slightly more aluminum concentrations. These calculations agreed very well with those for a uniform aluminum distribution, giving us some confidence that we can compare our results with experimental samples.

The remainder of the paper is organized as follows. In section 8.2, we present the details of our simulation methodology, including descriptions of the zeolite models, the force fields, and the simulation technique used. In section 8.3, computed Henry coefficients, adsorption isotherms, and heats of adsorption for linear alkanes in several zeolite structures are given, and those in H-TON, H-FER, and Na-MOR zeolites are analyzed and discussed in detail. Finally, some concluding remarks are given in section 8.4.

8.2 Simulation models and methods

8.2.1 Zeolite models. The structures of zeolites considered in this work are well-known and have been used in many previous simulation studies. The pure silica structures were constructed by using the crystallographic coordinates reported[50] and the structures with aluminum were obtained by randomly replacing silicon by aluminum atoms, satisfying the Löwenstein rule.

Since TON, FER, and MOR zeolites were studied in detail in this work, their structures are shown in Figure 8.1, while the structures for the other zeolites considered can be

found easily in the literature[41,51-53]. The TON-type zeolite exhibits a unidirectional 10-ring pore system along the z -axis, with a pore aperture of 5 Å. The FER-type zeolite consists of straight 10-ring channels (5.4×4.2 Å) parallel to the z -axis which are interconnected by cages with 8-ring windows (4.8×3.5 Å) in the y -direction. The MOR-type zeolite has main channels parallel to [001], having a slightly elliptical cross section with 12 TO_4 tetrahedron units ($T = \text{Si}, \text{Al}$), which are connected with small side channels parallel to [010], with 8 TO_4 cross sections called side pockets. Four distinct T-sites aluminum can be located in them, shown in Figure 8.1 as T1, T2, T3, and T4. The zeolite lattices were assumed to be rigid in the simulations, because the flexibility of the framework has a negligible influence on the adsorption of alkanes[54].

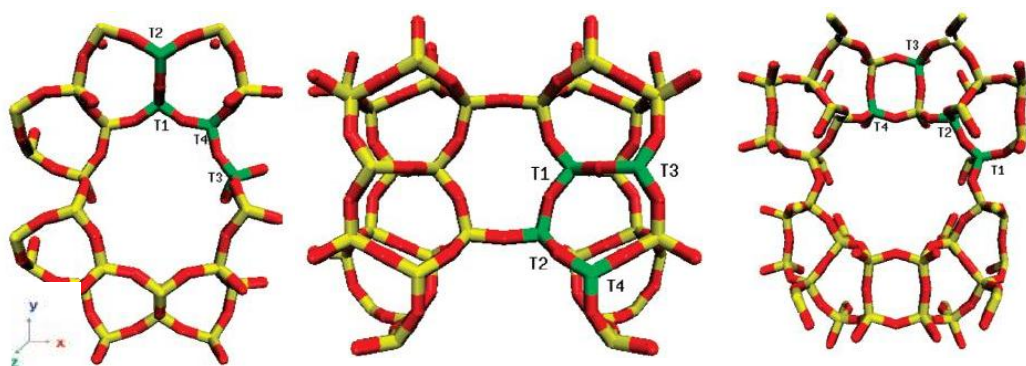


Figure 8.1 Representation of the model unit cell of (left) TON, (middle) FER, and (right) MOR with distinct T-sites where Al atoms can be located.

8.2.2 Force fields. Our simulations have been performed using a unique set of parameters defined by Dubbeldam et al. that accurately reproduce alkane–alkane and alkane–zeolite interactions in all silica structures[55,56]. Simulations in zeolites with aluminum in the framework require additional parameters for all interactions involving non-framework ions. Consequently the force fields recently proposed by Calero et al.[51,57] are used in this work for sodium cations and protons, both are the extended version of the force field of Dubbeldam et al.[55,56] to include the effects of sodium cations and protons. In these force fields the nature, density, and mobility of the non-framework ions, the density of the framework aluminum, and all host–guest interactions are carefully taken into account. The alkanes are described with a united atom model, in which CH_4 , CH_3 , and CH_2 groups are considered as single, charge-less interaction centers[58]. The beads in the chain are connected by harmonic bonding potentials. A harmonic cosine bending potential models the bond bending between three neighboring

beads, and a Ryckaert-Bellemans potential controls the torsional angle. The interactions between the adsorbates as well as the adsorbates and the zeolite are described by Lennard-Jones potentials and the interactions between the non-framework ions and the zeolite are modeled by Coulombic potentials. For a detailed description of the force fields, the reader is referred to refs [51,55-57].

8.2.3 Simulation technique. For the calculation of the Henry coefficients and the isosteric heats of adsorption at infinite dilution Q_{st}^0 , we performed Configurational-bias Monte Carlo (CBMC) simulations in the *NVT* ensemble. Each simulation consists of at least 4×10^7 steps, and in each cycle one move is chosen at random with a fixed probability 0.1 for a molecule translation, 0.1 for rotation around the center of mass, and 0.8 for regrowth of the entire molecule. During the simulation we compute the Rosenbluth factor and the internal energy ΔU , which are directly related to the Henry coefficients and the Q_{st}^0 [56,59].

Adsorption isotherms were calculated in the grand-canonical ensemble using the CBMC method. The CB-GCMC method simulates an open system specified by fixed temperature T , volume V , and fugacity f . We converted the imposed fugacity to the corresponding pressure using the Peng-Robinson equation of state. Four types of moves were carried out: translation, rotation, exchange of molecules between the zeolite and a molecule reservoir, and partial regrowth. All simulations included at least 2×10^7 steps. As the total number of ions is constant during simulations, only translation movements and regrowth at a random position in the zeolite are considered for these particles.

The statistical uncertainty was estimated by dividing each run into five blocks and calculating the standard deviation from the block averages. The standard deviation was within $\pm 10\%$ for every simulation. A detailed description of the simulation methods can be found in our previous work [51].

8.3 Results and discussion

8.3.1 Categorizing zeolites according to the sensitivity of adsorption properties to the aluminum distributions. In this work, we first categorized the commonly used zeolites (FAU, LTA, MEL, MFI, LTL, FER, MOR, and TON) into two groups according to the sensitivity of their adsorption properties to the aluminum distributions by computing the Henry coefficients of linear alkanes in them. In the simulations the Si/Al ratio is kept fixed by varying the aluminum distribution and using Na^+ and H^+ as non-framework ions. The results (see Supporting Information Figure 8.1) show that the adsorption properties of FAU, LTA, MEL, and MFI are insensitive to

aluminum distribution and they can be included in the insensitive group, while LTL, FER, TON, and MOR belong to the sensitive class. Therefore, the first group of zeolites can be used to accurately parameterize our simulation method[51,57], and for the second group of zeolites, their average aluminum distributions can be identified by matching the simulations with experiments using the parametrized simulation method[60].

8.3.2 Aluminum positions and alkane adsorptions in TON, FER, and MOR zeolites. We have performed molecular simulations to identify the aluminum positions in TON, FER, and MOR zeolites, as well as to provide a better molecular understanding of the alkane adsorption in them. For these zeolites, experimental adsorption data are available, and it is feasible to consider all possible aluminum distributions per unit cell: $H^+[AlSi_{23}O_{48}]$ -TON, $H^+[AlSi_{35}O_{72}]$ -FER (both with 4 possible aluminum distributions per unit cell), and $Na_8^+[Al_8Si_{40}O_{96}]$ -MOR (with 16 possible aluminum distributions per unit cell).

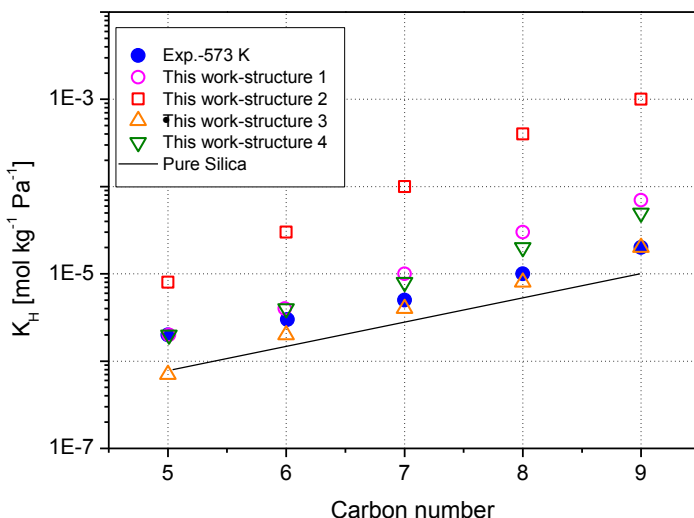


Figure 8.2 Comparison of the experimental[16] and simulated Henry coefficients of linear alkanes in H-TON zeolite at 573 K. Structures 1, 2, 3, and 4 indicate that the Al atom is located in T-site 1, 2, 3, and 4, respectively.

H-TON Zeolite. Figure 8.2 shows the calculated Henry coefficients of linear alkanes in H-TON zeolite at 573 K. The number of protons is kept one per unit cell to allow a direct comparison with experimental data. Since there are four distinct T-sites where aluminum

can be located and as the positions and stability of protons in the zeolite are strongly related to its Al distribution[3], four different structures were considered in this work, which correspond to the four T-sites. A comparison with the experimental values[16] indicates that most of the aluminum atoms on the zeolite sample are a combination of T3 and T4 substitutions for H-TON structures. Simulations at 473, 498, 523, and 548 K were also performed showing similar behavior (see ref [60] and Figure 8.2 in Supporting Information).

In order to clarify the differences among the structures, we examined the snapshots of these zeolites with adsorbed alkanes and those for hexane are shown in Figure 8.3. To illustrate the influences of protons on the adsorption, the results on pure silica structure are also shown for comparison. For pure silica structure, the hexane molecules adsorb homogeneously throughout the channels. In structures 1 and 4, protons were found located in the 10-ring channels partly. Protons take up adsorption volume in the channels where they are located but create additional preferred adsorption sites in the neighboring channels, which results in an increase of the adsorption comparing with the pure silica structure. As discussed in ref [57], the proton model necessarily assumes that there some traces of water in contact with the proton providing an effective adsorption volume that is significantly larger than one would expect from a single proton. We found that protons were all excluded from the 10-ring channels for structure 2, and they do increase the amount of adsorption in all 10-ring channels, leading to the highest adsorption capacity. The preferential location for proton in structure 3 is the 10-ring channels and the snapshot shows that protons occupy much volume in the channels, giving the lowest adsorption amount.

H-FER Zeolite. The adsorption behaviors of alkanes in H-FER zeolite were further investigated systematically. Figure 8.4 shows the calculated adsorption isotherms of propane at 333 K. Again the number of protons is kept one per unit cell and four different structures were considered corresponding to the four T-sites. Figure 8.4 shows that the calculated isotherms based on structure 3, that is, Al located on T3, agree very well with the experimental data. The adsorption isotherms of butane, pentane, and hexane show similar behavior (see ref [60] and Figure 8.3 in Supporting Information), illustrating that T3 structure is most likely the structure of the H-FER experimental sample. Heats of adsorption were also computed for this structure and comparison with experimental data[13] is provided in Table 8.1.

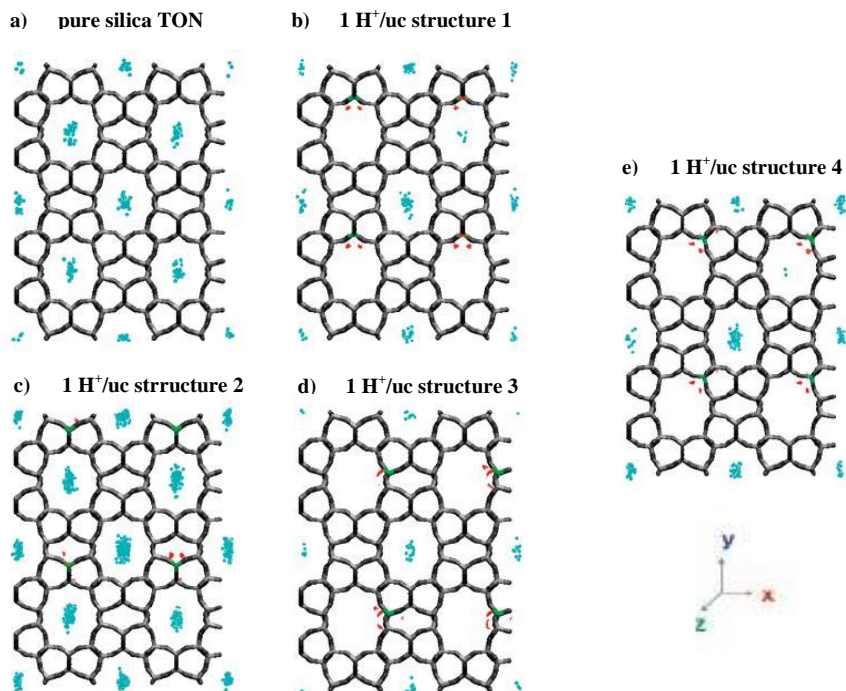


Figure 8.3 Distributions of hexane and the non-framework protons in TON zeolites at 5 kPa and 548 K. The centers of mass of the hexane molecules are represented by blue dots and the non-framework proton positions by red dots. The aluminum positions are indicated in green color.

Table 8.1 Comparison of the experimental and simulated heats of adsorption Q_{st}^0 [kJ mol⁻¹] of C₃-C₆ in H-FER zeolites.

	propane	<i>n</i> -butane	<i>n</i> -pentane	<i>n</i> -hexane
experimental data[13]	49	59	69	79
this work	48.43	57.14	67.72	81.90

The snapshots of the different structures with adsorbed alkanes were examined and those for butane are given, as an example, in Figure 8.5. The snapshots show that butane molecules are distributed over the channels and the cages for all structures considered. For pure silica structure, butane molecules are located almost homogeneously between the channels and the cages. For structure 1, proton was found located in the 8-ring cages

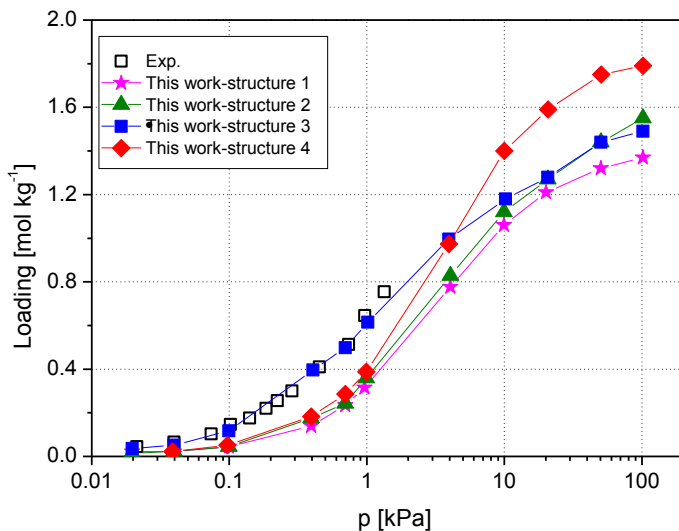


Figure 8.4 Comparison of the experimental[13] and simulated adsorption isotherms of propane in H-FER zeolite at 333 K. Structures 1, 2, 3, and 4 indicate that the Al atom is located in T-site 1, 2, 3, and 4, respectively

and butane molecules adsorbed preferentially in the 10-ring channels. Protons take up adsorption volume in the 8-ring cages but create additional preferred adsorption sites in the 10-ring channels, resulting in an increase of the adsorption. For structure 2, we found that the probability for protons located in the 8-ring cages and the 10-ring channels is almost the same, and from the snapshot, we can see that protons affect adsorption in a similar way as in structure 1, that is, decreasing the adsorption in the 8-ring cages but increasing it in the 10-ring channels. The preferential locations of protons in structure 3 are the 10-ring channels, which agrees well with the experimental analysis about the sample used in their work[13]. The protons occupy some volume in the 10-ring channels but the influence is not as big as in 8-ring cages. At low and intermediate loadings, they increase the amount of adsorption in both the 10-ring channels and the 8-ring cages, leading to the highest adsorption capacity. In structure 4, the preferential location for protons is the region across the 8-ring cages and the 10-ring channels, giving the lowest adsorption capacity. It seems that protons block the passageway to the 8-ring cages and the 10-ring channels.

The fractions of the adsorbed alkane molecules located in the FER 8-ring cages in structure 3 were calculated and the results are given in Figure 8.6 as a function of the loading. The ones on pure silica structure are also shown for comparison. Experimentally[17,18], it is found that propane adsorbs preferentially in the 8-ring cage. The adsorption of pentane initially takes place only in the 10-ring channel and adsorption

into the 8-ring cage occurs only at higher loadings. Hexane adsorbs only in the 10-ring channels and is excluded from the 8-ring cage. Our simulation results are consistent with the experimental observations. For butane, no preference is found by NMR measurements and our simulations predict that butane adsorption is preferred in the 10-ring channels for pure silica structure and in the 8-ring cage for H-FER structure. This can be explained by examining the snapshots of butane adsorption at low pressures. Figure 8.7 shows the sitting of butane in FER zeolites at 333 K and 0.05 kPa. For pure silica structure butane preferentially adsorbs in the 10-ring channels. Once we put any small amount inside the channels, they will start to repel *n*-alkanes attributed to the fact that the channel of FER-type zeolites is the smallest channel not to repel *n*-alkanes comparing with other zeolites[61]. When *n*-alkanes cannot reside in the 10-ring channel they will head for the 8-ring cage.

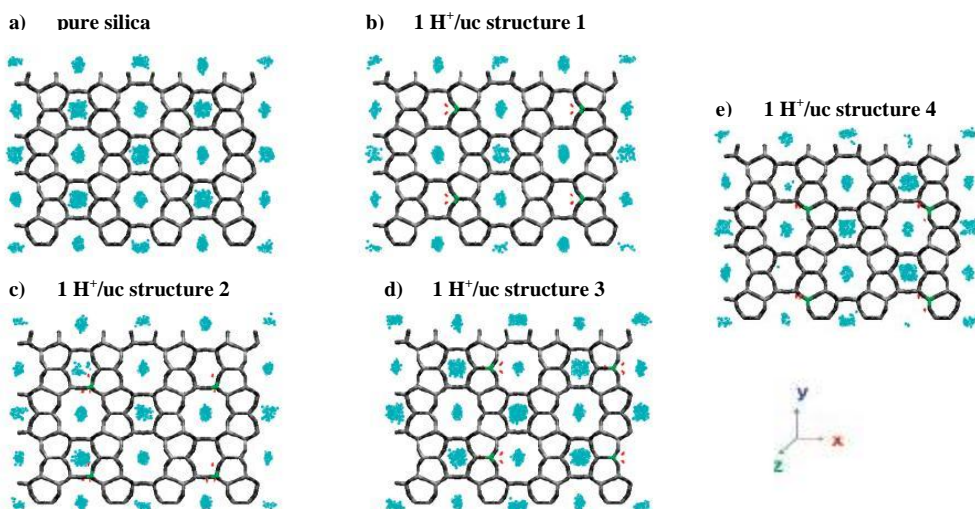


Figure 8.5 Distributions of butane and the non-framework protons in FER zeolites at 0.4 kPa and 333 K. The centers of mass of the butane molecules are represented by blue dots and the non-framework proton positions by red dots. The aluminum positions are indicated in green color.

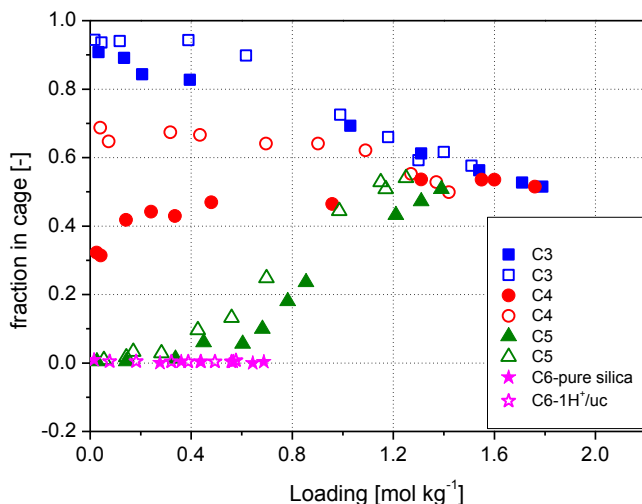


Figure 8.6 Fraction of the adsorbed alkane molecules located in the FER 8-ring cages as a function of loading at 333 K. The results for pure silica structure are represented by full symbols and the ones for H-FER are represented by open symbols.

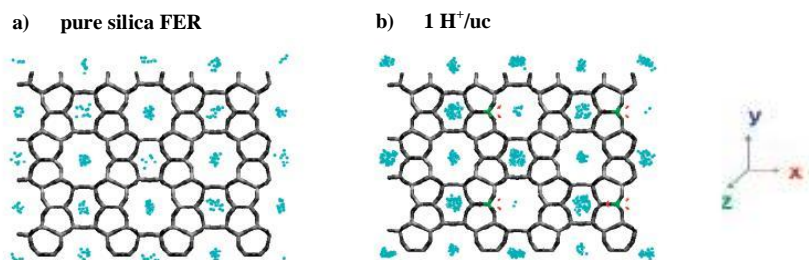


Figure 8.7 Distributions of butane and the non-framework protons in FER zeolites at 0.05 kPa and 333 K. The centers of mass of the butane molecules are represented by blue dots and the non-framework proton positions by red dots. The aluminum positions are indicated in green color.

Na-MOR Zeolite. Another important zeolite considered in this work is Na-MOR zeolite. The adsorption isotherms and the Henry coefficients of methane in sixteen different structures were calculated and compared with available experimental data[26,30]. Our results show that the agreement with experimental values is remarkable for the structure where Al atoms replace Si 4, 18, 31, 42, 80, 93, 105, and 115[60]. In this structure the eight Al atoms are located in the 4-rings, in complete conformity with the suggested preferential sitting of aluminum provided by previous crystallographic, experimental, and theoretical work[43,44,62-65]. To study the effects of the cations on the adsorption behavior, we checked the snapshot of this structure with adsorbed methane at 323 K and

1 kPa, and compared with the adsorption in pure silica structure. The results are shown in Figure 8.8. For pure silica structure, the methane molecules are located almost homogeneously between the main channels and the side pockets. However, for the structure with cations, methane molecules were found adsorbed preferentially in the side pockets. Nearly half of the sodium cations were found to reside in the center of the 8-membered oxygen rings outside the main channels[66,67]. This agrees with the available experimental data[68]. Furthermore, the fraction of the adsorbed methane molecules located in the MOR main channels in the sodium and the pure silica structures was also calculated and the results are given in Figure 8.9 as a function of the loading. For pure silica structure, it is found that the side pockets are favored but not very strongly because the side pocket adsorption sites have a lower energy[26,69] and the percentage is almost constant with the increasing of the loading. For Na-MOR structure, side pocket adsorption becomes more favorable because the Na cations residing at the opening of the side pockets make these sites more attractive[26]. These results are in complete conformity with the snapshots shown in Figure 8.8 and with all previous results[26,69], but those obtained by Smit and den Ouden[40]. Smit and den Ouden predicted exclusion of methane from the side pockets in Na-MOR structure considering that the side pockets were effectively blocked by the Na cations, and unlike in our work, they fixed the Na cations throughout their simulation.

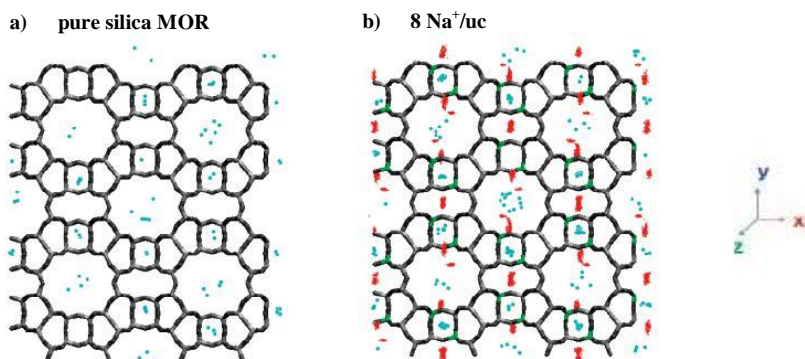


Figure 8.8 Distributions of methane and the non-framework sodium cations in MOR zeolites at 1 kPa and 323 K. The methane molecules are represented by blue dots and the non-framework Na⁺ positions by red dots. The aluminum positions are indicated in green color.

Our simulation results show that by matching the simulation data with the available experimental values the most likely position of aluminum in zeolites could be identified.

The aluminum position determines the cation distribution, and it is the presence and positions of the cations that can cause a difference in adsorption behavior. The Henry coefficients for FAU and LTA increase dramatically by the presence of cations, up to orders of magnitude for the longer chain lengths. As previously noted in literature, the effects of ions are 3-fold:[41,42,51] (a) ions provide additional adsorption sites, (b) ions occupy pore volume, and (c) ions can block accessible pockets and windows. FAU and LTA are examples of the first, while the second effect is here reduced because ions are allowed to occupy pore volume (the sodalite cages) that is not accessible to the bulkier alkanes. This volume effect is important in zeolites formed by channels, like MFI and MOR, and at high pressures where loadings are close to saturation. MOR is also sensitive to the third effect, showing side pockets that can be blocked[41]. In some zeolites which have very different adsorption “regions”, other complications can occur. Examples include MFI, which has straight channels, zigzag channels, and intersections, and FER which has 10-ring channels and 8-ring side cages. Typically, for many adsorbates, this shows up as inflection in the adsorption isotherms[55,70-72] and/or in Henry coefficients over chain length (see Figure 8.1f in Supporting Information). One of the main goals of this work is to find systematic trends in this and hopefully a classification or at least some criteria to estimate the influence of ions.

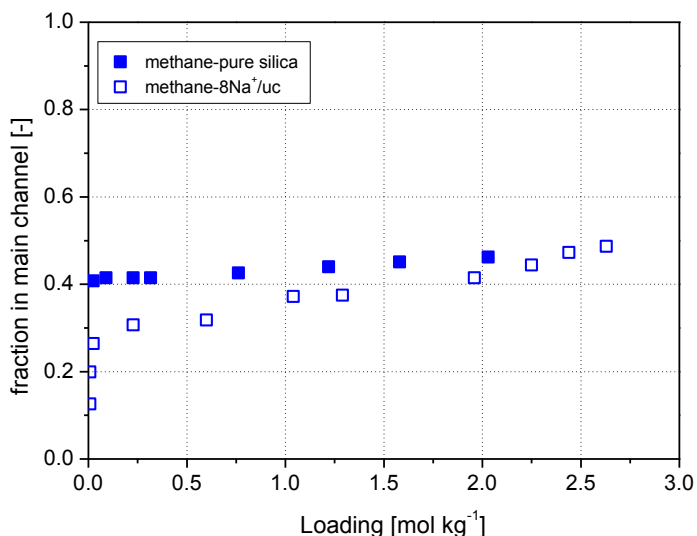


Figure 8.9 Fraction of the adsorbed methane located in the MOR main channels as a function of loading at 323 K. The results for pure silica structure are represented by full symbols, and the ones for Na-MOR are represented by open symbols.

For the adsorption of alkanes we found that FAU, LTA, MEL, and MFI are insensitive to the aluminum distribution, while LTL, FER, TON, and MOR belong to the sensitive

class. The insensitivity of the first group originates either from large, spherical cages with a high degree of symmetry (LTA and FAU), or from structures (MEL and MFI) that have preferred aluminum positions at different locations than the alkane adsorption sites. In MFI the preferred aluminum positions are in the big intersection, while alkanes prefer the straight channels at low loadings. LTA and FAU show a higher difference with the pure siliceous structure than MEL and MFI, mainly due to the larger amount of ions per volume present in these structures (see Figures 8.1a-8.1d in Supporting Information). The increase per carbon number is the same for MEL and MFI, but for FAU and LTA, we clearly find a change in slope. In cage type zeolites multiple beads of the molecule have interaction with the ions. MFI and MEL have channels that tightly confine the alkanes and only the ends of the alkanes feel the ions resulting in a constant shift of the Henry coefficients as a function of carbon number. The zeolites of second group are channel systems and seem very sensitive to the positions of the aluminum, especially at low loadings. Fortunately, this is the general case. We suspect that MFI and MEL could be sensitive to other adsorbates than alkanes. This means that FAU and LTA (big cages with high degree of symmetry) are ideal to calibrate potential parameters (as we previously did[51,73]), while almost all other structures are then suitable for the “reverse engineering.”[60]

We are aware that our comparisons are subject to several uncertainties as well as to the experimental and simulation errors. However, in our opinion the approach itself remains valid and very attractive as simulations and experiments advances in time. We note that the fitting procedures with the set of structures which are insensitive to the aluminum distribution are based on the same kind of experimental data and procedures. Our potentials might therefore effectively already contain a certain level of experimental error, although these of course might vary from zeolite to zeolite, and sample to sample. However, it is the best we could do using currently available experimental data, and as soon as more experimental data becomes available we can further refine our approach.

8.4 Conclusions

The simulation results provided a better physical understanding of the effects of the aluminum distributions on the adsorption properties of alkanes in zeolites at a microscopic level. This work shows that the aluminum distributions in zeolites strongly affect the positions and stability of ions, which in turn influence the adsorption behavior of alkanes. Therefore, the effect of aluminum on adsorption is indirect, and it depends on

the adsorbent, the ion, and the adsorbate type whether or not the adsorption is influenced. Furthermore, it should be possible, in the longer term, to use these data to more clearly delineate the relationships between the aluminum locations and the catalytic activities and selectivities of aluminosilicates.

Bibliography

- [1] Krishna, et al. *Chemical Society Reviews* **2002**, 31, 185.
- [2] Smit and Krishna. *Chemical Engineering Science* **2003**, 58, 557.
- [3] Buttefey, et al. *J. Phys. Chem. B* **2001**, 105, 9569.
- [4] van Bokhoven, et al. *Journal of Physical Chemistry B* **1999**, 103, 7557.
- [5] van Bokhoven, et al. *Journal of Catalysis* **2002**, 211, 540.
- [6] Engelhardt and Michel *High resolution solid state NMR of silicates and zeolites*; John Wiley & Sons: New York, 1987.
- [7] Ehresmann, et al. *Journal of the American Chemical Society* **2002**, 124, 10868.
- [8] Fyfe, et al. *Angewandte Chemie-International Edition in English* **1983**, 22, 259.
- [9] Joyner, et al. *Physical Chemistry Chemical Physics* **2004**, 6, 5435.
- [10] Denayer, et al. *J. Phys. Chem. B* **1998**, 102, 4588.
- [11] Denayer, et al. *Chemical Engineering Science* **1999**, 54, 3553.
- [12] Savitz, et al. *J. Phys. Chem. B* **1998**, 102, 6865.
- [13] Eder and Lercher. *J. Phys. Chem. B* **1997**, 101, 1273.
- [14] Pieterse, et al. *Journal of Physical Chemistry B* **2000**, 104, 5715.
- [15] Yang, et al. *J. Phys. Chem. B* **2001**, 105, 1935.
- [16] Ocakoglu, et al. *Journal of Physical Chemistry B* **2003**, 107, 398.
- [17] van Well, et al. *J. Phys. Chem. B* **1998**, 102, 3945.
- [18] van Well, et al. *Angewandte Chemie-International Edition* **1998**, 37, 1081.
- [19] Satterfield and Frabetti. *Aiche Journal* **1967**, 13, 731.
- [20] Choudhary, et al. *Journal of the Chemical Society-Faraday Transactions* **1995**, 91, 2935.
- [21] Eberly. *Journal of Physical Chemistry* **1963**, 67, 2404.
- [22] Xu, et al. *Journal of the Chemical Society-Faraday Transactions* **1995**, 91, 2949.
- [23] Xu, et al. *Journal of the Chemical Society-Faraday Transactions* **1996**, 92, 1039.
- [24] Denayer, et al. *J. Phys. Chem. B* **1998**, 102, 3077.
- [25] Webster, et al. *Journal of the American Chemical Society* **1999**, 121, 12127.
- [26] Macedonia, et al. *Langmuir* **2000**, 16, 3823.
- [27] Yamazaki, et al. *Physical Chemistry Chemical Physics* **2001**, 3, 2686.
- [28] Yuvaraj, et al. *Journal of Physical Chemistry B* **2003**, 107, 4971.
- [29] Salla, et al. *Journal of Physical Chemistry B* **2005**, 109, 915.

- [30] Delgado, et al. Adsorption equilibrium of carbon dioxide, methane and nitrogen onto mordenite at high pressures. In *Molecular Sieves: From Basic Research to Industrial Applications, Pts a and B*, 2005; Vol. 158; pp 1065.
- [31] Maesen, et al. *Journal of Catalysis* **1999**, 188, 403.
- [32] Schenk, et al. *Angewandte Chemie-International Edition* **2001**, 40, 736.
- [33] Domokos, et al. *Journal of Catalysis* **2001**, 203, 351.
- [34] Raybaud, et al. *Journal of Catalysis* **2001**, 197, 98.
- [35] Lu, et al. *Acta Chimica Sinica* **2003**, 61, 1232.
- [36] Ndjaka, et al. *Microporous and Mesoporous Materials* **2004**, 68, 37.
- [37] van Well, et al. *J. Phys. Chem. B* **1998**, 102, 3952.
- [38] Pascual and Boutin. *Physical Chemistry Chemical Physics* **2004**, 6, 2015.
- [39] Pascual, et al. *Molecular Simulation* **2004**, 30, 593.
- [40] Smit and den Ouden. *J. Phys. Chem.* **1988**, 92, 7169.
- [41] Beerdsen, et al. *J. Phys. Chem. B* **2002**, 106, 10659.
- [42] Liu and Smit. *Physical Chemistry Chemical Physics* **2006**, 8, 1852.
- [43] Koranyi and Nagy. *Journal of Physical Chemistry B* **2005**, 109, 15791.
- [44] Bodart, et al. *Journal of Physical Chemistry* **1986**, 90, 5183.
- [45] Takaishi, et al. *Zeolites* **1995**, 15, 21.
- [46] Peterson. *Journal of Physical Chemistry B* **1999**, 103, 3145.
- [47] Herrero, et al. *Physical Review B* **1992**, 46, 787.
- [48] Vega. *Journal of Physical Chemistry* **1996**, 100, 833.
- [49] Ding, et al. *Zeolites* **1995**, 15, 569.
- [50] International Zeolite Association. Structure Commission, <http://www.iza-structure.org>.
- [51] Calero, et al. *Journal of the American Chemical Society* **2004**, 126, 11377.
- [52] Maesen, et al. *Journal of Catalysis* **2001**, 203, 281.
- [53] Dubbeldam, et al. *Journal of Chemical Physics* **2005**, 122.
- [54] Vlugt and Schenk. *J. Phys. Chem. B* **2002**, 106, 12757.
- [55] Dubbeldam, et al. *Physical Review Letters* **2004**, 93.
- [56] Dubbeldam, et al. *Journal of Physical Chemistry B* **2004**, 108, 12301.
- [57] Calero, et al. *Journal of Physical Chemistry B* **2006**, 110, 5838.
- [58] Ryckaert and Belleman. *Faraday Discussions* **1978**, 95.
- [59] Frenkel and Smit *Understanding Molecular Simulations: From Algorithms to Applications*, second edition ed.; Academic Press: San Diego, CA, 2002.
- [60] Garcia-Perez, et al. *Angewandte Chemie-International Edition* **2007**, 46, 276.
- [61] Maesen, et al. *Journal of Catalysis* **2006**, 237, 278.
- [62] Schelenker, et al. *Materials Research Bulletin* **1968**, 13, 169.

- [63] Meier. *Kristallogr.* **1978**, 147, 329.
- [64] Derouane. Proceedings of the 6th International Zeolite Conference, 1984, Reno.
- [65] Debras, et al. *Chemistry Letters* **1983**, 199.
- [66] Maurin, et al. *Journal of Physical Chemistry B* **2001**, 105, 9157.
- [67] Maurin, et al. *Journal of Physical Chemistry B* **2004**, 108, 3739.
- [68] Meier. *Kristallogr.* **1961**, 115, 439.
- [69] Nivarthi, et al. *Journal of Chemical Physics* **1995**, 103, 3029.
- [70] Smit and Maesen. *Nature* **1995**, 374, 42.
- [71] Vlugt, et al. *J. Am. Chem. Soc.* **1998**, 120, 5599.
- [72] Vlugt, et al. *J. Phys. Chem. B* **1999**, 103, 1102.
- [73] Garcia-Perez, et al. *Journal of Physical Chemistry B* **2006**, 110, 23968.

The adsorption of several quadrupolar and non-polar gases on the Metal Organic Framework Cu-BTC has been studied by combining experimental measurements and Monte Carlo simulations. Four main adsorption sites for this structure have been identified: site I close to the copper atoms, site I' in the bigger cavities, site II located in the small octahedral cages, and site III at the windows of the four open faces of the octahedral cage. Our simulations identify the octahedral cages (sites II and III) and the big cages (site I') as the preferred positions for adsorption, while site I, near the copper atoms, remains empty over the entire range of pressures analyzed due to its reduced accessibility. The occupation of the different sites for ethane and propane in Cu-BTC proceeds similarly as for methane, and shows small differences for O₂ and N₂ that can be attributed to the quadrupole moment of these molecules. Site II is filled predominantly for methane (the non-polar molecule) whereas for N₂, the occupation of II and I' can be considered almost equivalent. The molecular sitting for O₂ shows an intermediate behavior between those observed for methane and for N₂. The differences between simulated and experimental data at elevated temperatures for propane are tentatively attributed to a reversible change in the lattice parameters of Cu-BTC by dehydration and by temperature, blocking the accessibility to site III and reducing that to site I'. Adsorption parameters of the investigated molecules have been determined from the simulations.



E. García-Pérez, J. Gascón, V. Morales-Flórez, J.M. Castillo, F. Kapteijn, and S. Calero

Identification of Adsorption Sites in Cu-BTC by Experimentation and Molecular Simulation

9.1 Introduction

Metal Organic Frameworks (MOFs) have become a novel field of research, resulting in numerous publications during the recent years[1]. MOFs are crystalline nanoporous materials that consist of small metal-containing clusters connected three dimensionally by organic ligands. The ligands act as spacers, creating an open porous structure with very high pore volume and surface area. Due to their unusual variety in terms of chemical composition, accessibility, and pore dimensions, MOFs are considered as promising candidates to address the current hurdles in gas storage, adsorption separations, and catalysis[2].

Among the many known MOFs, copper benzene tricarboxylate ($\text{Cu}_3(\text{BTC})_2$ or Cu-BTC) is one of the best characterized structures[3] together with the IRMOF series[4,5]. It was first reported in 1999 and named HKUST-1[6]. This electrically neutral framework is composed of dimeric cupric tricarboxylate units with a short Cu–Cu internuclear separation. Each metal completes its pseudo-octahedral coordination sphere with an axial water ligand opposite to the Cu–Cu vector[3]. After removing water from the framework, it becomes an open three dimensional porous structure with main channels of a square cross-section of about 9 Å diameter and tetrahedral side pockets of about 5 Å, which are connected to the main channels by triangular windows of about 3.5 Å in diameter. It is commonly synthesized under mild hydrothermal conditions (383 K – 393 K), although it has also been electrochemically synthesized[2]. $\text{Cu}_3(\text{BTC})_2$ shows a great potential for gas purification, separation[7], storage[8], and it could be also suitable for catalytic purposes due to its high Lewis acidity[9,10].

Despite the increasing amount of publications dealing with the synthesis of new MOFs, much less effort has been devoted to a better understanding of the interactions MOF–guest molecules[11-15]. Regarding Cu-BTC, Krungleviciute et al. analyzed the adsorption and kinetics of argon and carbon tetrafluoride providing experimental evidence that the former enter the octahedral cages of Cu-BTC but not the latter[16,17]. Vishnyakov et al.[18] constructed the first molecular structural model and made a first description of the preferential adsorption sites for the adsorption of Ar at low temperatures, defining the sequence of adsorption as a gradual filling of the side pockets to a stepwise adsorption and condensation in the main channels. Further molecular modeling using grand canonical Monte Carlo (GCMC) and different force fields has been reported focusing mainly on small gas molecules (Ar, H_2 , CH_4 , and CO_2)[19-24]. However, a good agreement between experimental and simulated isotherms has not been obtained so far. This is likely due to experimental and simulation problems. As reviewed very recently[23], adsorption results from different groups vary significantly due to crystal defects, the presence of guest molecules or just because of differences in the methods and adsorption equipment used[2,6,23,25].

The two main types of cavities in Cu-BTC make this structure a potentially good material not only for molecular adsorption but also for separations of gas mixtures. Therefore, it is vital to properly understand the underlying mechanisms of adsorption in this material. We analyze here the adsorption of several molecules on Cu-BTC, determining the preferential adsorption sites in all cases. The interactions between the metal organic framework and quadrupolar and non-polar gases have been studied by combining experimental results and grand canonical Monte Carlo simulations. High quality samples were synthesized and adsorption isotherms for methane, ethane, propane, nitrogen, and

oxygen were determined. They were reconciled with isotherms calculated using simulation techniques previously used by our group[26-28]. The comparison is used to analyze preferential adsorption sites for the different adsorbates as a function of pressure and coverage. To identify the main adsorption sites for this structure a similar procedure as the one reported by Liu et al.[29] is followed.

9.2 Experimental

Copper (II) nitrate hydrate ($\text{Cu}(\text{NO}_3)_2 \cdot 3\text{H}_2\text{O}$) and 1,3,5-benzenetricarboxylic acid (trimesic acid) purchased from Aldrich, were used as received, without further purification.

$\text{Cu}_3(\text{BTC})_2$ crystals were prepared by the method described elsewhere[9], 0.875 g (3.6 mmol) $\text{Cu}(\text{NO}_3)_2 \cdot 3\text{H}_2\text{O}$ are dissolved in 12 ml deionized water (solution A) and mixed with 0.42 g (2.0 mmol) of trimesic acid dissolved in 12 ml ethanol (solution B). The resulting solution (A + B) is stirred for 30 minutes, placed in an autoclave and heated under hydrothermal conditions (autogenous pressure) to 383 for 18 h. For entropic reasons, synthesis at a higher temperature can promote the loss of terminal ancillary ligands, while synthesis at lower temperatures would need much longer synthesis times to yield crystalline products[6].

A Micromeritics ASAP 2010 gas adsorption analyzer (stainless steel version) was used to measure the adsorption isotherms. Prior to the gas-adsorption measurements, the samples were treated under vacuum at 423 K overnight in order to remove present solvents, moisture, and other volatile components.

The crystalline materials were analyzed by X-ray diffraction (XRD) using a Bruker-AXS D5005 with Cu $K\alpha$ radiation using internal (LaB6) standard. After correcting for sample displacement by using the calibrated positions of the LaB6, peak positions are accurately known within $0.01^\circ 2\theta$. Temperature Programmed XRD (TP-XRD) was performed under dry N_2 atmosphere using temperature ramps of 1 K/min. The experimental procedure was as follows: one sample hydrated (as synthesized) was introduced in the sample cell and XRD was measured at room temperature. The sample was dehydrated by increasing the temperature under N_2 flow (100 ml/min) up to 473 K overnight. Afterward, the temperature was reduced using the same ramp and XRD analyses of the dehydrated sample were collected at 473, 373 K, and room temperature.

9.3 Simulation method and models

The computed adsorption isotherms were obtained from Grand Canonical Monte Carlo (GCMC) simulations, where the chemical potential, the temperature, and the volume are fixed. Pressure is transformed into fugacity using the Peng-Robinson equation of state, and fugacity can be directly related to the imposed chemical potential[30]. The Henry coefficients, energies, enthalpies, and entropies of adsorption were computed using MC in the NVT ensemble at 295 K. We grow test chains during the simulation using the Rosenbluth weight of the adsorbate. Detailed information about this method can be found elsewhere[31]. The MC moves were performed in cycles and in each cycle one move was chosen at random with a fixed probability of translation, rotation, and regrowth in a random position. We used at least 10^7 cycles and charge interactions were computed using Ewald sums with a relative precision of 10^{-6} . The Lennard-Jones potential is cut and shifted with the cutoff distance set to 12 Å.

Cu-BTC is composed of benzene-1,3,5-tricarboxylate (BTC) ligands coordinating copper ions, forming big cavities and small octahedral cages. The symmetry of the Cu-BTC unit cell is cubic. This unit cell is formed by six side cages of octahedral shape (not symmetry) located at the vertices of the unit cell, and linked by the metal centers. The octahedral structures are formed by BTC molecules placed in alternate faces. The rest of the faces are free of molecules, forming windows that allow the access to these side cages. Therefore, in the center of the unit cell lays a nearly spherical void space of 9 Å of diameter. Adsorption sites on this metal organic framework were selected as explained by Liu et al.[29] for H₂ adsorption.

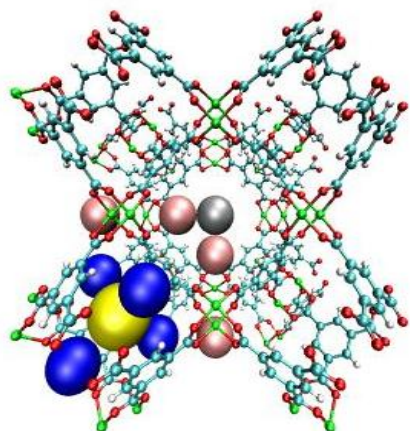


Figure 9.1 Preferential adsorption sites in Cu-BTC labeled I, I', II, and III. Color spheres illustrate the positions of the different sites. Site I, region close to the Cu atoms of the framework (pink spheres); site II, center of the octahedral side pockets (yellow sphere); site III, windows of the octahedral side pockets (blue spheres); and site I', center of the big Cu-BTC cages (gray sphere).

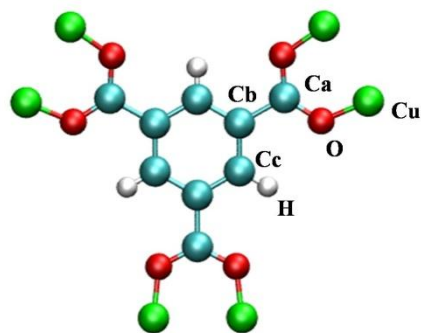


Figure 9.2 The crystallographically different atoms used to define the Cu-BTC structure are labeled; the other labels follow by symmetry.

We started this research considering those sites that can be briefly explained as follows: type I sites—48 per unit cell—were considered at the copper atoms of the structure, type II sites—8 per unit cell—were assigned to the center of the octahedral cages, and type III sites—8 per unit cell—were located at the windows of the four open faces of the octahedral cage. In addition to these sites defined by Liu et al., we also considered the type I'—4 per unit cell—adsorption site located in the big central cavities. The cutoff radius of site II is chosen as 0.2 nm and site III as the spherical annulus between radii 0.2 and 0.55 nm. The cutoff radius of site I is chosen as 0.3 nm removing the intersection with site III, and finally we defined site I' as the rest of the volume not contained in the previous sites. In this way, every coordinate within the unit cell was assigned to one single site. The Cu-BTC structure with the defined adsorption sites is shown in Figures 9.1 and 9.2.

The use of rigid frameworks has been proven to be accurate enough when studying adsorption of small molecules in zeolites at room temperature and in MOFs that are reasonably rigid[32-34]. There are various force fields available for rigid structures that

reproduce well adsorption isotherms in MOFs by using a different parameter set depending on the adsorbed molecule[22,35,36]. In this work, Cu-BTC is modeled as a rigid structure with Lennard-Jones parameters taken from DREIDING force field[35], except those for Cu that were taken from the UFF[36] force field. Atomic charges were taken from Frost and Snurr[37] and Lorentz-Berthelot mixing rules were used to calculate mixed Lennard-Jones parameters. One unit cell of Cu-BTC ($a = b = c = 26.343 \text{ \AA}$) was used in our simulations. The unit cell contains 624 atoms of which 48 are copper, 192 oxygen, 96 hydrogen, and 288 carbon (these latter classified in three groups depending on the atoms next to them, *Ca*: next to two oxygen atoms, *Cb*: between three carbons, and *Cc*: linked to one hydrogen). We obtained a helium void fraction of 0.76. This adsorption study is performed on a dehydrated Cu-BTC. Although it is well-known that the dehydration process causes a reduction of the cell volume due to the shrinking of the octahedral cages and preserves the crystalline nature of the material[3], the dehydrated crystal structure is not available in the literature. Therefore, we adopted the dehydrated form by removing the water oxygen atoms weakly bonded to the Cu atoms from the crystal structure of Chui et al.[6] The interactions between guest molecules (alkanes, N_2 , and O_2) with the Cu-BTC host framework are modeled by Lennard-Jones and Coulombic potentials. The Coulomb interactions in the system are calculated with Ewald summations. The alkanes (methane, ethane, and propane) are described with a united atom model[38], in which CH_x groups are considered as a single, chargeless interaction centers with their own effective potentials. The beads in the chain are connected by harmonic bonding potentials $U = 0.5 k (r - r_0)^2$ with $k/k_B = 96\,500 \text{ K/\AA}^2$ and $r_0 = 1.54 \text{ \AA}$. The bond bending between three neighboring beads is modeled by a harmonic cosine bending potential $U = 0.5 k (\theta - \theta_0)^2$ with $k/k_B = 62\,500 \text{ K}$ and $\theta_0 = 114^\circ$. N_2 and O_2 were considered as small rigid molecules, using the model proposed by Murthy et al.[39] for N_2 and the model proposed by Mellot and Lignieres[40] for O_2 . The partial charges of N_2 and O_2 were distributed over each molecule to reproduce experimental quadrupole moment. These models and potentials have been successfully employed to describe the adsorption in zeolites[26,28,41,42]. Table 9.1 collects the charges and intermolecular parameters used in this work.

Absolute adsorption was converted to excess adsorption for comparison with the experimental data[43,44]. The method used for the analysis of the preferential adsorption sites in Cu-BTC is similar to that used in our previous work on the locations and occupancies of ions in zeolites[45,46].

Table 9.1 Partial charges and Lennard–Jones parameters for the structure and the adsorbed molecules used in this work.

Cu-BTC				adsorbed molecules			
atom type	ε/k_B [K]	σ [Å]	charge [e^-]	atom type	ε/k_B [K]	σ [Å]	charge [e^-]
Cu	2.518	3.114	1.0	CH ₄	158.5	3.72	
O	48.19	3.03	-0.6	CH ₃	108.0	3.76	
Ca	47.86	3.47	0.7	CH ₂	56.0	3.96	
Cb	47.86	3.47	0.0	N (N ₂)	36.4	3.32	-0.40484
Cc	47.86	3.47	-0.15	dummy (N ₂)			0.80968
H	7.65	2.85	0.15	O (O ₂)	44.5	3.09	-0.112
				dummy (O ₂)			0.224

9.4 Results and discussion

Adsorption of N₂ at 77 K was obtained experimentally and by molecular simulations. Experimental results reveal a type I isotherm with no hysteresis loop. A surface area of 1366 m²/g, a micropore volume of 0.55 cm³/g and an external area of 30 m²/g were calculated from the N₂ adsorption isotherm at 77 K. As reviewed very recently, these values are similar as the best reported specific surface areas reported for this material[23]. Our molecular simulations overestimate the maximum amount of nitrogen adsorbed since they were performed in a perfect and hydrated crystal, without defects and where all pores are fully accessible. Therefore, differences between the experimental and simulated values can be attributed to small defects and residual solvent, guest molecules or nitrates after synthesis. Figure 9.3 compares the obtained adsorption isotherms at 77 K and shows that the ratio of the measured and simulated saturation loadings is 0.8 over the whole pressure range. Previous experimental data in this range of pressures were included for comparison[47]. The scaling factor provides a good measure of how much of the theoretical pore volume is accessible in the material used in the experiments[33,48]. Although it is possible to establish direct comparison between the experimental and the scaled simulation data, the exact position of the defects and remaining molecules after synthesis cannot be identified. The two-step isotherm is also reproduced, although the level of the first step is lower than experimentally reported[47]. If we analyze the low pressure sorption data, then the reported results point to a transient phenomenon, causing a hysteresis in the isotherm. Either activated diffusion and a too slow uptake interfered or, due to the nitrogen sorption slight changes, induced in the structure alleviated this diffusional resistance.

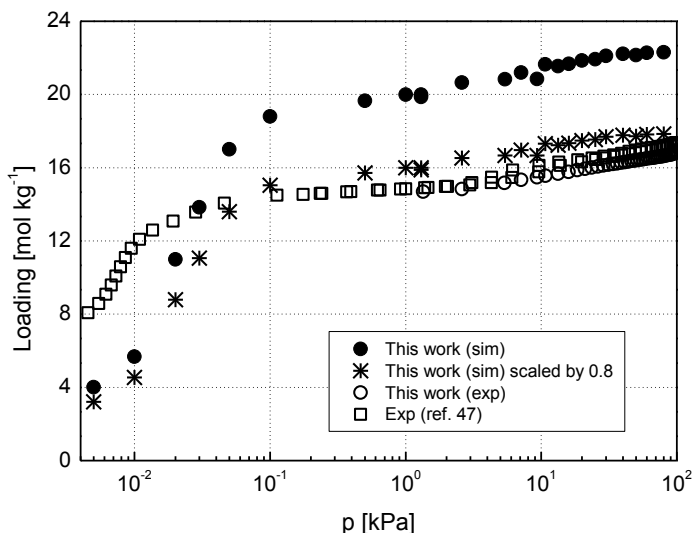


Figure 9.3 Comparison of simulated and experimental N_2 adsorption isotherms in Cu-BTC at 77 K. Our experimental and simulation results are represented by open and filled circles, respectively. Scaled simulation data are represented by stars and previous experimental data[47] (squares) are included for comparison.

Molecular simulations also reproduce the experimental data for N_2 at higher temperatures. The agreement between the experimental and scaled isotherms obtained from simulations at 295 K is shown in Figure 9.4, providing detailed information about the molecular sitting. The occupation of the preferential adsorption sites as a function of pressure is included in Figure 9.4 before applying the scaling factor. Note that at high temperatures and at the experimental pressures considered in this work, saturation is far from reached and therefore scaling is not as relevant as it was at 77 K. Analysis of the occupancies of the individual adsorption sites from the nonscaled simulation data indicates that N_2 adsorbs preferentially in the octahedral cages (site II) and in the big cages (site I'). The windows of the octahedral cages are also occupied (site III) but to a lower extent. Site I, near the copper atoms, remains empty over the entire range of pressures analyzed in this work. This is consistent with the literature, since although the Cu(II) cations in principle should become available after dehydration, they show a rather low coordinative unsaturation[3] due to a change in position in the structure. The unit cell size also reduces[3] (*vide infra*).

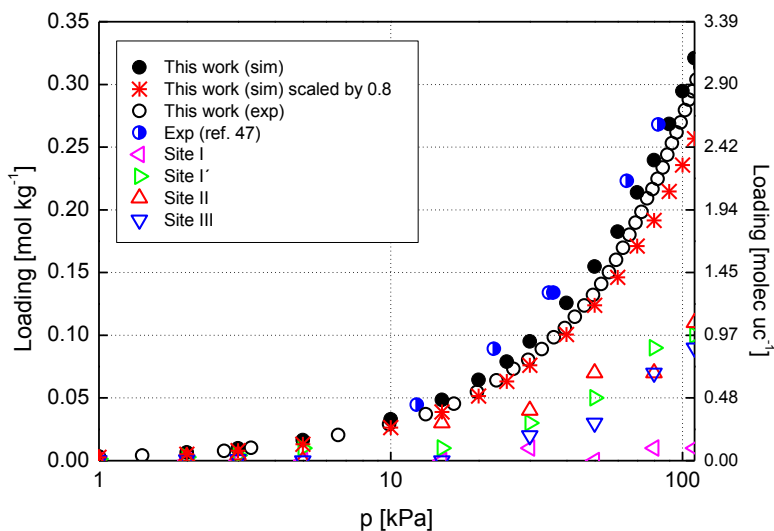


Figure 9.4 Comparison of simulated and experimental N_2 adsorption isotherms in Cu-BTC at 295 K. Our experimental and simulation results are represented by open and filled circles, respectively. Computed adsorption for the different sites is represented by left triangles (Site I), right triangles (Site I'), up triangles (Site II), and down triangles (Site III). Scaled simulation data are represented by stars and previous experimental data[49] (half-filled circles) are included for comparison.

The adsorption of O_2 and methane in Cu-BTC follows a similar behavior as N_2 as shown in Figures 9.5 (O_2) and 9.6 (methane) for our experimental and computed adsorption isotherms at 295 K. Available experimental[49] and simulation data[20,50] are included for comparison. The difference in the uptake measured in this work and that measured by Wang et al.[49] can be related to the different techniques and procedures used to obtain the isotherms; different synthesis procedures were employed, the MOFs were pelletized under pressure and crushed and sieved to particles of 1.4 mm[49]. In this case, adsorption in the macropores can play a role at high pressures. The experimental isotherms reported in this work were determined for the pure crystalline material, without further postprocessing.

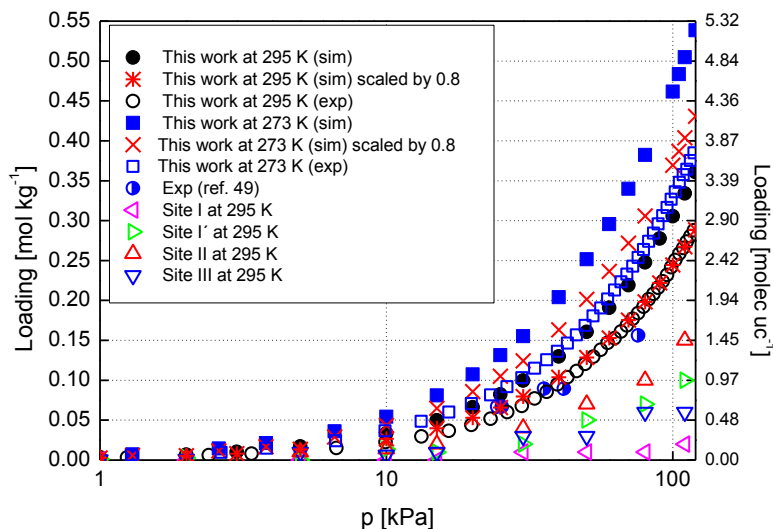


Figure 9.5 Comparison of simulated and experimental O_2 adsorption isotherms in Cu-BTC at 295 K (circles) and 273 K (squares). Our experimental and simulation results are represented by open and filled symbols, respectively. Computed adsorption for the different sites at 295 K is represented by left triangles (Site I), right triangles (Site I'), up triangles (Site II), and down triangles (Site III). Scaled simulation data are represented by stars and crosses and previous experimental data[49] at 295 K (half-filled circles) are included for comparison.

The contributions of the individual adsorption sites for O_2 and methane at 295 K are included in Figures 9.5 and 9.6, respectively. As observed before for N_2 , the positions close to the copper are not filled, and the octahedral cages (center and windows) as well as site I' are again the preferred locations for adsorption. The molecular sitting observed for O_2 , N_2 , and methane shows small differences that could be attributed to the quadrupole moment of the molecules. Hence, site II is filled predominantly for methane (the nonpolar molecule), whereas for N_2 the occupation of II and I' is almost equivalent. The quadrupolar moment of an O_2 molecule is approximately $4 \times$ smaller than that of a N_2 molecule, and consequently, the molecular sitting shows a behavior intermediate between that observed for methane and for N_2 .

The obtained adsorption isotherms for ethane at 295 K are shown in Figure 9.7. The adsorption mechanism for ethane in Cu-BTC is similar as for methane. It initiates at site II and at a loading of 0.8 mol kg^{-1} (corresponding to 8 molecules per unit cell) this site

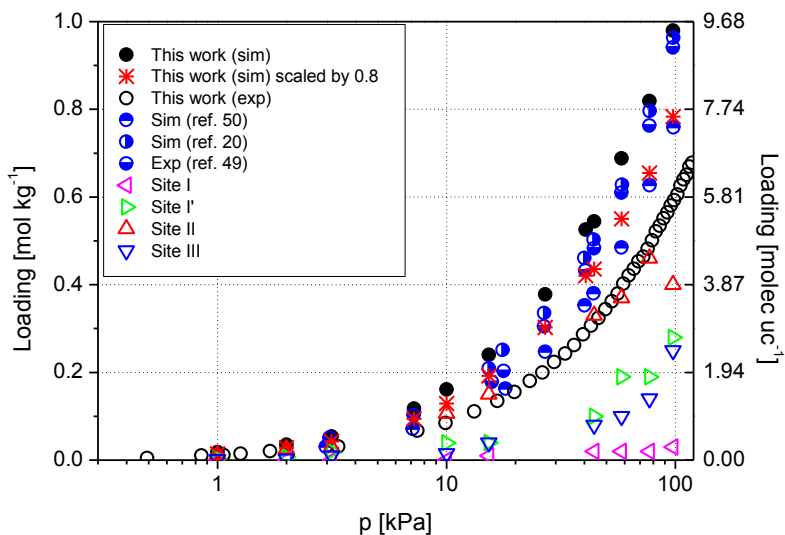


Figure 9.6 Comparison of simulated and experimental methane adsorption isotherms in Cu-BTC at 295 K. Our experimental and simulation results are represented by open and filled circles, respectively. Computed adsorption for the different sites is represented by left triangles (Site I), right triangles (Site I'), up triangles (Site II) and down triangles (Site III). Scaled simulation data are represented by stars and previous experimental[49] and simulation data[20] (half-filled circles) are included for comparison.

becomes saturated. The adsorption continues with occupation of sites I' and III, and as before site I remains empty. The computed Henry coefficients, energies, enthalpies, and entropies of adsorption at zero coverage and 295 K corroborate that II is the preferential adsorption site at low loading for all the molecules considered in this study. The obtained values are listed in Table 9.2. The adsorption isotherms for propane were computed and measured experimentally at 283, 318, 353, and 383 K. The agreement between our measured and calculated isotherms is good at the lower temperature (Figure 9.8) but surprisingly poor at the higher temperatures (Figure 9.9), where simulations provide much higher loadings than those obtained experimentally, not only by our group but also by other authors[51]. Volume changes like reported for other metal organic frameworks[52] could account for this phenomenon. Indeed, a reduction of the cell volume, caused by the shrinking of the $[\text{Cu}_2\text{C}_4\text{O}_8]$ cage, is observed after dehydration[3]. If the MOF structure contracts with temperature, then the available space in site I' may be smaller or site III may even become inaccessible. Both phenomena yield lower loadings.

To check if changes in the MOF structure happen due to temperature effects, temperature programmed XRD (XRTP) under N_2 atmosphere was performed. Figure 9.10 shows the XRD pattern of a hydrated sample (as synthesized) compared with the pattern for this material reported in the literature together with the comparison between hydrated and dehydrated samples measured at different temperatures. When two patterns are subtracted and only positive or negative peaks are observed this is due to a change in reflection intensity. If peak shifts occur, then pattern subtraction yields pairs of positive and negative peaks. As reported in literature, comparison between XRD at room temperature before and after dehydration reveals changes in the relative intensity of several reflections[3] and the disappearance of the peak at $2\theta = 5.9$ [9], related with a shrinking of the $[Cu_2C_4O_8]$ cage[3].

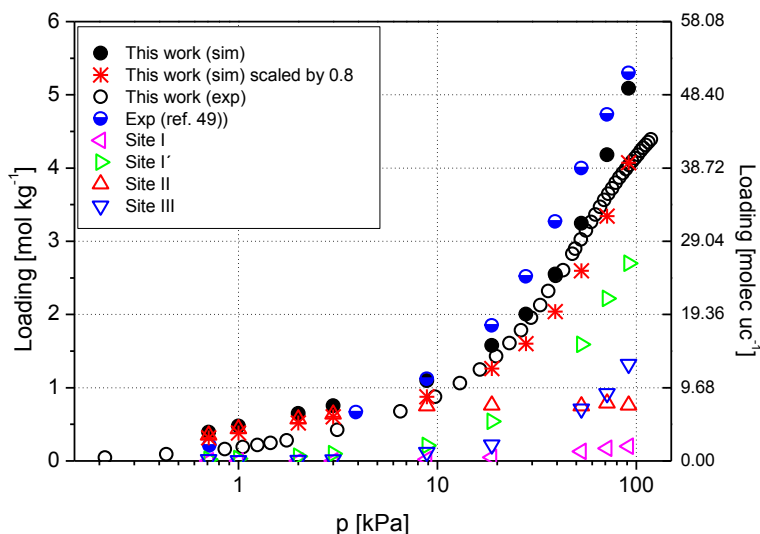


Figure 9.7 Comparison of simulated and experimental ethane adsorption isotherms in Cu-BTC at 295 K. Our experimental and simulation results are represented by open and filled circles, respectively. Computed adsorption for the different sites is represented by left triangles (Site I), right triangles (Site I'), up triangles (Site II), and down triangles (Site III). Scaled simulation data are represented by stars and previous experimental data[49] (half-filled circles) are included for comparison.

Even more interesting is the comparison between the XRD patterns of the dehydrated sample at different temperatures, the main reflections shift to larger 2θ values. By applying Bragg's law to the main reflections (plans 110, 220, 222, 400, 311, 330, and 440) a decrease of ~ 0.5 % in the lattice spacing could be calculated between the dehydrated sample at room temperature and the same sample at 373 K. A further decrease by 0.4 % occurred when increasing the temperature further to 473 K. Clearly, a reversible

change occurs in the crystalline lattice of Cu-BTC when changing the temperature, which may affect the adsorptive properties of the material in terms of packing density or accessibility. Our data show two effects separately: the structure shrinks (a) when water is

Table 9.2 Henry coefficients, energies, enthalpies, and entropies of adsorption computed at zero coverage for the different sites at 295 K^a.

site	K_H [molkg ⁻¹ Pa ⁻¹]	-dU [kJmol ⁻¹]	-dH [kJmol ⁻¹]	-dA [kJmol ⁻¹]	-dG [kJmol ⁻¹]	-dS [JK ⁻¹ mol ⁻¹]
methane						
I	3.31×10^{-6} (3)	9.07 (3)	11.52 (3)	4.82 (3)	7.27 (3)	14.4 (2)
I'	3.88×10^{-6} (4)	9.25 (2)	11.71 (2)	5.21 (2)	7.66 (2)	13.7 (1)
III	5.08×10^{-6} (3)	11.65 (5)	14.11 (5)	5.87 (1)	8.32 (1)	19.6 (2)
II + III	1.78×10^{-5} (1)	18.55 (3)	21.00 (3)	8.95 (2)	11.40 (2)	32.5 (1)
Cu-BTC	1.83×10^{-5} (2)	18.23 (4)	20.69 (4)	9.01 (3)	11.46 (3)	31.3 (2)
ethane						
I	2.44×10^{-5} (2)	15.62 (3)	18.08 (3)	9.72 (2)	12.18 (2)	20.0 (2)
I'	2.94×10^{-5} (3)	15.78 (4)	18.24 (4)	10.18 (2)	12.63 (2)	19.0 (2)
III	5.1×10^{-5} (2)	23.5 (4)	26.0 (4)	11.54 (8)	14.00 (8)	41 (1)
II + III	9.7×10^{-4} (2)	34.77 (7)	37.22 (8)	18.76 (6)	21.22 (6)	54.3 (5)
Cu-BTC	9.9×10^{-4} (3)	34.7 (1)	37.1 (1)	18.80 (7)	21.25 (7)	53.9 (6)
propane						
I	3.3×10^{-3} (9)	12.75 (2)	15.2 (2)	4.8 (6)	7.27 (6)	27 (2)
I'	4×10^{-3} (1)	12.94 (2)	15.39 (2)	5.2 (7)	7.66 (7)	26 (2)
III	1.82×10^{-3} (4)	44.0 (4)	46.5 (4)	20.30 (6)	22.75 (6)	80 (2)
II + III	1.6×10^{-2} (6)	46.9 (1)	49.4 (1)	25.5 (1)	28.0 (1)	72.2 (5)
Cu-BTC	1.56×10^{-2} (4)	46.86 (7)	49.31 (7)	25.56 (6)	28.01 (6)	49.67 (4)
nitrogen						
I	1.36×10^{-6} (5)	6.60 (1)	9.06 (1)	2.65 (1)	5.10 (1)	13.39 (7)
I'	1.54×10^{-6} (6)	6.72(1)	9.17 (1)	2.956 (9)	5.409 (9)	12.77 (8)
III	1.83×10^{-6} (1)	8.29 (2)	10.74 (3)	3.37 (1)	5.82 (1)	16.7 (1)
II + III	3.37×10^{-6} (3)	11.76 (2)	14.21 (2)	4.87 (2)	7.32 (2)	23.4 (1)
Cu-BTC	3.65×10^{-6} (3)	11.49 (4)	13.94 (4)	5.06 (2)	7.51 (2)	21.8 (2)
oxygen						
I	1.3×10^{-6} (8)	6.39 (1)	8.84 (1)	2.53 (1)	4.98 (1)	13.1 (1)
I'	1.47×10^{-6} (5)	6.551 (5)	9.003 (5)	2.841 (9)	5.294 (9)	12.57 (5)
III	1.98×10^{-6} (1)	8.85 (2)	11.30 (2)	3.56 (1)	6.01 (1)	17.9 (1)
II + III	3.50×10^{-6} (5)	11.72 (4)	14.18 (4)	4.96 (4)	7.41 (4)	22.9 (3)
Cu-BTC	3.76×10^{-6} (3)	11.42 (4)	13.88 (4)	5.13 (2)	7.60 (2)	21.3 (2)

^a The values for site II + III were computed for the sphere with radius 0.55 nm centered at the middle of the octahedral cage. Site III is defined as the spherical annulus between radii 0.2 nm (site II) and 0.55 nm. The obtained error bars are shown in brackets.

removed and (b) with increasing temperature (negative thermal expansion, NTE). We would like to highlight that for the first time NTE for Cu-BTC is reported. The NTE was previously observed only for isorecticular metal-organic frameworks by Dubbeldam et al.[34]

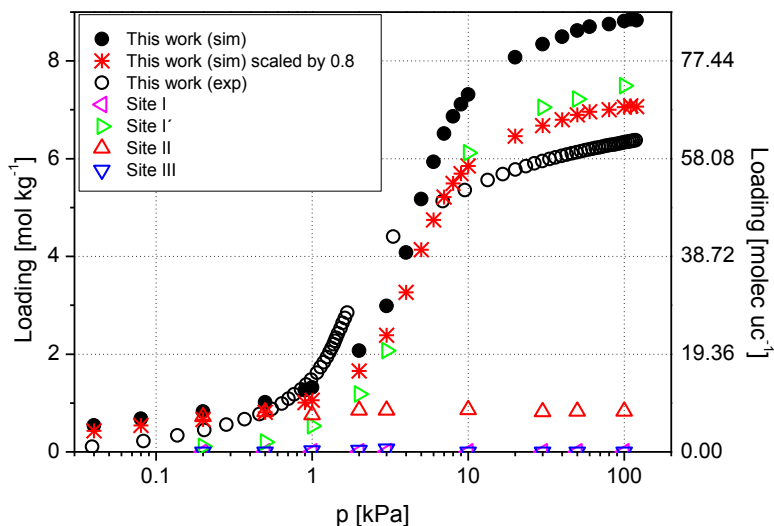


Figure 9.8 Comparison of simulated and experimental propane adsorption isotherms in Cu-BTC at 283 K. Our experimental and simulation results are represented by open and filled circles, respectively. Computed adsorption for the different sites is represented by left triangles (Site I), right triangles (Site I'), up triangles (Site II), and down triangles (Site III). Scaled simulation data are represented by stars.

The adsorption mechanism for propane is similar for the four temperatures studied in this work and only that at 283 K is plotted in Figure 9.8 for the sake of clarity. The occupation of the individual adsorption sites for propane at 283 K are also plotted in this figure. Again, site II is filled up before the other sites. The site becomes saturated with 8 molecules per unit cell and after that loading propane starts to fill site I', leaving both site I and III almost empty. The same pore filling behavior was found for higher temperatures (318, 353, and 383 K). Site I, related to the copper cations is inaccessible, due to the dehydration of the sample and the changed position of the copper. The molecular modeling has been performed with the structural parameters of the hydrated sample, the only information currently available, which does not account for these changed structural parameters. The low accessibility of site III is tentatively also attributed to these changed

lattice parameters due to dehydration. The accessibility of this window site in case of the larger propane molecule in this study may be very sensitive to small changes, also explaining the increased divergence between the modeling and experimental results with increasing temperature. A finetuning of the structural parameters for the dehydrated sample and its temperature dependency is required to establish a full match.

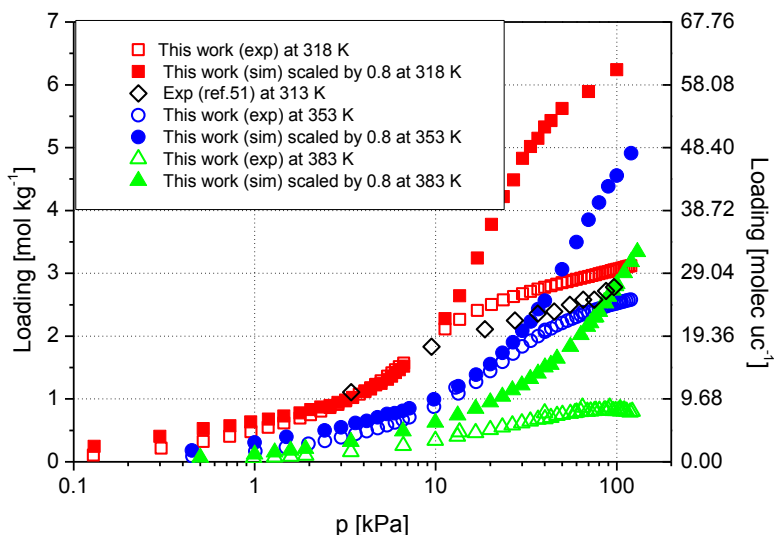


Figure 9.9 Comparison of rescaled simulation results and experimental propane adsorption isotherms in Cu-BTC at 318, 353, and 383 K. Our experimental and rescaled simulation results are represented by open and filled symbols, respectively. Previous experimental data[51] (at 313 K) (diamonds) are included for comparison.

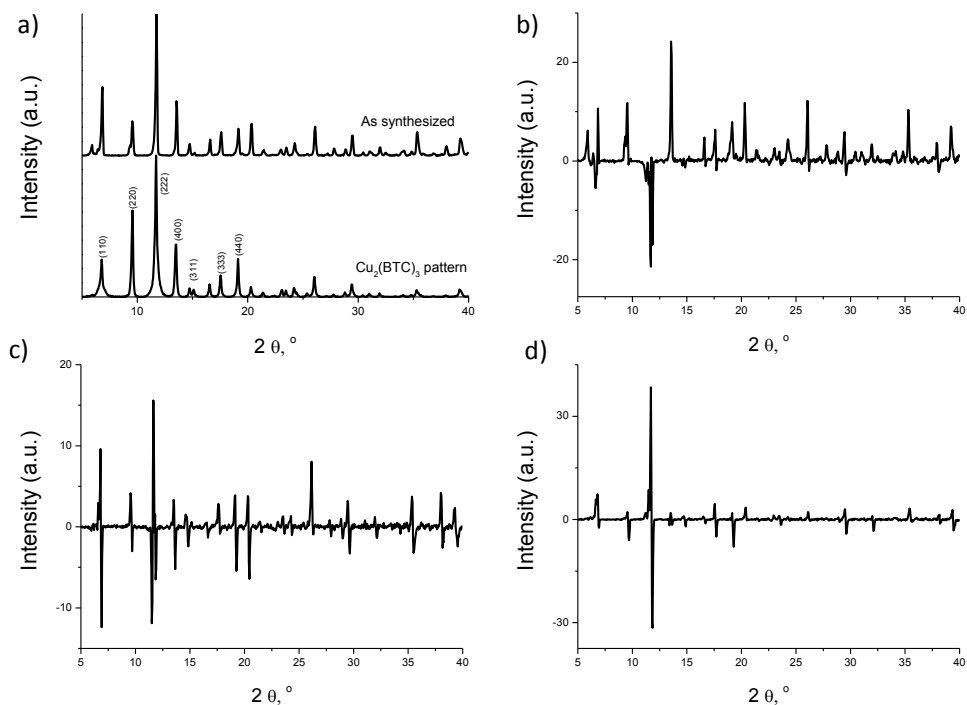


Figure 9.10 Temperature Programmed XRD results: (a) comparison between the as-synthesized material and the Cu-BTC pattern. (b) Difference of XRD patterns of the as synthesized sample (hydrated) and dehydrated sample at room temperature. (c) Difference pattern of dehydrated sample at room temperature and dehydrated sample at 373 K. (d) Difference pattern of dehydrated sample at 373 K and dehydrated sample at 473 K.

9.5 Conclusions

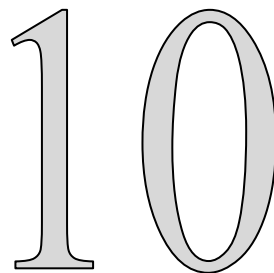
Cu-BTC is formed by two types of cages, one of them is commensurate with small molecules and the other one is capable of adsorbing larger molecules. This characteristic could induce strong selectivity for mixtures. Optimization of separation selectivity requires proper understanding of the adsorption behavior of Cu-BTC. With this work, we contributed to a better understanding of the interactions governing the Cu-BTC substrate, as well as the properties of the structure when water is removed. The observed negative thermal expansion for Cu-BTC has important implications for adsorption, because of the close match between small molecules and the small pockets. Future simulations should take this structural change into account to obtain a better match with experiments at higher temperatures.

Bibliography

- [1] Kitagawa, et al. *Angewandte Chemie-International Edition* **2004**, 43, 2334.
- [2] Mueller, et al. *Journal of Materials Chemistry* **2006**, 16, 626.
- [3] Prestipino, et al. *Chemistry of Materials* **2006**, 18, 1337.
- [4] Eddaoudi, et al. *Science* **2002**, 295, 469.
- [5] Yaghi, et al. *Nature* **2003**, 423, 705.
- [6] Chui, et al. *Science* **1999**, 283, 1148.
- [7] Lee, et al. *Advanced Functional Materials* **2007**, 17, 1255.
- [8] Wang and Ronnebro. *Trends in Materials and Manufacturing Technologies for Transportation Industries and Powder Metallurgy Research and Development in the Transportation Industry* **2005**, 21.
- [9] Schlichte, et al. *Microporous and Mesoporous Materials* **2004**, 73, 81.
- [10] Alaerts, et al. *Chemistry-a European Journal* **2006**, 12, 7353.
- [11] Ramsahye, et al. *Physical Chemistry Chemical Physics* **2007**, 9, 1059.
- [12] Walton, et al. *Journal of the American Chemical Society* **2008**, 130, 406.
- [13] Wang. *Energy & Fuels* **2007**, 21, 953.
- [14] Yang, et al. *Aiche Journal* **2007**, 53, 2832.
- [15] Yang and Zhong. *Journal of Physical Chemistry B* **2005**, 109, 11862.
- [16] Krungleviciute, et al. *Langmuir* **2007**, 23, 3106.
- [17] Krungleviciute, et al. *Aiche Journal* **2008**, 54, 918.
- [18] Vishnyakov, et al. *Nano Letters* **2003**, 3, 713.
- [19] Skoulidas and Sholl. *Journal of Physical Chemistry B* **2005**, 109, 15760.
- [20] Yang and Zhong. *Chemphyschem* **2006**, 7, 1417.
- [21] Yang and Zhong. *Journal of Physical Chemistry B* **2006**, 110, 655.
- [22] Yang and Zhong. *Journal of Physical Chemistry B* **2006**, 110, 17776.
- [23] Liu, et al. *Journal of Physical Chemistry C* **2007**, 111, 9305.
- [24] Wang, et al. *Separation and Purification Technology* **2008**, 60, 30.
- [25] Millward and Yaghi. *Journal of the American Chemical Society* **2005**, 127, 17998.
- [26] Dubbeldam, et al. *Physical Review Letters* **2004**, 93.
- [27] Krishna, et al. *Chemical Physics Letters* **2006**, 429, 219.
- [28] Garcia-Perez, et al. *Adsorption-Journal of the International Adsorption Society* **2007**, 13, 469.
- [29] Liu, et al. *Journal of Alloys and Compounds* **2007**, 446, 385.
- [30] Beerdsen, et al. *J. Phys. Chem. B* **2002**, 106, 10659.
- [31] Vlugt, et al. *Journal of Chemical Theory and Computation* **2008**, 4, 1107.

- [32] Vlucht and Schenk. *J. Phys. Chem. B* **2002**, 106, 12757.
- [33] Dubbeldam, et al. *Fluid Phase Equilibria* **2007**, 261, 152.
- [34] Dubbeldam, et al. *Angewandte Chemie-International Edition* **2007**, 46, 4496.
- [35] Mayo, et al. *Journal of Physical Chemistry* **1990**, 94, 8897.
- [36] Rappe, et al. *Journal of the American Chemical Society* **1992**, 114, 10024.
- [37] Frost and Snurr. **private communication**.
- [38] Martin and Siepmann. *J. Phys. Chem. B* **1998**, 102, 2569.
- [39] Murthy, et al. *Molecular Physics* **1980**, 41, 1387.
- [40] Mellot and Lignieres. *Molecular Simulation* **1996**, 18, 349.
- [41] Garcia-Perez, et al. *Applied Surface Science* **2005**, 252, 716.
- [42] Dubbeldam, et al. *Journal of Physical Chemistry B* **2004**, 108, 12301.
- [43] Duren and Snurr. *Journal of Physical Chemistry B* **2004**, 108, 15703.
- [44] Duren, et al. *Langmuir* **2004**, 20, 2683.
- [45] Calero, et al. *Journal of the American Chemical Society* **2004**, 126, 11377.
- [46] Calero, et al. *Journal of Physical Chemistry B* **2006**, 110, 5838.
- [47] Peterson, et al. *Journal of the American Chemical Society* **2006**, 128, 15578.
- [48] Surble, et al. *Journal of the American Chemical Society* **2006**, 128, 14889.
- [49] Wang, et al. *Microporous and Mesoporous Materials* **2002**, 55, 217.
- [50] Garberoglio, et al. *Journal of Physical Chemistry B* **2005**, 109, 13094.
- [51] Wagener, et al. *Chemie Ingenieur Technik* **2007**, 79, 851.
- [52] Ramsahye, et al. *Journal of Physical Chemistry C* **2008**, 112, 514.

The understanding of adsorption isotherms is important for the solution of a large class of industrial problems, many of which are of current research interest. The existence of stepped adsorption isotherms is often observed in some particular adsorption processes, being a distinction of mesoporous materials reflecting capillary condensation effects. However, such singularity is less observed at very low relative pressures. For instance, the presence of a substep on the argon adsorption isotherm of MFI at cryogenic temperature has been corroborated with a variety of experimental studies, but its origin is still unclear, and the interpretations are even contradictory. In this work, a new insight into this process is proposed by a combined approach using both experiments and molecular simulations.



E. García-Pérez, J.B. Parra, C.O. Ania, D. Dubbeldam, T.J.H. Vlugt, J.M. Castillo, P.J. Merkling, and S. Calero

Unraveling the Argon Adsorption Processes in MFI-Type Zeolite

Attempts to understand physisorption phenomena of argon in MFI-type zeolite motivate a great deal of theoretical and experimental research[1-8]. MFI-type zeolite is of scientific and technological interest in heterogeneous catalysis, separation, purification, and lately in environmental applications[9-11]. This structure is characterized by two sets of interconnecting channels defined by 10-membered rings, with straight channels extending in the $\langle 010 \rangle$ direction and sinusoidal channels in the $\langle 100 \rangle$ direction. It is well established by X-ray diffraction and NMR measurements that high-silica MFI undergoes a reversible phase transition at around 340 K, from a monoclinic to an orthorhombic structure[12]. The change in symmetry results only in minor changes of the framework positions and the unit cell vectors. Similar phase transitions from monoclinic to orthorhombic symmetry can also be reversibly induced by loading the zeolite with ammonia or with organic molecules[13-15].

Argon adsorption isotherms at 77 K measured by several groups[16-20] all show a kink/step at around 23 argon atoms per unit cell. The origin of this substep remains a subject of debate. It has been considered as an argon transition from the fluid phase to a more crystalline commensurate phase[19], as an intracrystalline process rather than a solidification occurring at the pore[21], to adsorbent deformations[22], and as a

framework phase transition from the monoclinic to the orthorhombic symmetry[6]. We have combined experimental measurements with molecular simulations to provide new insights into the adsorption processes of argon in MFI at 77 K. Our goal was to establish the effect of the adsorbate and the adsorbent on the nature and shape of the argon isotherm.

Adsorption studies were performed experimentally and using Monte Carlo (MC) simulations in the grand-canonical ensemble, and self-diffusion coefficients were obtained from the meansquare displacement using Molecular Dynamics (MD) simulations in the NVT ensemble and the velocity Verlet integration scheme with a time step of 0.5 fs. Simulations were performed for rigid (monoclinic[23], $P2_1/n$ space group, and orthorhombic[24], $Pnma$ space group), structures of MFI and flexible frameworks. For the flexible zeolite, we used a model that includes bond stretching, bond bending, bond angle coupling, a dihedral potential, Lennard-Jones interactions, and electrostatic interactions[25]. The Ewald summation was used to handle electrostatic interactions. To validate this force field, we have computed the infrared spectra of the zeolite at 77 and 298 K, as well as the adsorption isotherm at 300 K, and compared the results with experiments.

Infrared spectra were obtained as the Fourier transform of the charge-weighted velocity autocorrelation function of the whole system[26]. The charges used are 1.1 |e| for Si and -0.55 |e| for O as provided by the |e| model[25]. A step size of 1 cm^{-1} was chosen. Table 10.1 compares the peaks of the experimental spectra[27] with those obtained from molecular simulations at 77 and at 298 K. The agreement between the simulations and the experimental modes is excellent, thus validating the set of parameters used in this work for flexible structures. The modes between 1250 and 950 cm^{-1} correspond to strong bands attributed to the asymmetric Si–O stretching modes. The weak deformation modes between 820 and 650 cm^{-1} are assigned to a symmetrical Si–O stretching model, and those in the lowfrequency region (650–400 cm^{-1}) are associated with Si–O–Si bending modes. Whereas the experimental spectrum exhibits broad but well-separated peaks at 444 and 552 cm^{-1} , computed MFI structures both at 77 and at 298 K exhibit an absorption range from approximately 380 to 560 cm^{-1} with many maxima. Only the most intense have been selected.

Figure 10.1 shows the computed adsorption isotherms of argon in orthorhombic MFI at 300 K and using a rigid and a flexible framework. The isotherms for a rigid and flexible framework are almost identical and in excellent agreement with available data[28-30]. The interactions of the adsorbed molecules with the zeolite are dominated by the dispersive forces between the guest atoms and the oxygen atoms of the zeolite[31,32],

meaning that the silicon van der Waals interactions are taken into account through an effective potential with only the oxygen atoms. Argon–argon Lennard-Jones interaction parameters were obtained by fitting the force field to the experimental vapor–liquid equilibrium curve using a truncated and shifted potential.

Table 10.1 Infrared spectra peaks (cm^{-1}) obtained from molecular simulations at 77 and 298 K and compared with experimental spectra[27]^a.

experimental	MFI 298 K	MFI 77 K
444 (s)	464, 487 (w)	445, 480 (w)
552 (m)	562 (w)	560 (w)
804 (w)	770 (w)	776 (w)
1096 (s)	1102 (s)	1103 (s)

^a The error bars in the computed frequencies are on the order of 10 cm^{-1} [(w) weak peak, (s) strong peak, (m) medium peak]

Argon–oxygen Lennard-Jones parameters were obtained by calibrating the force field through explicitly fitting three points of the experimental isotherm shown in Figure 10.2. Simulations were performed at 2.0×10^{-3} , 9.0×10^{-2} , and 9.0×10^{-1} kPa using the rigid, monoclinic structure at 77 K. Detailed information about the force fields and simulation parameters can be found in the Supporting Information.

Low-temperature (77.3 K) and low-pressure experimental argon isotherms were measured in a Micromeritics ASAP 2010 M gas adsorption analyzer in the pressure range from 10^{-4} to 26 kPa. The instrument was equipped with a molecular drag vacuum pump and three different pressure transducers (0.133 kPa, uncertainty within 0.12 % of reading; 1.33 and 133 kPa, uncertainty within 0.15 % of reading) to enhance the sensitivity in the low-pressure range, which is especially useful in adsorption studies on highly microporous materials. Prior to the adsorption measurements, the sample was outgassed in situ under vacuum at 673 K overnight to remove any adsorbed impurities. The elapsed time for the measurement of the argon isotherm on silicate was 52 h, with over 100 equilibrium points. The argon saturation pressure was measured throughout the entire analysis by means of a pressure transducer; the nonideality factor was 5×10^{-5} . Argon was supplied by Air Products with an ultrahigh purity (i.e., 99.9992 %).

Figure 10.2 shows the experimental and computed adsorption isotherms of argon in MFI at 77 K. Simulations were performed for (a) the crystallographic monoclinic and orthorhombic structure, keeping the framework rigid during the simulation and (b) a flexible framework starting from the monoclinic structure. The experimental adsorption isotherm obtained for argon is of type-I character, although it exhibits a substep at 5×10^{-3} Pa, in agreement with those found previously in the literature[16-20]. Our simulation results using rigid frameworks correctly reproduce the saturation loading (simulations always provide slightly higher saturation loadings than experiments since the simulated frameworks are defect free), but they underestimate adsorption in the monoclinic structure and overestimate adsorption in the orthorhombic structure, in the vicinity of the substep region. Furthermore, both overestimate the adsorption in the low-pressure regime. On the other hand, the simulation data using the flexible framework show good agreement with the experimental isotherm in the whole range of pressures, matching closely with those obtained for the rigid monoclinic framework at low pressures and with those obtained for the rigid orthorhombic framework at high pressures.

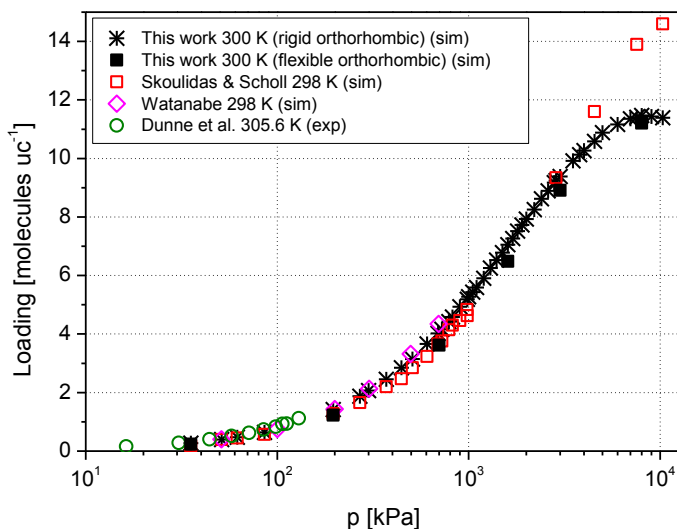


Figure 10.1 Computed adsorption isotherms of argon in orthorhombic MFI at 300 K using a rigid and a flexible framework, compared with available previous data[25-27].

Additional Molecular Dynamics simulations have been performed to compute self-diffusion coefficients for 7, 14, 23, and 31 molecules of argon per unit cell at 77 K in rigid and flexible frameworks. The obtained results are listed in Table 10.2. Diffusion decreases with argon loading and shows lower values for the orthorhombic structure than those for the monoclinic structure. Simulations using a flexible framework show

intermediate self-diffusion coefficients for 7, 14, and 23 molecules of argon per unit cell and an increased diffusivity at the saturation loading. The fact that simulations using flexible frameworks provide adsorption and diffusion values between those obtained for the rigid structures suggests a monoclinic to orthorhombic transition and not a phase transition of argon due to the confinement as the most probable reason for the adsorption substep; that would provide much lower diffusion coefficients in the substep than the ones obtained from our calculations. In general, an increase in adsorption in the zeolitic pore provokes a decrease in the molecular diffusion. The experimentally pronounced kink implies a fast adsorption in a very narrow pressure range and therefore a decrease in the diffusion coefficient. If this “fast” adsorption was also affected by a phase transition of the argon, the molecular order would be higher, leading to an even lower molecular diffusion.

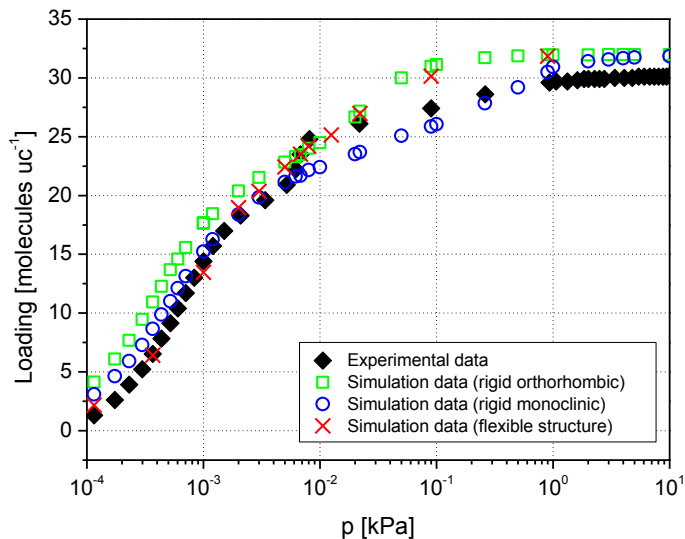


Figure 10.2 Experimental and computed adsorption isotherms of argon in MFI at 77 K.

Table 10.2 Computed self-diffusion coefficients in MFI-type zeolite as a function of argon loading at 77 K.

molecules of argon per unit cell	$D \cdot 10^{-11} \text{ [m}^2 \text{ s}^{-1}\text{]}$ monoclinic rigid structure	$D \cdot 10^{-11} \text{ [m}^2 \text{ s}^{-1}\text{]}$ orthorhombic rigid structure	$D \cdot 10^{-11} \text{ [m}^2 \text{ s}^{-1}\text{]}$ flexible structure
7	34 ± 2	30 ± 3	32 ± 5
14	29.1 ± 1.5	22.5 ± 0.5	26.2 ± 1.0
23	8.1 ± 1.5	7.8 ± 1.1	8.0 ± 1.6
31	0.39 ± 0.12	0.7 ± 0.3	0.7 ± 0.4

Molecular simulations starting from the monoclinic framework but allowing framework flexibility provide indirect evidence of the framework change upon argon adsorption with (1) values for the self-diffusion coefficients completely comparable with those obtained from the rigid structures, (2) good agreement with the experimental adsorption isotherm at 77 K in the whole range of pressures, as shown in Figure 2, and (3) strongly increasing framework–framework interactions when the loading of argon is increased, indicating deformations of the framework (Figure 10.3-left). Argon–argon and argon–framework energies obtained at several pressures and at the substep show no evidence of a phase transition of argon following a quasilinear behavior of the energy with argon loading (Figure 10.3-right).

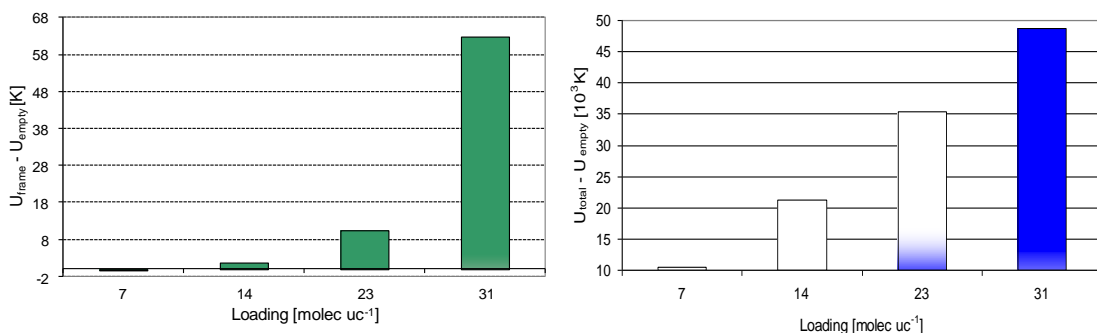


Figure 10.3 Computed interactions as a function of argon loading at 77 K normalized versus the energy of the empty framework (U_{empty}); (left) framework–framework interactions (U_{frame}) and (right) framework–framework, framework–argon, and argon–argon interactions (U_{total}). The energy for the empty framework U_{empty} is 1.04276610×10^8 K.

According to our simulations results, the favorable adsorption sites for argon are the straight channels at very low loadings (less than 2 molecules per unit cell), but the molecules are pulled off of those sites toward the zigzag channels at medium coverage (16 molecules per unit cell). Argon molecules completely fill the pore intersections at

saturation once the zigzag and the straight channels are full. Our findings are in agreement with those proposed in 1994 by Pellenq and Nicholson[33]. They provided a similar mechanism for the filling of the MFI pores and suggested a change in the framework as the most plausible explanation for the experimental substep at 23 molecules per unit cell at 77 K, but none of their models were able to reproduce it. We have presented a combination of high-quality experiments and molecular simulations that provide additional support that a subtle interplay between the guest molecules and the flexible host structure could be responsible for kinks/steps in the isotherms.

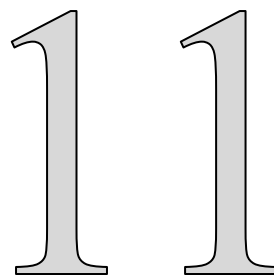
Bibliography

- [1] Coulomb, et al. Crystalline-Structure Analysis by Neutron-Diffraction of Argon Sorbed Phases Observed in the High Loading Regime of Silicalite-I and Zsm-5 (Si/Al=23) Zeolites. In *Characterization of Porous Solids Iii*, 1994; Vol. 87; pp 535.
- [2] Douguet, et al. *Molecular Simulation* **1996**, 17, 255.
- [3] Llewellyn, et al. *Journal of Thermal Analysis* **1992**, 38, 683.
- [4] Nakai, et al. *Adsorption-Journal of the International Adsorption Society* **2007**, 13, 351.
- [5] Nicholson and Pellenq. *Advances in Colloid and Interface Science* **1998**, 77, 179.
- [6] Pellenq and Nicholson. *Langmuir* **1995**, 11, 1626.
- [7] Pellenq, et al. *Journal of Physical Chemistry* **1995**, 99, 10175.
- [8] Tao, et al. *Advanced Materials* **2005**, 17, 2789.
- [9] Schenk, et al. *Journal of Catalysis* **2003**, 214, 88.
- [10] Krishna, et al. *Chemical Society Reviews* **2002**, 31, 185.
- [11] Guisnet and Gilson *Zeolites for cleaner technologies*; Imperial College Press: London, 2002; Vol. 3.
- [12] Hay and Jaeger. *Journal of the Chemical Society-Chemical Communications* **1984**, 1433.
- [13] Fyfe, et al. *Journal of the American Chemical Society* **1988**, 110, 3373.
- [14] Wu, et al. *Journal of Physical Chemistry* **1979**, 83, 2777.
- [15] Snurr, et al. *Journal of Physical Chemistry* **1993**, 97, 13742.
- [16] Hammond, et al. *Langmuir* **2007**, 23, 8371.
- [17] Muller, et al. *Fresenius Zeitschrift Fur Analytische Chemie* **1989**, 333, 433.
- [18] Saito and Foley. *Microporous Materials* **1995**, 3, 543.
- [19] Llewellyn, et al. *Langmuir* **1993**, 9, 1846.
- [20] Borghard, et al. *Journal of Catalysis* **1993**, 139, 19.

- [21] Maglara, et al. *Langmuir* **1994**, *10*, 4167.
- [22] Tvardovski, et al. *Journal of Colloid and Interface Science* **1997**, *191*, 117.
- [23] Vankoningsveld, et al. *Zeolites* **1990**, *10*, 235.
- [24] Baerlocher *Atlas of Zeolite Structure Types*, 5th ed.; Elsevier: London, 2001.
- [25] Nicholas, et al. *J. Am. Chem. Soc.* **1991**, *113*, 4792.
- [26] Bornhauser and Bougeard. *J. Phys. Chem. B* **2001**, *105*, 36.
- [27] Serrano, et al. *Journal of the Chemical Society-Chemical Communications* **1992**, 745.
- [28] Skoulidas and Sholl. *Journal of Physical Chemistry B* **2002**, *106*, 5058.
- [29] Watanabe, et al. *Molecular Simulation* **1995**, *15*, 197.
- [30] Dunne, et al. *Langmuir* **1996**, *12*, 5888.
- [31] Kiselev, et al. *Zeolites* **1985**, *5*, 261.
- [32] Bezus, et al. *Journal of the Chemical Society-Faraday Transactions II* **1978**, *74*, 367.
- [33] Pellenq and Nicholson. Rare-Gas Probes for Energetic Heterogeneity in Zeolite Pores - Theory and Simulation. In *Characterization of Porous Solids Iii*, 1994; Vol. 87; pp 21.

Conclusions

Molecular simulations provide an important tool to understand the relation between microscopic and macroscopic properties of many molecules in several structures. The field of molecular simulation is quickly growing and means a great complement for the experimental techniques. Following the scheme presented in the section 1.5, the main conclusions of this work are summarized below:



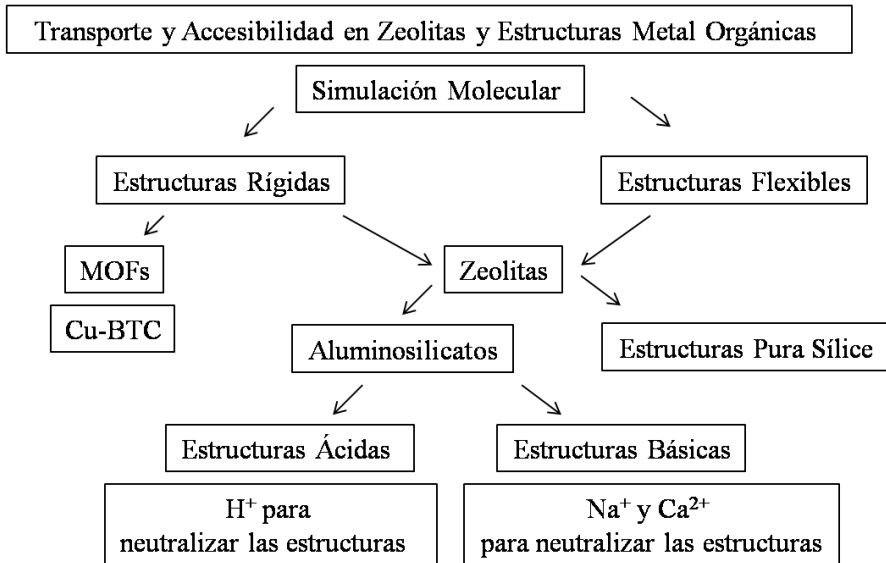
- A realistic model of host structures, guest molecules, as well as a proper definition of the interactions between them is needed to get into high-quality results.
- We can predict the adsorption behavior of single components as well as multicomponent mixtures in many structures (pure silica, basic, and acidic zeolites, as well as MOFs). The adsorption selectivity for binary and ternary mixtures is always in favor of the molecule which has the highest polarity, but depends on the type of the framework and on the mixture bulk composition.
- With regard to diffusion, the obtained results show that the transport of molecules is strongly dependent on the loading, the molecular length, and the choice of the structure. At saturation loading diffusion coefficients of any species reduce to zero.
- From simulation data of adsorption of *n*-alkanes at low coverage regime in sodium-exchanged MFI-, FAU-, and MOR- type zeolites, it is possible to provide simple empirical expressions that adequately describe the Henry coefficients and heats of adsorption of these molecules as a function of the cation density, temperature, and pressures. We can also provide an expression for saturation capacities of linear alkanes at high coverage regime in sodium MFI-type zeolites. These empirical expressions are an adequate substitute for complex Configurational-bias Monte Carlo simulations which mean an expensive computational cost.
- It is also possible to predict the preferential sites of adsorption of the studied molecules at specific conditions of temperature, pressure, and bulk chemical composition. This provides useful information about the interactions of guest molecules with the host framework.

- In this work we develop a new force field which accurately describes the adsorption properties of linear alkanes in Na/Ca zeolites. Our simulation results showed good agreement with previous available experimental and simulation data, so the reliability of our work is confirmed.
- We proposed a computational method to characterize framework aluminum in aluminosilicates and to identify the most likely positions of aluminum in several zeolites. The location of these atoms affects the position of the non-framework ions, and thus influences the adsorption and diffusion behavior of the guest molecules. The method can be so useful for designing more efficient industrial adsorbents.
- MOFs are a new family of metal-containing clusters. Due to their different pore dimensions, they have important applications in adsorption separation processes. Cu-BTC is formed by two types of cages and we showed that this structure induces strong selectivity for mixtures.
- Concerning the inclusion of framework flexibility, our results showed that exists a relationship between the adsorbed molecules and the flexible host structure. This could be the responsible of structural phase transitions among others phenomena.

I will finish this section by highlighting what in my opinion is the most important conclusion of this work. Molecular Modeling is nowadays an extremely powerful tool to predict molecular adsorption and diffusion in zeolites and MOFs, one must be careful on the choice of the different factors involved on the simulations: the definition of realistic host and guest models, the choice of accurate and transferable atomic and molecular force fields, fast and efficient simulation methods, a good knowledge of the crystallographic positions for the non-framework cations to be used as starting point in the simulations, non-accessible pockets blockage, the use of excess adsorption when direct comparison with experiment is required, an adequate choice of the equation of state to properly obtain the fugacity coefficients, or the use of flexible frameworks when these are really needed. In this thesis we provided some hints about how to address all these different factors to be able not only to reproduce previous available experimental and simulation data but also to apply the obtained knowledge to the development and design of new materials.

Resumen y conclusiones (Summary and conclusions in Spanish)

Esta tesis está estructurada en base al siguiente esquema:



Esquema de trabajo seguido en esta tesis.

Primero hemos llevado a cabo simulaciones moleculares en estructuras rígidas. Hemos estudiado dos tipos de materiales porosos: zeolitas y estructuras metal-orgánicas (MOFs). Las zeolitas estudiadas pueden estar compuestas por a) átomos de silicio y oxígeno (zeolitas pura sílice), b) átomos de silicio, aluminio y oxígeno con cationes sodio y calcio (zeolitas básicas) o c) átomos de silicio, aluminio y oxígeno con protones (zeolitas ácidas). En estas estructuras estudiamos procesos de adsorción y difusión de alcanos, CO₂ y N₂. En cuanto a los MOFs, se estudian las propiedades de adsorción de alcanos, N₂ y O₂ en Cu-BTC. También se realiza un análisis de los sitios preferentes de adsorción de estas moléculas adsorbidas en la estructura mencionada.

Para estudiar el efecto de la cantidad de moléculas adsorbidas sobre posibles cambios de fase usamos modelos flexibles.

Todo el trabajo realizado se ha llevado a cabo usando técnicas de simulación molecular descritas en el primer capítulo de la tesis.

Estudio de las propiedades de adsorción y difusión de moléculas polares y no polares en zeolitas pura sílice. (Capítulos 2 y 3)

En el capítulo 2 se estudian las propiedades de adsorción de CO_2 , N_2 y CH_4 en zeolitas pura sílice (MFI, MOR, ISV, ITE, CHA y DDR) usando técnicas de simulación molecular. Se obtienen isotermas de adsorción para un rango de presiones que van desde el régimen de Henry hasta la saturación. Las simulaciones se realizan a varias temperaturas tanto para componentes puros como en mezclas binarias y ternarias, variando la proporción de cada uno de los componentes. Nuestras simulaciones nos permiten conocer el comportamiento de adsorción de mezclas multicomponentes así como la localización de las moléculas a una presión, temperatura y composición química determinada.

En el capítulo 3 se realizan simulaciones de dinámica molecular para determinar los valores de auto-difusión del CH_4 y CO_2 como componentes puros y en mezclas equimolares. Este estudio se realiza en tres tipos de zeolitas: MFI, CHA y DDR. Los resultados obtenidos muestran que el comportamiento de difusión de las moléculas estudiadas depende de la cantidad de moléculas adsorbidas y de la estructura de la zeolita (canales que se cruzan o bien cajas separadas por ventanas estrechas).

Estudio de las propiedades de adsorción de alcanos lineales en aluminosilicatos y efecto de la posición del Al en la estructura. (Capítulos 4, 5, 6, 7 y 8)

En los capítulos 4 y 5 se calculan isotermas de adsorción, coeficientes de Henry y calores de adsorción de alcanos lineales en zeolitas tipo MFI, MOR y FAU con cationes sodio, usando simulaciones Configurational-bias Monte Carlo. En esta sección se desarrollan expresiones empíricas para describir las propiedades de adsorción de estas zeolitas a partir de los datos obtenidos por simulación. Se presentan expresiones que describen los coeficientes de Henry y calores de adsorción de n -alcanos en función de la densidad de cationes sodio y la temperatura. Nuestros resultados reproducen los valores obtenidos por técnicas experimentales.

En el capítulo 6 se desarrolla un nuevo campo de fuerza que incluye cationes calcio para describir las propiedades de adsorción de alcanos lineales en zeolitas LTA 5A. Estas zeolitas contienen cationes Na y Ca. Una vez validado el campo de fuerza usando resultados experimentales se estudian a) los calores de adsorción y coeficientes de Henry en función de la longitud de la cadena del hidrocarburo y b) el efecto de los cationes en zeolitas LTA 5A.

En los capítulos 7 y 8 se propone un método computacional para a) caracterizar las estructuras de diversos aluminosilicatos, b) identificar las posiciones más favorables de los átomos de aluminio en zeolitas tipo TON, FER y MOR y c) interpretar los mecanismos moleculares que rigen los procesos de adsorción en estas estructuras. Las simulaciones muestran que la localización del aluminio influye directamente en la posición de los iones y por tanto puede alterar la adsorción molecular.

Estudio de la adsorción de diferentes moléculas en Cu-BTC e identificación de los sitios de adsorción. (Capítulo 9)

En este capítulo se analiza la adsorción de distintas moléculas gaseosas polares (N_2 y O_2) y no polares (metano, etano y propano) en Cu-BTC mediante técnicas de simulación Monte Carlo. Además, se determinan los sitios preferentes de adsorción de los distintos adsorbatos en la estructura, en función de la presión y del número de moléculas.

Estudio de los procesos de adsorción de argón en la zeolita tipo MFI. (Capítulo 10)

En este capítulo se propone una nueva aproximación del proceso de adsorción de argón a 77 K combinando técnicas experimentales con simulación molecular. A 77 K se produce un bucle en la isoterma de argón que es corroborado por estudios experimentales previos pero su origen genera aún controversia. Los resultados obtenidos muestran que la interacción entre las moléculas adsorbidas y la estructura podría ser la responsable de este bucle de la isoterma.

Las simulaciones moleculares son una importante herramienta para entender la relación entre las propiedades microscópicas y macroscópicas de muchas moléculas en diferentes estructuras. Este campo de simulación molecular crece con rapidez y supone un complemento consistente para las técnicas experimentales.

Siguiendo el esquema presentado al comienzo de esta sección, las principales conclusiones de este trabajo se resumen a continuación.

- Para obtener buenos resultados es necesario el diseño de modelos realistas para adsorbentes y adsorbatos, así como una adecuada definición de las interacciones entre ellos.

- Podemos predecir cómo se transportan y adsorben diferentes moléculas y sus mezclas multicomponentes en una gran variedad de estructuras porosas (zeolitas pura sílice, básicas, ácidas, así como MOFs). La selectividad de adsorción de mezclas binarias y ternarias siempre está a favor de las moléculas con mayor polaridad, pero el grado de selectividad depende del tipo de estructura y de la composición de la mezcla.
- En cuanto a la difusión, los resultados obtenidos muestran que el transporte de las moléculas depende en gran medida de la cantidad de moléculas adsorbidas, del tamaño de las moléculas y del tipo de estructura. En condiciones de saturación los coeficientes de difusión tienden a cero.
- A partir de los datos de simulación obtenidos para la adsorción de alcanos lineales a bajas presiones en zeolitas con cationes tipo MFI, FAU y MOR, podemos proporcionar expresiones empíricas sencillas que describen con precisión los coeficientes de Henry y los calores de adsorción de estas moléculas en función de la densidad de cationes, la temperatura y la presión. Además, también se proporciona una expresión para la capacidad de adsorción de alcanos lineales a altas presiones en zeolitas tipo Na-MFI. Estas expresiones pueden sustituir a las simulaciones, lo que supone un alto ahorro computacional.
- A lo largo del trabajo se predicen sitios preferentes de adsorción en distintas estructuras en condiciones concretas de temperatura, presión y composición química. Esto nos proporciona información detallada sobre el modo en que interaccionan las moléculas con la estructura porosa.
- Se propone un método computacional para caracterizar las estructuras con aluminio e identificar las posiciones más favorables de éstos en las distintas zeolitas. La posición de los átomos de aluminio afecta a las posiciones de los iones que neutralizan la estructura, y esto influye en la adsorción y difusión de las moléculas estudiadas. Este estudio puede resultar muy útil para el diseño de materiales con aplicaciones industriales.
- Los MOFs son una nueva familia de nanomateriales que contienen iones metálicos en su estructura. Debido a que presentan poros de diferentes dimensiones pueden resultar muy útiles en procesos de separación. El Cu-BTC está formado por dos tipos de poros, lo que induce a una fuerte selectividad para las mezclas.

- En cuanto a la inclusión de modelos de estructuras flexibles, nuestros resultados muestran que existe una relación entre las moléculas adsorbidas y la estructura, que pueden ser la responsable de cambios estructurales en la zeolita.

Me gustaría finalizar esta sección resaltando la que, en mi opinión, es la conclusión más importante de este trabajo. Aunque la Simulación Molecular es hoy en día una herramienta extremadamente potente para predecir las propiedades de adsorción y difusión de moléculas en zeolitas y MOFs, debemos ser precavidos en la elección de los factores implicados en las simulaciones: la definición realista de los modelos de estructuras y moléculas, la elección de campos de fuerza atomísticos y moleculares precisos, métodos de simulación rápidos y eficientes, un buen conocimiento de las posiciones cristalográficas de los iones que neutralizan las estructuras como punto de partida en las simulaciones, el correcto bloqueo de sitios no accesibles experimentalmente, el uso de adsorciones de exceso cuando se compara directamente con datos experimentales, una buena elección de la ecuación de estado para obtener los coeficientes de fugacidad o el uso de modelos flexibles de estructuras cuando realmente se requiera. En esta tesis se proporciona nueva información relevante sobre cómo manejar los diferentes factores para ser capaces no sólo de reproducir los datos experimentales existentes, sino también para aplicar el conocimiento de las propiedades de adsorción y difusión al diseño y desarrollo de nuevos materiales.

List of publications

Chapter 2

E. García-Pérez, J.B. Parra, C.O. Ania, A. García-Sánchez, J.M. van Baten, R. Krishna, D. Dubbeldam, and S. Calero. “A computational study of CO₂, N₂, and CH₄ adsorption in zeolites”. *Adsorption*, 13, 469-476 (2007).

Chapter 3

R. Krishna, J.M. van Baten, E. García-Pérez, and S. Calero. “Diffusion of CH₄ and CO₂ in MFI, CHA, and DDR zeolites”. *Chemical Physics Letters*, 429, 219-224 (2006).

Chapter 4

E. García-Pérez, I.M. Torréns, S. Lago, R. Krishna, B. Smit, and S. Calero. “Molecular simulation of adsorption of n-alkanes in Na-MFI zeolites. Determination of empirical expressions”. *Studies in Surface Science and Catalysis*, 158, 1097-1104 (2005).

Chapter 5

E. García-Pérez, I.M. Torréns, S. Lago, D. Dubbeldam, T.J.H. Vlught, T.L.M. Maesen, B. Smit, R. Krishna, and S. Calero. “Elucidating alkane adsorption in sodium exchanged zeolites from molecular simulations to empirical equations”. *Applied Surface Science*, 252, 716-722 (2005).

Chapter 6

E. García-Pérez, D. Dubbeldam, T.L.M. Maesen, and S. Calero. “Influence of cation Na/Ca ratio on adsorption in LTA 5A: a systematic molecular simulation study of alkane chain length”. *Journal of Physical Chemistry B*, 110, 23968-23976 (2006).

Chapter 7

E. García-Pérez, D. Dubbeldam, B. Liu, B. Smit, and S. Calero. “A computational method to characterize framework aluminium in aluminosilicates”. *Angewandte Chemie International Edition*, 45, 276-278 (2007).

Chapter 8

B. Liu, E. García-Pérez, D. Dubbeldam, B. Smit, and S. Calero. “Understanding aluminum location and non-framework ions effects on alkane adsorption in aluminosilicates: a molecular simulation study”. *Journal of Physical Chemistry C*, 111, 10419-10426 (2007).

Chapter 9

E. García-Pérez, J. Gascón, V. Morales, J.M. Castillo, F. Kapteijn, and S. Calero. “Identification of adsorption sites in the Metal Organic Framework Cu-BTC using Molecular Simulations”. *Langmuir*. 25, 1725-1731 (2009).

Chapter 10

E. García-Pérez, J.B. Parra, C.O. Ania, D. Dubbeldam, T.J.H. Vlugt, J.M. Castillo, P. J. Merklings, and S. Calero. “Unraveling argon adsorption processes in MFI-type zeolite”. *Journal of Physical Chemistry C*, 112 (27), 9976–9979 (2008).

Not included in this thesis

E. García-Pérez, P.S. Barcia, J.A.C. Silva, A.E. Rodrigues, and S. Calero. “Influence of the sodium and calcium non-framework cations on the adsorption of hexane isomers in zeolite BEA”. *Theoretical Chemistry Accounts* (accepted).

V. Finsy, S. Calero, E. García-Pérez, P.J. Merklings, G. Vedts, D. De Vos, G.V. Baron, and J.F.M. Denayer. “Low coverage adsorption properties of the Metal-Organic Framework MIL-47 studied by pulse chromatography and Monte Carlo simulations”. *Physical Chemistry Chemical Physics*, 11, 3515–3521 (2009)

A. Martín-Calvo, E. García-Pérez, J.M. Castillo, and S. Calero. “Molecular simulations for adsorption and separation of natural gas in IRMOF-1 and Cu-BTC Metal-Organic Frameworks”. *Physical Chemistry Chemical Physics*, 10, 7085–7091 (2008)

T.J.H. Vlugt, E. García-Pérez, D. Dubbeldam, and S. Calero. “Computing the heat of adsorption using molecular simulations: The effect of strong coulombic interactions”. *Journal of Chemical Theory and Computation* 4 (7), 1107–1118 (2008)

A. García-Sánchez, E. García-Pérez, D. Dubbeldam, R. Krishna, and S. Calero. "A simulation study of alkanes in Linde Type A zeolites". *Adsorption Science and Technology*, 25, 417-429 (2007).

R. Krishna, J.M. van Baten, E. García-Pérez, and S. Calero. "Incorporating the loading dependence of the Maxwell-Stefan diffusivity in the modeling of CH₄ and CO₂ permeation across zeolite membranes". *Industrial Engineering Chemistry Research*, 46, 2974-2986 (2007).

S. Calero, M.D. Lobato, E. García-Pérez, J.A. Mejías, S. Lago, T.J.H. Vlugt, T.L.M. Maesen, B. Smit, and D. Dubbeldam. "A coarse-graining approach for the proton-complex in protonated aluminosilicalites". *Journal of Physical Chemistry, B*, 110, 5838-5841 (2006).

